

UNIVERSIDADE DE LISBOA
FACULDADE DE CIÊNCIAS
DEPARTAMENTO DE FÍSICA



**New numerical approaches to galaxy cluster simulations in
non-homogeneous LTB models**

Sara Nóbrega Fernandes de Nóbrega

Mestrado em Física
Especialização em Astrofísica e Cosmologia

Dissertação orientada por:
António da Silva
José P. Mimoso

Acknowledgments

I want to start by thanking my supervisors António da Silva e José Mimoso. They were always available to discuss the progress and details of this work. They constantly checked if everything was going smoothly and if I needed any help, in which case they would point me in the right direction. They were very dedicated and thoughtful and they are mentors whom anyone can easily look up to.

I want to thank my family for all the kindness and for all the annoying usual question "Haven't you finished your thesis yet?" alongside for their unconditional support and affection.

I am immensely grateful for having shared this MsC journey with wonderful friends and colleagues. Their names are too important not to be mentioned: Thank you to Bea, André, Ana, Cláudia, Alicja, Isabel, Rita, and Tiago. Your support and fellowship means everything to me.

Abstract

The cosmological principle, which states that the Universe is homogeneous and isotropic, is the basis of modern cosmology. The upcoming ESA/Euclid satellite mission will test this paradigm over a wide range of scales allowing us to assess whether the non-homogeneous Lemaitre-Tolman-Bondi (LTB) models should be considered to accurately describe observations locally and at intermediate cosmological scales. The Euclid survey is expected to reveal/confirm more than 40 thousand new clusters in the optical and infrared bands, which represents a new era for cluster cosmology as well as for understanding the physical processes that govern the evolution of these structures. This project proposes to address the problem of modeling the galaxy cluster population in the context of LTB models, and the development of new numerical tools that may be used to provide ways of confronting model predictions with observations from galaxy surveys (e.g. Euclid) and the Cosmic Microwave Background (CMB) (such as Planck).

The work of this thesis consists of gathering an in-depth knowledge of the machinery of the Planck Sky Model (PSM) code, identifying and modifying the key functions and procedures according to a LTB framework. More specifically, we employed the non-homogeneous isotropic Constrained Garcia-Bellido-Haugbølle (CGBH) model which is completely specified by the matter density profile of the large-scale void. Our focus is on the Delabrouille, Melin, Bartlett (DMB) method, implemented by the PSM, which we here modify to a LTB framework. This method computes the thermal and kinetic Sunyaev-Zel'dovich (SZ) components of the CMB, which are well-known and effective probes of structure formation. The dominant SZ effect is the thermal effect and is this component that we modified in this thesis to extend the DMB method in the PSM to LTB models. To assist our modified version of the DMB method we made use of the Bubble code which outputs the relativistic exact solutions in LTB framework. In a first stage, we changed only the PSM functions related to the background properties of the cosmos, and then in a second stage the same was undertaken to include modifications in the functions concerning the mass function and the growth of perturbations. We named these two steps as "zero-order" and "first-order" modifications, respectively. The PSM then computes all-sky SZ effect maps, using the HEALPix tessellation tool, and galaxy cluster catalogues generated by our modified version of the DMB method. Having the maps, we were able to perform a fast statistical analysis obtaining the histogram of the distribution of pixels and its key (first four) moments, one of them being the mean SZ comptonization parameter $\overline{y_{SZ}}$ that has been constrained by CMB satellite observations by the COBE-FIRAS experiment. We then explored the evolution of the power spectra,

the thermal SZ maps and of the $\overline{y_{SZ}}$ signal as the parameters of the CGBH model vary. We also compare our results to two different FLRW cosmologies: a critical and a Λ CDM "concordance" model. Finally, the code generated catalogues of galaxy clusters which allow to generate, for the first time, mock simulations of clusters. This is a crucial tool to characterise systematic effects and estimate covariance matrices for parameter inference with cluster observables in galaxy surveys. Having the catalogues and maps, the future steps would be to confront theoretical predictions against SZ (Planck) observations and optical catalogues from existing galaxy surveys (eg SDSS/MAXBSG). The study in this project is timely and innovative. This is the first time the galaxy cluster population is modelled in the LTB context with a set of new tools at the beginning of a new era for cluster cosmology with the ESA/Euclid satellite.

Keywords: Cosmological Principle, Non-homogeneous Universe, LTB models, Clusters of galaxies, Sunyaev-Zel'dovich effect.

Resumo

O princípio cosmológico que declara que o Universo é homogêneo e isotrópico é a base da cosmologia moderna. A próxima missão da ESA/EUCLID vai testar este paradigma sobre uma vasta escala o que permitirá perceber se os modelos não homogêneos Lemaitre-Tolman-Bondi (LTB) devem ser considerados para descrever as observações locais e a escalas intermédias de uma forma precisa. É esperado que o EUCLID revele/confirme mais de 40 mil novos enxames nas bandas do ótico e do infravermelho o que representa uma nova era para a cosmologia de enxames e para a compreensão dos processos físicos que governam a evolução destas estruturas. Este projeto propõe a abordagem do problema de modelagem da população de enxames de galáxias no contexto dos modelos LTB, e o desenvolvimento de novas ferramentas numéricas que podem ser usadas para fornecer formas de confrontar previsões de modelos com observações de levantamentos de galáxias (por exemplo o Euclid) e Radiação Cós mica de Fundo Cós mico (como o Planck).

O trabalho desta tese consiste em apreender um conhecimento aprofundado da maquinaria do código Planck Sky Model (PSM), identificando e modificando as funções e procedimentos-chave de acordo com uma metodologia LTB. Mais especificamente, utilizamos o modelo isotrópico não-homogêneo *Constrained Garcia-Bellido-Haugbølle* (CGBH) que é completamente especificado pelo perfil de densidade de matéria do vazio em grande escala. O nosso foco é o método Delabrouille, Melin, Bartlett (DMB), implementado pelo PSM, que modificámos para uma estrutura LTB. Este método calcula os componentes Sunyaev-Zel'dovich (SZ) térmicos e cinéticos do CMB, que são sondas bem conhecidas e eficazes de formação de estrutura. O efeito SZ dominante é o efeito térmico e é esse componente que modificamos nesta tese para estender o método DMB nos modelos PSM para LTB. Para auxiliar a nossa versão modificada do método DMB, usamos o código Bubble, que fornece as soluções relativísticas exatas no framework LTB. Numa primeira fase, alterámos apenas as funções PSM relacionadas com as propriedades de fundo do cosmos, e numa segunda fase o mesmo foi empreendido para incluir modificações nas funções relativas à função de massa e ao crescimento de perturbações. Nomeamos essas duas etapas de modificações de "ordem zero" e "primeira ordem", respectivamente. O PSM então calcula mapas de efeito SZ de todo o céu, usando a ferramenta de tesselação HEALPix e catálogos de aglomerados de galáxias gerados por nossa versão modificada do método DMB. Tebdo os mapas, pudemos realizar uma análise estatística rápida obtendo o histograma da distribuição dos pixels e dos seus principais (quatro primeiros) momentos, sendo um deles o parâmetro de Compton média SZ $\overline{Y_{SZ}}$ que foi restringido por observações de satélite CMB pelo experimento COBE-FIRAS.

Depois, exploramos a evolução dos espectros de potência, os mapas térmicos SZ e do sinal $\overline{y_{SZ}}$ conforme os parâmetros do modelo CGBH variam. Também comparamos os nossos resultados com duas cosmologias FLRW diferentes: um modelo crítico e um modelo de "concordância" Λ CDM. Finalmente, o código gerou catálogos de aglomerados de galáxias que permitem gerar, pela primeira vez, simulações simuladas de aglomerados. Esta é uma ferramenta crucial para caracterizar efeitos sistemáticos e estimar matrizes de covariância para inferência de parâmetros com agrupamentos observáveis em levantamentos de galáxias. Com os catálogos e mapas, as etapas futuras seriam confrontar previsões teóricas contra observações SZ (Planck) e catálogos ópticos de galáxias existentes (por exemplo, SDSS / MAXBSG). O estudo neste projeto é oportuno e inovador. Esta é a primeira vez que a população de aglomerados de galáxias é modelada no contexto LTB com um conjunto de novas ferramentas no início de uma nova era para a cosmologia de aglomerados com o satélite ESA / Euclid.

Palavras-chave: Princípio Cosmológico, Universo não-homogêneo, Modelos LTB, Enxames de galáxias, Efeito Sunyaev-Zel'dovich.

Contents

Acknowledgments	i
Abstract	ii
Resumo	iii
List of Figures	xii
List of Tables	xiii
Abbreviations	xiv
1 Introduction	1
1.1 Objectives	2
2 Theoretical Introduction	4
2.1 Introduction	4
2.1.1 LTB models	5
2.1.2 GBH Models	7
2.1.3 CGBH Models	8
2.2 Clusters of galaxies	8
2.2.1 Cluster mass function	9
2.2.2 Galaxy cluster scaling laws	12
2.2.3 The Sunyaev-Zel'dovich effect	13
2.2.4 PSM in a FLRW framework	16
2.2.5 PSM extension to LTB models	18
2.3 Numerical Tools	21

2.3.1	Planck Sky Model	21
2.3.2	Model Components	22
2.3.3	SZ component	23
2.4	HEALPix	25
2.5	CAMB	27
3	Methodology	28
3.1	Overview	28
3.2	DMB method	29
3.3	Model Parameters	29
3.4	The code	30
3.4.1	Bubble code	30
3.4.2	Zero order modifications	31
3.4.3	First order modifications	33
3.4.4	Anafast	34
3.5	Statistics	34
3.6	Testing LTB results	35
4	Results	37
4.1	Dependence of the LTB density profile on the CGBH parameters	38
4.2	Dependence of r , d_A , dV/dz , H_T and H_R on the CGBH parameters	40
4.3	Zero Order Modifications	44
4.3.1	Thermal SZ maps	44
4.3.2	Map statistics	45
4.3.3	Power Spectrum	47
4.4	First Order Modifications	47
4.4.1	Thermal SZ maps	48
4.4.2	Map statistics	50
4.4.3	Power Spectrum	52
4.4.4	Redshift dependence of the $f(t(z), r(z))$ function	54
4.5	Comparison Between Zero and First Order Modifications	55
4.6	Comparison between CGBH and FLRW	57
4.6.1	Map histogram comparison	58
4.6.2	Power Spectrum	59
4.7	Catalogues of Galaxy Clusters	60

5	Discussion	62
5.1	LTB Density profile	62
5.2	Redshift dependence of r , d_A , dV/dz , H_T and H_R	63
5.3	Zero Order Modification	63
5.4	First Order Modification	65
5.5	Comparison between Zero and First Order Modification	67
5.6	FLRW Framework and Comparison With CGBH Model	67
5.7	Catalogues of Galaxy Clusters	68
5.8	Future Steps	69
5.8.1	Cluster mocks, kinetic SZ and emulators for parameter inference	69
5.8.2	Lensing and Scaling relations	70
6	Summary	71
	References	72
	Appendices	83

List of Figures

2.1	A sphere sliced in concentric shells.	22
2.2	Thermal SZ map of 3 by 4 square degrees. Left Panel: $\Omega_m = 0.3$, $\Lambda = 0.7$, $h = 0.65$, $\Omega_b = 0.05$. Right Panel: $\Omega_m = 1$, $\Lambda = 0$, $h = 0.5$, $\Omega_b = 0.07$, from [1].	25
2.3	Orthographic view of HEALPix partition of the sphere. Light-gray shading shows one of the eight (four north, and four south) identical polar base-resolution pixels. Dark-gray shading shows one of the four identical equatorial base-resolution pixels. The grid is hierarchically subdivided with the grid resolution parameter equal to (left, right): $N_{side} = 1, 2$ and the total number of pixels equal to $N = 12 \times N_{side}^2 = 12, 48$. From [2]	26
4.1	Change in the density function profile $\Omega_M(r)$ when varying the CGBH model parameter r_0 . The fiducial model is represented by the blue line ($r_0=1.5$ Gpc).	38
4.2	Change in the density function profile $\Omega_M(r)$ when varying Δr . The fiducial model is represented by the red line ($\Delta r=0.5$ Gpc).	39
4.3	Change in the density function profile $\Omega_M(r)$ when varying Ω_{in} . The fiducial model is represented by the blue line ($\Omega_{in}=0.3$ Gpc).	39
4.4	Change in the density function profile $\Omega_M(r, t_0)$ when varying h	40
4.5	Evolution of the scale r with the redshift regarding the fiducial CGBH model.	41
4.6	Left panel: Evolution of H_T and H_R with the scale r taken at the current time for the central observer assuming a fiducial CGBH model. Right panel: Evolution of H_T and H_R with redshift assuming the fiducial CGBH model.	41
4.7	Angular diameter distance for different values of Δr . The fiducial model is the red line ($\Delta r= 0.5$ Gpc).	42

4.8	Angular diameter distance for different values of r_0 . The fiducial model is the blue line ($r_0=1.5$ Gpc).	42
4.9	Angular diameter distance for different values of Ω_{in} . The fiducial model is the blue line ($\Omega_{in}=0.3$).	42
4.10	Angular diameter distance for different values of h . The fiducial model is the red line ($h=0.675$ km/s/Mpc).	42
4.11	Volume element for different values of Δr . The fiducial model is the red line ($\Delta r=0.5$ Gpc).	43
4.12	Volume element for different values of r_0 . The fiducial model is the blue line ($r_0=1.5$ Gpc).	43
4.13	Volume element for different values of Ω_{in} . The fiducial model is the blue line ($\Omega_{in}=0.3$).	43
4.14	Volume element for different values of h . The fiducial model is the red line ($h=0.675$ km/s/Mpc).	43
4.15	Mollview projection of the thermal SZ map regarding the fiducial CGBH model.	44
4.16	Mollview projection for a CGBH model with $\Omega_{in} = 0.1$ (the remaining parameters are set to their fiducial value).	44
4.17	Mollview projection for a CGBH model with $\Omega_{in} = 0.5$ (the remaining parameters are set to their fiducial value).	45
4.18	Angular power spectrum of the CGBH model obtained using the zero order modification method, for the different values of Ω_{in} . The fiducial model is represented by the green line.	47
4.19	Mollview projection of the thermal SZ map regarding the fiducial CGBH model.	48
4.20	Gnomview thermal SZ patch regarding the fiducial CGBH model.	48
4.21	Thermal SZ map of a CGBH model with $r_0=0.750$ Gpc (the remaining parameters are set to their fiducial value).	49

4.22	Thermal SZ map of a CGBH model with with $r_0=2.5$ Gpc (the remaining parameters are set to their fiducial value).	49
4.23	Thermal SZ map of a CGBH model with $\Delta r=0.250$ Gpc (the remaining parameters are set to their fiducial value).	50
4.24	Thermal SZ map of a CGBH model with $\Delta r=0.750$ Gpc. (the remaining parameters are set to their fiducial value).	50
4.25	Thermal SZ angular power spectrum of the CGBH model for the different values of r_0	52
4.26	Thermal SZ angular power spectrum of the CGBH model for the different values of Δr	53
4.27	Thermal SZ angular power spectrum of the CGBH model for the different values of h	53
4.28	Thermal SZ angular power spectrum of the CGBH model for the different values of Ω_{in}	54
4.29	$f(t, r)$ for different values of Δr	55
4.30	$f(t, r)$ for different values of r_0	55
4.31	$f(t, r)$ for different values of Ω_{in}	55
4.32	$f(t, r)$ for different values of h	55
4.33	Thermal SZ maps of the fiducial CGBH model obtained with the zero order (left) and first order (right) modification methods.	56
4.34	Power spectra of the fiducial CGBH model: Zero order modification (green line) and first order modification (red line).	56
4.35	Thermal SZ map for the standard FLRW model with $\Omega_M = 1$	57
4.36	Thermal SZ map for the standard FLRW model with $\Omega_M = 0.3$	58
4.37	Comparison between the histograms of the distribution of pixels of the fiducial CGBH model with FLRW with $\Omega_M = 1$	59
4.38	Comparison between the power spectra of the fiducial CGBH model with $\Omega_{in} = 0.3$ (red line) and the standard FLRW model with curvature with $\Omega_M = 1$ (blue line) and with $\Omega_M = 0.3$ (green line)	60
4.39	Distribution of cluster integrated Y_{SZ} luminosities for the fiducial CGBH (zero and first order modification) model and FLRW model with $\Omega_M = 1$. These catalogues assume a minimum mass of $M_{min} = 10^{14} M_{\odot}$	61

4.40	Redshift distribution of (all-sky) galaxy cluster number counts, $N(z)$, for the fiducial CGBH model and FLRW model with $\Omega_M = 1$. These catalogues assume a minimum mass of $M_{min} = 10^{14} M_{\odot}$.	61
.1	Mollview projection of the thermal SZ map for a CGBH model with $\Omega_{in}=0.2$.	84
.2	Mollview projection of the thermal SZ map for a CGBH model with $\Omega_{in}=0.4$.	84
.3	Mollview projection of the thermal SZ map for a CGBH model with $r_0=0.750$ Gpc.	85
.4	Mollview projection of the thermal SZ map for a CGBH model with $r_0=1.0$ Gpc.	85
.5	Mollview projection of the thermal SZ map for a CGBH model with $r_0=2.0$ Gpc.	86
.6	Mollview projection of the thermal SZ map for a CGBH model with $r_0=2.5$ Gpc.	86
.7	Mollview projection of the thermal SZ map for a CGBH model with $\Delta r=0.250$ Gpc.	87
.8	Mollview projection of the thermal SZ map for a CGBH model with $\Delta r=0.750$ Gpc.	87
.9	Mollview projection of the thermal SZ map for a CGBH model with $h=0.625$ km/s/Mpc.	88
.10	Mollview projection of the thermal SZ map for a CGBH model with $h=0.65$ km/s/Mpc.	88
.11	Mollview projection of the thermal SZ map for a CGBH model with $h=0.675$ km/s/Mpc.	89
.12	Mollview projection of the thermal SZ map for a CGBH model with $h=0.75$ km/s/Mpc.	89
.13	Power Spectra of the CGBH model when varying h .	90
.14	Power Spectra of the CGBH model when varying Δr .	90
.15	Power Spectra of the CGBH model when varying r_0 .	91
.16	Mollview projection of the thermal SZ map for a CGBH model with $\Omega_{in}=0.1$.	92
.17	Mollview projection of the thermal SZ map for a CGBH model with $\Omega_{in}=0.2$.	92
.18	Mollview projection of the thermal SZ map for a CGBH model with $r_0=1.0$ Gpc.	93
.19	Mollview projection of the thermal SZ map for a CGBH model with $r_0=2.0$ Gpc.	93

.20	Mollview projection of the thermal SZ map for a CGBH model with $h=0.65$ km/s/Mpc.	94
.21	Mollview projection of the thermal SZ map for a CGBH model with $h=0.675$ km/s/Mpc.	94

List of Tables

3.1	Range of values for the several parameters. The parameters regarding the fiducial model are in bold.	30
4.1	Mean y -distortion and variance of the thermal SZ signal in maps obtained using the zero-order modification for the fiducial CGBH model.	45
4.2	SZ mean y -distortion and variance in maps obtained using the zero-order modification when varying Δr	46
4.3	SZ mean y -distortion and variance in maps obtained using the zero-order modification when varying h	46
4.4	SZ mean y -distortion and variance in maps obtained using the zero-order modification when varying Ω_{in}	46
4.5	SZ mean y -distortion and variance in maps obtained using the zero-order modification when varying, r_0	46
4.6	SZ mean y -distortion and variance in maps obtained with the first order modification methods for the fiducial CGBH model.	51
4.7	SZ mean y -distortion and variance in maps obtained with the first order modification method when varying Δr	51
4.8	SZ mean y -distortion and variance in maps obtained with the first order modification method when varying h	51
4.9	SZ mean y -distortion and variance in maps obtained with the first order modification method when varying Ω_{in}	51
4.10	SZ mean y -distortion and variance in maps obtained with the first order modification method when varying r_0	52
4.11	SZ mean y -distortion and variance in maps regarding the FLRW model with $\Omega_M = 0.3$ and $\Omega_M = 0.1$	58

Abbreviations

CAMB - Code for Anisotropies in the Microwave Background

CMB - Cosmic Microwave Background

FLRW - Friedmann-Lemaitre-Robertson-Walker

HEALPix - Hierarchical Equal Area IsoLatitude Pixelization

LTB - Lemaitre-Tolman-Bondi

PSM - Planck Sky Model

SZ - Sunyaev-Zel'dovich

Λ CDM - Lambda Cold Dark Matter model

CGBH - Constrained Garcia-Bellido-Haugbølle

Chapter 1

Introduction

The cosmological principle together with the Einstein's equations leads to the popular homogeneous and isotropic Friedmann-Lemaitre-Robertson-Walker (FLRW) models that have become the present baseline paradigm to analyze and predict large-scale cosmological datasets. We have enough evidence that justifies the homogeneity and isotropy of the Universe at large scales but at small scales we know for sure that this picture is not accurate. In FLRW models, large scales translate into scales around 100Mpc. The Λ CDM framework provides a very good fit to various datasets, but it contains some open issues [3]. As an example, there are inconsistencies between probes: the tension between CMB primary signal (Planck) and weak lensing (CFHTLenS) [4], and more recently the combined KV450 + DES-Y1 constraint on the weighted amplitude of matter fluctuations S_8 parameter is in tension with the Planck 2018 constraint from the CMB [5].

One of the current challenges of cosmology research is to find a scale in which the Universe is no longer homogeneous. When the homogeneity is no longer a prerequisite, the models fall into the category of a more general non-homogeneous isotropic LTB models, which contain the FLRW model. The main motivation of this project is then to describe the Universe at intermediate cosmological (and local) scales in a way that may describe observations better than the standard homogeneous and isotropic FLRW paradigm. Noting that everything depends on the very definition of redshift, the different observed tensions could be resolved by turning to a different framework of non-homogeneous models. When interpreting the results from the light coming from the distant clusters, one could possibly eliminate these tensions by assuming a non-homogeneous and isotropic space-time. One possible outcome of these LTB studies is conjecturing that the scale of transition lies at a

redshift so low that its impact in cosmology is low, having only a local influence, giving rise to removable dipoles with regard to our planet's and milky way's velocity. While exploring the framework of non-homogeneous LTB models we are interested in studying the radial variations of the average matter density (density profiles) that are compatible with observations. The way the density profile is chosen from the observer and the scale where the Universe begins to be described by a FLRW metric can be itself a method to parameterize these kind of models. One way to test models is to use galaxy cluster information from multi-wavelength observations, such as in the optical, X-rays and Cosmic Microwave Background (CMB/SZ observations). This research is relevant for the forthcoming ESA/Euclid satellite mission that will test the cosmological principle paradigm over a wide range of cosmological scales with a variety of probes [6]. The Euclid mission will map billions of galaxies out to a distance of 10 billion light-years. Using all-sky galaxy clusters identification algorithms, one of the outcomes of this mission will be the production of large catalogues of galaxy clusters. Those catalogues contain the average redshift of every cluster, the total mass of their objects as well as the number of galaxies and their type. These catalogues of galaxy clusters allow us to generate mock simulations of clusters. The covariance matrixes are calculated based on these simulations which is crucial for cosmological parameter determination. The Euclid survey, alone, is expected to reveal more than 60 thousand clusters with signal-to-noise ratio greater than 3, up to redshift $z = 2$ (10 thousand of this will be high redshift clusters with $z > 1$) [6].

1.1 Objectives

The main target is then to model galaxy cluster populations in a LTB framework. Since we are looking for a scale of transition between a non-homogenous and a homogeneous Universe, we explored the density profiles - the radial variation of the matter density parameter $\Omega(r, t)$ - in LTB models, using parameters that allow the matter density and the Hubble parameter in LTB to asymptotically approach the FLRW values below a redshift transition, z_t . There are a set of analytical and semi-analytical methods that allow us to fill, shell by shell, the Universe with dark matter halos in the same way that it was performed for the Planck Mission. The expressions that we use in our models are normalized to observations, that is, they reflect observations or empirical relations. The PSM is a software package, originally developed in the context of the Planck mission, to produce simulations of all the CMB foregrounds (primary, secondary and tertiary [7])

including simulated galaxy cluster catalogues and all-sky CMB/SZ effect maps. Besides cluster profiles and mass functions, scaling relations are also a key component to relate observations with cluster properties. One of the main tasks then is to develop a fast semi-analytical algorithm using the PSM code that populates the Universe with dark matter halos derived from a halo mass function (that determines the abundance of clusters in each shell, giving the number of objects by unit of volume) and their observational profiles (that describe the mass distribution around the haloes' centre). The several shells are populated in an identical way as in FLRW but the matter density function evolves as in a LTB framework. More precisely, the Sunyaev–Zeldovich (SZ) component of the PSM code has been modified to a LTB framework as it is a cosmological probe widely employed to measure the properties of gas in clusters of galaxies and studying the evolution of structure in the Universe. The PSM then provides not only LTB maps for the thermal and kinetic SZ component but also catalogues of all the clusters and their position in the sky, their mass, the Y_{SZ} signal, cluster temperature and velocity at all redshifts. These generated catalogs are crucial for further incoming scientific research. This procedure is key to compute covariance functions and the likelihood of number counts in order to make inference on the different cosmological parameters for these models. These catalogues allow us to obtain for the first time mock simulations of clusters that can be used to test systematic effects and determine covariance matrixes of observable cluster quantities from galaxy surveys in an LTB framework. This studies are essential to further test the cosmological principle with galaxy surveys, such as EUCLID. This is one of the main motivations of this work. The PSM code is built to apply several type of cosmologies using any set of cosmological parameters which is a great advantage comparing to time-consuming N-body simulations. These maps and catalogues in LTB models is something that does not yet exist in scientific literature. Further methods to study the viability of the LTB models and expected results are presented in Section 5.8. The end result will consist of generating thermal SZ maps in the framework of LTB models, computing the related angular power spectrum and mean SZ signal, $\overline{y_{SZ}}$, and finally generating galaxy cluster catalogues.

Chapter 2

Theoretical Introduction

2.1 Introduction

In the era when observational cosmology is becoming ever more precise, many *a priori* assumptions are still employed before interpreting data from observations. The latest results from the Planck mission [8], assuming the base- Λ CDM cosmology, yield the following model-dependent parameters: a Hubble constant of $H_0 = (67.4 \pm 0.5) \text{ km s}^{-1} \text{ Mpc}^{-1}$, a matter density parameter of $\Omega_m = 0.315 \pm 0.007$ and a matter fluctuation amplitude $\sigma_8 = 0.811 \pm 0.006$. As stated in [8], there are some unresolved tensions concerning the Dark Energy Survey’s combined-probe results including galaxy clustering and tensions with local measurements of the Hubble constant. More recently, results from KV450 + DES-Y1 [5] constraint on S_8 is in tension with the Planck 2018 constraint from the CMB at the level of 2.5σ [8]. For many decades the scientific community has made use of the Cosmological Principle which assumes total symmetry (homogeneity and isotropy) regarding the spatial coordinates. Many have questioned if this assumption is consistent and if indeed it is the best model to describe observations. This symmetries are “expected to be valid on very large scales”, but do we know precisely how large this scale should be? We are aware that our solar system and our Local Group is far from being homogeneous so, how should we interpret present observations coming from an inhomogeneous Universe if we assume a homogeneous one? As it is indeed observed a high isotropic CMB, several versions of these spherically symmetric inhomogeneous models also named Lematre-Tolman-Bondi (LTB) [9, 10, 11] models have been proposed.

2.1.1 LTB models

In the standard FLRW Universe, space-time is characterised by functions such as the Hubble rate $H(t)$ and the density parameter $\Omega(t)$, that depend on cosmic time but are independent of the radial coordinate r . In LTB models these arbitrary functions, e.g. $H(r, t)$ and $\Omega(r, t)$ are generally dependent on both time and on the radial coordinate. Here we are assuming $c=1$. The general line element satisfying spherically symmetric spatial sections can be written as [12]:

$$ds^2 = -dt^2 + X^2(r, t) dr^2 + A^2(r, t) d\Omega^2 1, \quad (2.1)$$

where $d\Omega^2 = d\theta^2 + \sin^2 \theta d\phi^2$ is the solid angle. Here, $A(t, r)$ plays the role of a scale function that can depend both on time and radial coordinates. X and A are related as:

$$X(r, t) = A'(r, t) / \sqrt{1 - k(r)}, \quad (2.2)$$

where $k(r)$ is an arbitrary function playing the role of the spacial curvature parameter related to the energy function $E(r)$ as $k(r) = -2E(r)$. Here, prime denotes partial derivative with respect to the coordinate r . One can note that assuming homogeneity conditions we recover the usual FRLW metric:

$$A(r, t) = a(t) r, \quad k(r) = k r^2, \quad (2.3)$$

where $a(t)$ is the FLRW scale factor and r the comoving distance. In LTB models there are two rates of expansion, the transverse and longitudinal:

$$H_T(r, t) \equiv \frac{\dot{A}(r, t)}{A(r, t)}, \quad (2.4)$$

$$H_L(r, t) \equiv \frac{\dot{A}'(r, t)}{A'(r, t)}. \quad (2.5)$$

In general, these two functions will be different as long as the space-time is inhomogeneous. In homogenous models, these two quantities are not distinguishable. One can define a mean

¹The Bubble code employs a slightly different metric written as $ds^2 = dt^2 - \frac{a_2^2(t, r)}{1 - k(r)r^2} dr^2 - a_1^2(t, r)r^2 d\Omega^2$, where $a_2 = (a_1 r)'$, and where a_1 must satisfy $\left(\frac{\dot{a}_1}{a_1}\right)^2 = \frac{8\pi G}{3} \frac{m(r)}{a_1^3} - \frac{k(r)}{a_1^2}$

Hubble factor through an arithmetic mean as [12]:

$$\langle H \rangle = \frac{1}{3}(2H_T + H_L), \quad (2.6)$$

The matter content is represented by a inhomogeneous fluid that is pressureless. Therefore, the stress-energy tensor can be written as [13]

$$T_{\nu}^{\mu} = -\rho(r, t) u^{\mu} u_{\nu} \quad (2.7)$$

where u^{μ} is the four-velocity field of the fluid. Due to the symmetries of the line element, the analogue Friedmann-like equation is:

$$H_T^2 - \frac{2E}{A^2} = \frac{2M}{A^3}, \quad (2.8)$$

where $M(r)$ is another free function of r that can be interpreted as the gravitational mass inside a spherical shell of radius r . A dimensionless matter and curvature density parameters evaluated today can be written as [13]:

$$\Omega_M(r) = \frac{2M(r)}{H_{T0}^2(r)A_0^3(r)}, \quad (2.9)$$

$$\Omega_k(r) = \frac{2E(r)}{H_{T0}^2(r)A_0^2(r)}. \quad (2.10)$$

In order to compare the LTB model with observations it is necessary to construct the light paths. This is accomplished by solving the appropriate null geodesics for the model. By symmetry, incoming light travels along radial null geodesics, $ds^2 = d\Omega^2 = 0$, and time decreases when going away, $dt/dr < 0$ [12], so:

$$\frac{dt}{dr} = -\frac{A'(r, t)}{\sqrt{1 - k(r)}}. \quad (2.11)$$

Combining with the redshift equation:

$$\frac{d \log(1 + z)}{dr} = \frac{\dot{A}(r, t)}{\sqrt{1 - k(r)}}, \quad (2.12)$$

this can be written as a parametric set of differential equations, with $N = \log(1 + z)$ being

the effective number of e-folds before the present time,

$$\frac{dt}{dN} = -\frac{A'(r, t)}{\dot{A}(r, t)}, \quad (2.13)$$

$$\frac{dr}{dN} = \frac{\sqrt{1 - k(r)}}{\dot{A}(r, t)}. \quad (2.14)$$

From here, not only the functions $t(z)$ and $r(z)$ can be obtained but also the luminosity distance, the comoving distance and the angular diameter distance as a function of redshift [13]. In LTB models the angular diameter distance measured by an observer at the center is directly related to the scale function $A(r, t)$:

$$d_L(z) = (1 + z)^2 A[r(z), t(z)], \quad (2.15)$$

$$d_C(z) = (1 + z) A[r(z), t(z)], \quad (2.16)$$

$$d_A(z) = A[r(z), t(z)]^2. \quad (2.17)$$

The r -dependent Hubble rate is written as [12]

$$H^2(r, t) = H_T^2(r, t) = H_0^2(r) \left[\Omega_M(r) \left(\frac{A_0(r)}{A(r, t)} \right)^3 + (1 - \Omega_M(r)) \left(\frac{A_0(r)}{A(r, t)} \right)^2 \right]. \quad (2.18)$$

and the "effective" acceleration parameter $q(z)$ [12] can be defined as:

$$q(z) = -1 + \frac{d \ln H(z)}{d \ln(1 + z)}, \quad (2.19)$$

where $H(z)$ is $H_L(r(z), t(z))$.

2.1.2 GBH Models

Garcia-Bellido and Haugbølle [12] proposed a void-like model with six parameters that is completely characterized by the matter density $\Omega_M(r)$ and the transverse expansion rate today $H_{t0}(r)$. These kind of models are asymptotically Einstein-de Sitter which is a cosmological model for a flat matter-only FLRW Universe. Their parameterization fixes the inner and outer values of Ω_M and H_{t0} and also how large and smooth is the transition from the inner and outer regions of the void:

$$\Omega_M(r) = \Omega_{\text{out}} + (\Omega_{\text{in}} - \Omega_{\text{out}}) \left(\frac{1 - \tanh[(r - r_0)/2\Delta r]}{1 + \tanh[r_0/2\Delta r]} \right) \quad (2.20)$$

$$H_0(r) = H_{\text{out}} + (H_{\text{in}} - H_{\text{out}}) \left(\frac{1 - \tanh[(r - r_0)/2\Delta r]}{1 + \tanh[r_0/2\Delta r]} \right) \quad (2.21)$$

Here, Ω_{out} is determined by asymptotic flatness, Ω_{in} is determined by LSS observations, r_0 characterises the size of the void, H_{out} is determined by CMB observations, H_{in} is determined by HST observations and Δr characterises the transition to uniformity. For instance, a smaller Δr translates into a swifter transition and a model with $r_0=1.5$ Gpc has a void of that size. The goal is to employ $\Omega(r)$ that approximates to the constant Ω_{out} , in other words, to asymptotically approach the FLRW limit at large ($r \gg r_0$) radi.

2.1.3 CGBH Models

The authors also created a simpler and more constrained model in which the Big Bang is homogeneous, that is, the spatial hypersurface at the Big Bang does not depend on the radial coordinate r [12]. This extra condition imposes a relation between the expansion rate and the matter density and hence this model has only a single free function. This is obtained by a choice of $H_0(r)$:

$$H_0(r) = H_0 \left[\frac{1}{\Omega_K(r)} - \frac{\Omega_M(r)}{\sqrt{\Omega_K^3(r)}} \sinh^{-1} \sqrt{\frac{\Omega_K(r)}{\Omega_M(r)}} \right], \quad (2.22)$$

where $\Omega_k + \Omega_M = 1$ and

$$t_{\text{BB}} = c H_0^{-1}, \quad (2.23)$$

the age of the Universe, is universal for all observers regardless of their spatial location. There is less freedom in this model as now there is only one arbitrary function, $\Omega_M(r)$, and there is one free parameter less. Plots of $\Omega_M(r)$ when the several parameters vary are presented in Section 4.1.

2.2 Clusters of galaxies

Clusters of galaxies are the largest gravitationally bound bodies in the Universe and are one of the latest bound structures forming in the cosmos [14, 15]. For this reason,

their number density is extremely sensitive to the growth rate and power spectrum of density perturbations as well as to cosmological background parameters like the matter density and the Hubble parameter. Hence, cluster abundance is a thoroughly established cosmological probe. The SZ effect is one of the most useful properties of the clusters and it will be addressed in the next subsection. The main components required for our methodology regarding galaxy clusters are the mass function, the cluster profiles and their scaling relations.

The most massive galaxies have masses typically smaller than $10^{12}M_{\odot}$. For clusters of galaxies the range of mass varies between 10^{14} and $10^{15}M_{\odot}$. At redshift $z=5$ there are galaxies but galaxy clusters are extremely rare. At that redshift the Universe is too young to have formed galaxy clusters and as such the thermal SZ effect is mainly produced by ionized gas in filaments [16]. The main quantity that goes into the computation of the expected abundance of clusters for a given cosmological scenario is the mass function, $n(M, z)$ which gives the comoving number density of virialized halos forming within infinitesimal range around redshift z and mass M , according to [14]. Then, the redshift distribution of observed galaxy cluster abundances can be compared against model predictions using the following expression [17]:

$$N(z) = \frac{dV}{dzd\Omega} \int_0^{\infty} \frac{dn(M, z)}{dM} f_{\text{survey}}(M, z) dM. \quad (2.24)$$

Here, $N(z)$ is the number of clusters per unit redshift per unit solid angle, $dV/dzd\Omega$ is the volume element of the underlying model, and $f_{\text{survey}}(M, z)$ is the cluster survey selection function. Setting $f_{\text{survey}} = 1$ and assuming that it is possible to observe all cluster masses, (2.24) gives the full redshift distribution of halos in the Universe. Now we can write the total number of objects with mass bigger than M_{min} per unit of solid angle [18]. This equation is obtained by integrating Eq. (2.24) in redshift and by assuming that f_{survey} is a unit step function centered in M_{min} :

$$N(> M_{\text{min}}) = \int_0^{\infty} \frac{dV}{dzd\Omega} \int_{M_{\text{min}}}^{\infty} \frac{dn}{dM} dM dz. \quad (2.25)$$

2.2.1 Cluster mass function

The predictions for the abundance of collapsed objects are usually quantified as a function of their mass and redshift, i.e., in terms of the mass function $n(M, z)$. The general expression

for the mass functions that was firstly derived in the Press–Schechter (PS) formalism and different mass functions may be written with a general expression, as [17]³:

$$\frac{dn}{dM} = f(\sigma) \frac{\bar{\rho}_m}{M} \frac{d \ln \sigma^{-1}}{dM} \quad (2.26)$$

The different mass functions differ in the $f(\sigma)$ function. This function is expected to be universal to the changes in redshift and cosmology. In the Press–Schechter case it is given by:

$$f(\sigma) = -\sqrt{\frac{2}{\pi}} \frac{\delta_c}{\sigma^2} \exp\left(-\frac{\delta_c^2}{2\sigma^2(M, z)}\right). \quad (2.27)$$

Here ρ_0 is the comoving matter density which in FLRW is $\rho_0 = \Omega_{M0} \rho_{crit}$ and δ_c is the linear overdensity threshold at collapse that can be computed in linear perturbation theory. For LCDM models of interest it is often set to $\delta_c = 1.686$ due to its mild dependence on z , [19]. $\sigma^2(R(M), z)$ is the variance of the smoothed density contrast filtered on the comoving scale $R(M)$, and M is the mass enclosed in the volume occupied by a top-hat filter, $M = \rho_m V$ where ρ_m is the background density of the universe. § The quantity σ is the root mean square of the variance of the smoothed overdensity field, see e.g. [18], that can be computed from the matter power spectrum as:

$$\sigma^2 = \int P(k)W(kR)k^2 dk, \quad (2.28)$$

where P_k is the power spectrum which has a well determined shape for a given cosmological model, k is the wave number and W is the Fourier transform of the real-space top-hat window function of radius R . The normalization of the power spectrum can be made by computing σ at the $R = 8h^{-1}$ Mpc scale at the present time, which is represented by the $\sigma_8(z=0)$ parameter. The normalization of the power spectrum at this scale, is often achieved from the observation of the abundance of galaxy clusters. The CMB also allow us to normalize the power spectrum, but at larger physical scales, i.e. at a lower k .

³The mass function is usually written in several ways: $\frac{dn}{dM}$, $\frac{dn}{dM dz}$ or $\frac{dN}{dV dM dz}$. In this work the notation $\frac{dn}{dM}$ or $\frac{dn}{dM dz}$ is employed to represent $n(M, z)$.

There are other mass functions like the Jenkins, Sheth and Tinker [20, 21, 22, 23]. In particular, the PSM code implements a Tinker mass function which employs [23]:

$$f(\sigma) = A \left[\left(\frac{\sigma}{b} \right)^{-a} + 1 \right] e^{-c/\sigma^2}. \quad (2.29)$$

The first three parameters of $f(\sigma)$ are allowed to vary as a power law of $1+z$:

$$A(z) = A_0 (1+z)^{-0.14}, \quad (2.30)$$

$$a(z) = a_0 (1+z)^{-0.06}, \quad (2.31)$$

$$b(z) = b_0 (1+z)^{-\alpha}, \quad (2.32)$$

$$\log \alpha(\Delta) = - \left(\frac{0.75}{\log(\Delta/75)} \right)^{1.2}, \quad (2.33)$$

where subscript ‘0’ indicates the value obtained at $z = 0$ for the different parameters: $A_0=0.186$, $a_0=1.47$, $b_0=2.57$, $c=1.19$ and $\Delta=200$ [23].

According to [24, 18, 25], the rms (σ) of the fluctuations can be approximated by the following fitting formula, derived from cluster observations:

$$\sigma = \sigma_8(z) \left(\frac{R}{8h^{-1} \text{Mpc}} \right)^{-\gamma(R)}, \quad (2.34)$$

considering a Top-Hat filter with $R = (3M/4\pi\Omega\rho_{crit})^{1/3}$, where $\sigma_8(z)$ is described below and

$$\gamma(R) = (0.3\Gamma + 0.2) \left[2.92 + \log \left(\frac{R}{8h^{-1} \text{Mpc}} \right) \right]. \quad (2.35)$$

Γ is the shape parameter of the power spectrum. It is typically obtained by fitting the power spectrum obtained with Boltzmann codes and controls how fast the power decreases at small scales. According to [26], $\Gamma = \Omega_0 h \exp[-\Omega_{B0}(1 + \sqrt{2h}/\Omega_0)]$.

The normalization and redshift dependence of the mass function is related to the amplitude of the linear matter power spectrum at a redshift z and is given by $\sigma_8(z) = \sigma(R = 8h^{-1}\text{Mpc}, z)$ [24]:

$$\sigma_8(z) = \frac{\sigma_8(0) g[\Omega(z), \Omega_\Lambda(z)]}{1+z g[\Omega_0, \Omega_{\Lambda 0}]}, \quad (2.36)$$

where $\sigma_8(0)$ is the power spectrum normalization at the present and $g(z)$ is the linear growth factor, which for Λ CDM models is a function of the density parameters [18]:

$$g(z) = g(\Omega_m(z), \Omega_\Lambda(z)), \quad (2.37)$$

An explicit fitting formula of $g(z)$ was provided by [27]:

$$g[\Omega(z), \Omega_\Lambda(z)] = \frac{5}{2} \Omega(z) \left[\Omega(z)^{4/7} - \Omega_\Lambda(z) + \left(1 + \frac{1}{2} \Omega(z)\right) \left(1 + \frac{1}{70} \Omega_\Lambda(z)\right) \right]^{-1}. \quad (2.38)$$

The value of $\sigma_8(z)$ can be calculated using this semi-analytical function or by direct computation of Eq. (2.28) on the scale of 8 Mpc for a given matter power spectrum shape and filter. The PSM code automatically calculates the value of $\sigma_8(z)$ integrating the power spectrum for Friedmann models.

2.2.2 Galaxy cluster scaling laws

The simplest model describing cluster scaling relations is assuming, among other things, that gravity is the dominating force and clusters of different masses are self-similar replicas of each other. Under these assumptions the cluster scaling models are parameterized as power laws of the form [17]:

$$Y = A E(z)^{\beta_{ss}} (X/X_0)^{\alpha_{SS}}, \quad (2.39)$$

where Y and X are cluster properties, A is a normalization parameter giving the amplitude of Y at $X = X_0$, $E(z) = H(z)/H_0$, α_{SS} is the power law index of the (independent) property X , and β_{ss} is a parameter giving the self-similar evolution of the normalization. The parameters α and β_{ss} can be computed analytically within an extended self-similar modelling that also assumes that the baryon gas component in clusters is in hydrostatic equilibrium. In general, the amplitude parameter A may itself be a function of redshift and if so, it evolves in a non self-similar way, usually parameterized by a power-law of redshift, $A(z) = A_0(1+z)^\beta$.

In general, the galaxy clusters scaling laws involve mass, M , SZ integrated signal, Y , X-ray temperature, T_X and luminosity, L_X [28]:

$$T_X = A_{TM} (M/M_0)^{\alpha_{TM}} (1+z)^{\beta_{TM}} E(z)^{2/3}, \quad (2.40)$$

$$L_X = A_{LM} (M/M_0)^{\alpha_{LM}} (1+z)^{\beta_{LM}} E(z)^{7/3}, \quad (2.41)$$

$$Y = A_{YM} (M/M_0)^{\alpha_{YM}} (1+z)^{\beta_{YM}} E(z)^{2/3}. \quad (2.42)$$

For clusters, the normalisation scales are typically $M_0 = 10^{14} h^{-1} M_\odot$ and $T_{X,0} = T_{\text{mw},0} = 1 \text{ keV erg/s}/h^2$ following the same reference. The quantities A , α , and β are the scalings normalisation at $M = M_0$ and $z = 0$, the power index on the independent variable and the departures from the expected redshift evolution, respectively. The PSM code, when employing the DMB method, implements (2.40) and (2.42). A future step, as described in Section 5.8, would be adding to the PSM code cluster scaling relations relating cluster richness quantity N , with the SZ integrated signal and mass:

$$N = A_{NY} E(z)^{2/3} (1+z)^{\beta_{NY}} (Y/Y_0)^{\alpha_{NY}}, \quad (2.43)$$

$$N = A_{NM} E(z) (1+z)^{\beta_{NM}} (M/M_0)^{\alpha_{NM}}. \quad (2.44)$$

2.2.3 The Sunyaev-Zel'dovich effect

The Sunyaev–Zel'dovich (SZ) effect is the change in energy experienced by CMB photons when they scatter from intervening gas, especially that in galaxy clusters [29], [17]. The primordial CMB signal has been widely employed to constrain cosmological parameters and now the SZ effect is becoming an effective probe of structure formation. There are two contributions for this effect, the thermal and the kinetic one. Both thermal and kinetic SZ effects are actually Doppler's effects. The velocity of an electron can be decomposed in two components: the velocity of the mass center of the cloud, where the electron is, and the electron's velocity around the cloud's mass center. The kinetic SZ effect is the Doppler shift arising from the bulk motion of the gas [30]. In other words, it represents the cloud's own velocity and is the Doppler's effect that arises from that bulk velocity of all electrons in the cloud. Therefore, the kinetic effect translates the radial component of the cluster's velocity with respect to the observer. But, at the same time, each electron has a movement with respect to the cloud's center due to thermal motion, giving rise to the thermal SZ effect. The dominant effect from clusters is the thermal SZ effect which is the gain in energy of photons acquired from the thermal motion of the gas which is commonly at a temperature of tens of millions of degrees in clusters. Our focus is on the thermal contribution because for typical cluster velocities and optical depths, the thermal SZ effect is the dominant one. The CMB spectral distortion caused by the thermal effect is given by [31]:

$$\Delta I_{\text{th}} = I_0 g(x) y, \quad y = \frac{k_B \sigma_T}{m_e c^2} \int T_e n_e dl, \quad (2.45)$$

where $I_0 = 2k_B^3 T^3 / h^2 c^2$, y is the line-of-sight Compton SZ parameter, T_e is the electron temperature, n_e is the electron number density, and $g(x)$ is a function giving the frequency dependence of the effect.

The total SZ signal integrated over the sky angular size of a cluster is well approximate by

$$Y \equiv \int y d\Omega = d_A^{-2} \int y dA = \frac{k_B \sigma_T}{m_e c^2} d_A^{-2} \int_V T_e n_e dV, \quad (2.46)$$

where d_A is the angular diameter distance from the observer to the cluster. This equation is the cluster volume integrated SZ Y -flux or Y -luminosity and is a measure of the total thermal energy density of the cluster. The y -flux is also called the integrated pressure. Throughout this work this quantity is denominated by Y_{SZ} .

In this thesis we assume, in the DMB method of the PSM code, an isothermal beta profile for galaxy clusters where the electron density n_e that generates the SZ effect is: [1]:

$$n_e(r) = n_e(0) \left(1 + \left(\frac{r}{r_c} \right)^2 \right)^{-3\beta/2}, \quad (2.47)$$

where $\beta \approx 2/3$. These isothermal models assume that the temperature remains constant through the cluster which is a common approximation to take on. In reality, temperature decreases slightly as we advance to the outskirts of the cluster. In order to calculate the SZ effect we also need the temperature of the electrons, T_e . Since we are working with isothermal profiles and temperatures, T_e is obtained by a scale relation that depends solely on the mass and on the cosmological parameters. At each redshift, the r in Eq. (2.47) will be angularly scaled since there is a relation between the physical size of the object and the its redshift, given by the angular diameter distance. A gas temperature-mass relation normalized to numerical simulations used in the PSM code is:

$$T_e = 6.8 h^{2/3} \left(\frac{M}{10^{15} M_\odot} \right)^{2/3} \left(\frac{\Omega_m \Delta_{NL}(z)}{178} \right)^{1/3} (1+z) \text{ keV} \quad (2.48)$$

where $\Delta_{NL}(z)$ is the non-linear density contrast on collapse.

The PSM generates a number of objects at each redshift according to the mass function.

Since the goal is to compute the integrated SZ signal, we will employ an empirical relation between the mass and the SZ signal that a particular mass assembles in the sky [32]:

$$\begin{aligned}
Y_{500} &= 1.383 \times 10^{-3} I(1) \left(\frac{M_{500}}{3 \times 10^{14} \text{M}_{\odot}} \right)^{\frac{1}{\alpha_{MYX}}} \\
&\times E(z)^{2/3} \left(\frac{d_A(z)}{500 \text{Mpc}} \right)^{-2} \text{arcmin}^2, \tag{2.49}
\end{aligned}$$

where Y_{500} is the SZ flux in R_{500} , $I(1) = 0.6145$ is a numerical factor arising from the volume integral of the pressure profile, $d_A(z)$ is the angular distance and $\alpha_{MYX} = 0.561$. M_{500} is the mass embedded in a ratio whose density is 500 times the critical density. The equation above relates the mass with the integrated SZ signal that the same mass produces in the sky.

If clusters are too away from the observer they only cover one pixel in the sky and there is no need to employ the gas profile due to their small angular size. On the other hand, for nearby clusters we need to compute its profile. For remote clusters the procedure is straightforward since it is only necessary to translate mass into Y_{SZ} . For the others their profile is computed and the fraction of signal is added to the pixel to build up along the line-of-sight. An important statistic to derive from sky maps of the SZ effect is the angular power spectrum of the thermal and kinetic SZ temperature fluctuations. The angular power spectra tells us what is the contribution to the total power in the sky of objects of a certain angular size. The mass function plays a key role as it describes how many objects of a certain size/mass lie on a certain redshift. The multipole moment ℓ is related to the angular scale θ as $\ell \approx 1/\theta$ [33]. Therefore, small multipoles translate into large angular-size objects in the sky. Analytically, the angular power spectrum of the thermal SZ signal can be computed as a sum of two terms: $C_l^{total} = C_l^{Poisson} + C_l^{clustering}$, where $C^{Poisson}$ or C_l^{1halo} is the power spectrum resulting from a Poisson distribution of objects (clusters) and $C_l^{clustering}$ is a “2-halo” or clustering term giving the ℓ power arising from object (cluster two-point) correlations. The first term accounts for intra-halo correlations and the second

for inter-halo ones. These terms can be computed as [34]:

$$C_\ell^{\text{Poisson}} = \int_0^{z_{\text{max}}} \frac{dV}{dz d\Omega} \int_{M_{\text{min}}}^{M_{\text{max}}} \frac{dn(M, z)}{dM} |y_\ell(M, z)|^2 dM dz, \quad (2.50)$$

$$C_\ell^{\text{clustering}} = \int_0^{z_{\text{max}}} \frac{dV}{dz d\Omega} P(k) \times \left[\int_{M_{\text{min}}}^{M_{\text{max}}} \frac{dn(M, z)}{dM} b(M, z) y_\ell(M, z) dM \right]^2 dz \quad (2.51)$$

where y_ℓ is the 2D Fourier transform of the matter power spectrum at redshift z , and $b(M, z)$ is the linear bias factor that relates the matter power spectrum, $P(k, z)$, to the cluster correlation power spectrum $P_{\text{cluster}}(k, M_1, M_2, z) = b(M_1, z)b(M_2, z)D^2(z)P(k, z=0)$. The mass and redshift range of the integrations are chosen so as to cover all relevant SZ source contributions up to high enough redshift. The halo/Poisson term translates the effect of having isolated objects on the map without being correlated. It depends on the volume element, on the mass limits and on the cluster's profile through y_ℓ . The clustering term accounts for the fact that large-scale clusters are not randomly aligned on the sky, rather they are aligned through the cosmic web, the filaments, and therefore correlations arise. The procedures employed in this work only account for the first term (2.50) where there is no clustering as clusters are drawn in the sky maps without accounting for correlations. Observationally, the thermal SZ all sky anisotropies can be separated from the overall CMB signal by applying component separation techniques that make use of the spectral signature and scale of the SZ effect. The first all-sky maps of the thermal SZ effect were produced from Planck observations [35]. These studies allowed to investigate the distribution of the y -signal and characterize its higher order statistics, such as the angular power spectrum and bi-spectrum. The observed thermal SZ power spectrum was confirmed to be very sensitive to cosmological parameters, especially σ_8 and Ω_{m0} , but these are strongly degenerate with the mass bias parameter b (they found that $\sigma_8(\Omega_{m0}/0.28)^{3/8} = 0.80_{-0.03}^{+0.01}$ if $b = 0.2$ and $\sigma_8(\Omega_{m0}/0.28)^{3/8} = 0.90_{-0.03}^{+0.01}$ if $b = 0.4$). These results are consistent with the constraints on $\sigma_8(\Omega_{m0}/0.28)^{3/8}$ from cluster number counts but were one of the first evidences for a ‘‘soft tension’’ with the constraints obtained from primary CMB data assuming a Λ CDM concordance base model.

2.2.4 PSM in a FLRW framework

The machinery of the PSM was built to reflect a Λ CDM model. Hence, it is convenient to first present the main expressions used by the algorithm in this framework (see e.g., [18]).

Regarding the cosmological density parameters, the redshift dependence on the matter and cosmological constant density parameters is respectively :

$$\Omega(z) = \begin{cases} \frac{\Omega_0(1+z)}{\Omega_0(1+z) + (1-\Omega_0)}, & \text{if } \Omega < 1; \Lambda = 0 \\ \frac{\Omega_0(1+z)^3}{\Omega_0(1+z)^3 + (1-\Omega_0)}, & \text{if } \Omega = 1 - \Omega_\Lambda \end{cases}, \quad (2.52)$$

$$\Omega_\Lambda(z) = \frac{1 - \Omega_0}{\Omega_0(1+z)^3 + (1-\Omega_0)}. \quad (2.53)$$

Here, $\Omega \equiv \Omega_m(z)$ and $\Omega_0 = \Omega_{m0}$ is the present matter density. The physical volume element per unit of solid angle and unit of redshift is:

$$\frac{dV}{d\Omega dz} = \frac{c}{H(z)} \frac{(a_0 r)^2}{(1+z)^3} = \frac{c}{H_0} \frac{d_A^2}{E(z)(1+z)}, \quad (2.54)$$

where $E(z) = H(z)/H_0$, $d\Omega = \sin\theta d\theta d\phi$ is the solid angle element of the FLRW metric and $a_0 r$ is the angular diameter distance:

$$d_A = a_0 r = a_0 \int_{r_e}^0 \frac{dr}{\sqrt{1-kr^2}} = a_0 c \int_{a(t)}^{a_0} \frac{da}{a\dot{a}} = \frac{c}{H_0} \int_{a(t)}^{a_0} \frac{da}{aE(a)}, \quad (2.55)$$

where r is the comoving distance. The luminosity distance is then related to the angular diameter one by:

$$d_L^2 = (1+z)^2 d_A(z). \quad (2.56)$$

The comoving distance d_C can be written as:

$$d_C = d_L(1+z)^2. \quad (2.57)$$

Regarding the cluster profiles, the `cluster_profile` parameter (see Section 2.3.3) in the PSM code comprises different types of profiles that can be chosen when running the code. For example, the three dimensional pressure profile is given by [36]:

$$P(r) = n(r) T(r) = T(M, z) n(r) = P_0 \left[1 + \frac{r^2}{r_c^2} \right]^{-3\beta/2}, \quad (2.58)$$

where P_0 is a model parameter, r_c is the core radius, which depends on the cluster mass, and β is fixed to 2/3. This equation can also be formulated using $n_e(r)$, the electron

density. The beta profile adjusts well to the properties of the gas, for instance the X-ray gas emission.

There are other possible profiles to be implemented like the generalized Navarro-Frenk-White (NFW) profile, commonly utilized for dark matter halos:

$$P(r) = P_{500} \frac{P_0}{(c_{500}x)^\gamma (1 + (c_{500}x)^\alpha)^{\frac{\beta-\gamma}{\alpha}}}, \quad (2.59)$$

where $x = r/R_{500}$, P_{500} an analytical formula depending on the cluster mass and redshift, and α , β and γ being fitted on XMM data [37]) and Chandra data [38], respectively.

Scaling relations depend on the baseline cosmology and also on the mass function, which in turn is model-dependent as well. These relations are key quantities in observational cosmology as they relate the cluster observables in X-rays and SZ to cluster mass. The key scaling relations are:

- Mass and temperature relations ($M - T_X$), (2.40), which are then used to construct mass functions and number counts utilised to constrain the cosmological models [17].
- $M - Y$ relation (equation 2.42), where the observed quantity is actually the Y_{SZ} , which is the total (line-of-sight) SZ signal (equation 2.46).

Outside of the scope of the standard PSM code, there are two scaling relations that could be further studied:

- Richness and Mass relation ($N - M$), (2.44), in which N is the number of galaxies which each cluster possess.
- ($N - Y$) relation Eq.[2.43].

Regarding the mass functions, the code implements the ones described in Section 2.2.

2.2.5 PSM extension to LTB models

The main task in this work was extending the PSM implementation to non-homogeneous LTB models. The PSM code has been modified according to the CGBH LTB model (see Section 2.1.3). The first stage was modifying the approach which the code computes the distance from the observer to each shell, the angular diameter distance. The procedure to compute this quantity is described in Section 3. The mass function provides us with the

number of objects per unit of volume. Therefore, the volume element has been modified. In a LTB framework it is given by [39]:

$$\frac{dV}{dz} = \frac{4\pi d_A(z)^2}{(1+z)H_L(z)} \quad (2.60)$$

The Press-Schechter mass function (2.27) is derived from the Gaussian linear perturbation theory in which the density is compared to the background's. In LTB models, the Ω_M parameter is a density function profile, that is, it will depend on the scale r instead of being a constant as in FLRW models. The impact of changing the mass functions in LTB models is direct when employing the Press-Schechter or the Seth & Thorman one because these depend on the $\sigma_8(z)$ which in turn depends on the linear growth factor $g(\Omega_m(z), \Omega_\Lambda(z))$.

In a LTB framework, the $\sigma(M, z)$ in the mass function is replaced by $\sigma_{out}(M, z) f(t, r)$ where the factor is used to rescale the variance of the density perturbations outside the void and is given by:

$$f(t, r) = \frac{\delta_\alpha(t, r)}{\delta_\alpha(t, r \rightarrow \infty)}, \quad (2.61)$$

where $\delta_\alpha(t, r)$ is the density contrast and is computed theoretically as:

$$\delta_\alpha(t, r) = \delta_0(t, r) \left(1 + \alpha \epsilon(t, r)\right), \quad (2.62)$$

where ϵ is the background shear [40]:

$$\epsilon \equiv \sqrt{\frac{2 \Sigma^2}{3 \Theta^2}} = \frac{H_T - H_L}{2 H_T + H_L}, \quad (2.63)$$

where $\Sigma^2 = \Sigma_{ij} \Sigma^{ij}$ is the square of the background shear, and Θ the expansion parameter of a congruence of comoving geodesics. α is a parameter that can depend on t and r and on the cosmological parameters. Here a value fo $\alpha=2$ as been employed [40] since this value seems to be constant through time and only slightly depend on the position in the void. In the absence of shear, that is, for large r , $\delta_\alpha(t, r) = \delta_0(t, r)$.

We can write $\delta_0(t, r)$ [40] as

$$\delta_0(t, r) \propto D(\Omega(r), A(t, r)/A_0(r)), \quad (2.64)$$

where

$$\begin{aligned}
D(\Omega, a) &\equiv \frac{5}{2} \Omega h^2 H(\Omega, a) \int_0^a \frac{da'}{[a' H(\Omega, a')]^3} \\
&= a \cdot {}_2F_1 \left[1, 2; \frac{7}{2}; \frac{\Omega - 1}{\Omega} a \right],
\end{aligned} \tag{2.65}$$

where $D(\Omega, a)$ is the growth factor in an open CDM Universe with matter parameter Ω and ${}_2F_1(a, b; c; z)$ is the Gauss hypergeometric function (GHF). This function can be expressed as an infinite series as [41]:

$${}_2F_1(a, b; c; z) = \sum_{k=0}^{\infty} \left[\frac{(a)_k (b)_k}{(c)_k} \right] \frac{z^k}{k!}, \tag{2.66}$$

in which a, b, and c are the function parameters and z is the variable of the GHF.

The PSM code computes the local slope $\alpha = \frac{d \ln \sigma^{-1}}{d \ln dM}$ as:

$$\frac{d \ln \sigma^{-1}}{d \ln dM} = \frac{d(-\ln \sigma)}{d \ln dM} = -\frac{d \ln \sigma}{d \ln dM} = -\frac{\frac{d\sigma}{\sigma}}{\frac{dM}{M}} = \frac{M}{\sigma} \frac{d\sigma}{dM} \tag{2.67}$$

So,

$$\frac{d \ln \sigma^{-1}}{d \ln dM} = -\frac{M}{\sigma} \frac{d\sigma}{dM} \tag{2.68}$$

Let us write $\sigma = f \sigma_{flrw}$,

$$\frac{d \ln \sigma^{-1}}{d \ln dM} = -\frac{M}{f \sigma_{flrw}} \frac{d(f \sigma_{flrw})}{dM} \tag{2.69}$$

where the function f depends on the scale $r(z)$. We can write:

$$\frac{d \ln \sigma^{-1}}{d \ln dM} \approx -\frac{M}{f \sigma_{flrw}} f \frac{d \sigma_{flrw}}{dM} \approx -\frac{M}{\sigma_{flrw}} \frac{d \sigma_{flrw}}{dM} = \frac{d \ln \sigma_{flrw}^{-1}}{d \ln M} \tag{2.70}$$

Therefore, the slope α is not modified by changing σ to $f \sigma_{flrw}$ as in each shell it is the same constant FLRW slope.

Concerning the gas density profiles we assume that the shape of the halos is not significantly altered in a LTB framework.

The matter of scaling relations is similar to that of the mass functions. We can make use of relations fixed by observations or theoretical ones with free parameters with dependence on the $E(z) = H(z)/H_0$ parameter, which in turn depends on the $\Omega_M(z)$ and $\Omega_k(z)$ from

the LTB parameterization.

2.3 Numerical Tools

2.3.1 Planck Sky Model

The Planck Sky Model (PSM) [42] is a set of programs and data for the simulation or the prediction of sky emission⁴. It models all of the different CMB components and also the SZ component which are addressed in further sections. The software is developed mostly in the IDL programming language and it employs the HEALPix sky-pixellisation package, the `astron` library, the `CAMB` and the `MPFIT` fitting library. HEALPix's main routines to be implemented in this project are `anafast` (calculates angular spectra) and `synfast` (generates primordial CMB maps) and `CAMB`'s tools to compute transfer function and the CMB initial power spectrum. The output of the PSM are maps and catalogues, the latter comprising the following quantities: galactic latitude, virial mass, transverse velocity, Compton parameter and core radius.

Our modeling of the full cluster population is constructed according to the following ideas:

- In the modeling of the SZ components of the PSM, the observer is placed at the origin and the Universe is sliced in concentric shells (see Figure 2.1 for a schematic visualization) of 100Mpc thick in comoving coordinates. The slicing along the depth is performed in such a way that the shells along the line-of-sight have a constant comoving distance and a redshift separation that varies with depth.
- The shells have a 100 Mpc thickness which is much larger than the size of the clusters.
- The clusters have structural properties similar to the clusters in FLRW with different matter density Ω_M which is adjusted to its predicted value in LTB framework.
- The σ_8 and Ω_b parameters vary in each shell according to the LTB framework and Ω_b is determined by observations (see Section 3.4.2).
- The Universe becomes asymptotically Einstein-de Sitter at large ($r \gg r_0$) radii.

⁴Public versions of the package are available from: www.apc.univ-paris7.fr/~delabrou/PSM/psm.html

As the shells are small comparing to the large variation of the void, we assume that different shells behave like in a FLRW model but with varying Ω_M . In this way, the PSM code populates the Universe with these dark matter halos derived from a mass function and their observational profiles. The maps is the result of this stacking, the projection of all of these slices.

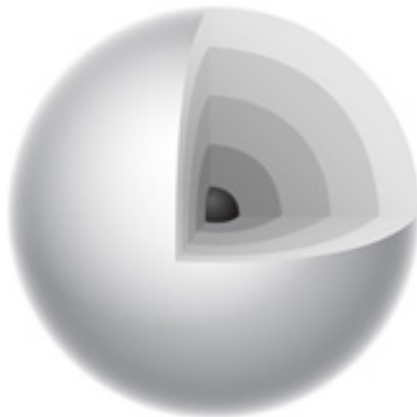


Figure 2.1: *A sphere sliced in concentric shells.*

2.3.2 Model Components

Detailed information regarding the model components can be found in [36]. The main components generated by the PSM are listed below followed by a brief description:

1. **dipole**: The CMB dipole, due mainly to the motion of the solar system.
2. **cmb**: The CMB anisotropies, including lensing, ISW, and re-ionisation effects.
3. **SZ effect**: The Sunyaev-Zel'dovich emission, including thermal and kinetic effect.
4. **galaxy**: The emission of the galactic interstellar medium, including thermal dust, spinning dust, synchrotron, free-free, and CO emission lines.
5. **point sources**: The emission of galactic and extra-galactic point sources (radio and infrared, ultracompact H-II regions).

6. **firb**: The emission of the background of blended extra-galactic infrared point sources

All these model components are astrophysical effects excepting the primordial CMB and the SZ effect. For each of these components, several different models are available, each specified with a number of model-specific parameters. Our methodology only addresses modifications to the SZ component because we are interested in exploring LTB solutions with a FLRW asymptotic behaviour at large scales (and therefore with same primordial CMB spectra as in FLRW on large scales). We outline these modifications as described below.

2.3.3 SZ component

The SZ effect in the PSM code is simulated with the superposition of thermal and kinetic effects in maps and a catalogue of galaxy clusters. The SZ model, at each shell, performs realizations that are in agreement with the abundance at each redshift for every single mass above a certain mass minimum. SZ effects are generated in the PSM by two means: i) they can be generated by post-processing (ray-tracing of) large scale N-body and/or hydrodynamical simulations of Large Scale Structure or ii) can be generated on the basis of the cluster mass function method described earlier. In both ways the code produces catalogues of clusters and maps of thermal and kinetic SZ effects. A number of parameters are implemented to convert mass and redshift into integrated Y parameter, or connect X-ray observations to Y [36]:

- **CLUSTER_PROFILE**: Allows selection of which type of profile is used to model clusters (see Section 2.3.1).
- **NSTD_PROFILE**: Whether to use a non-standard profile. A non-standard slope is a Y-M relation of $Y \propto M^{1.78}$ while a standard one is $Y \propto M^{5/3}$.
- **NORM_PROFILE**: Whether the cluster profile is normalised to match the observations. If set to no, the normalisation is made according to a theoretical model and uses the normalisation parameter **CLUSTER_T_STAR**.
- **PROFILE_BOUNDS**: Gives the distance from the cluster center at which it is assumed all the cluster mass is included. It also sets the angular distance from the cluster center at which the SZ emission of a single cluster will vanish in the SZ maps.

- **CLUSTER_T_STAR**: Normalisation parameter to be used if **NORM_PROFILE** is set to no or if **CLUSTER_PROFILE** is set to the pressure profile. It is the value of the T^* parameter of equation 4 of [43]:

$$\left[\frac{M(T, z)}{10^{15} h^{-1} M_{\odot}} \right] = \left(\frac{T}{T^*} \right)^{3/2} (\Delta_c E^2)^{-1/2} \times \left[1 - 2 \frac{\Omega_{\Lambda}(z)}{\Delta_c} \right]^{-3/2}. \quad (2.71)$$

Moreover, to generate cluster catalogues, additional parameters are set:

- **MASS_FUNCTION**: the mass function used to compute the number density of clusters in each shell and to generate maps and catalogues (see Section 2.3.1).
- **CLUSTER_M_INF**: lower mass limit of clusters included maps and the catalogue, in units of $10^{15} M_{\odot}$.
- **SZ_INPUT_CAT**: used to define the catalogues of known clusters that may be included in the simulation.
- **SZ_RELATIVISTIC**: sets whether relativistic corrections are taken into account in the model of thermal SZ, and at which order.

Lastly, there are several types of SZ models that can be implemented:

- **SZ:prediction**: includes only expected signals from the clusters included in the catalogues specified with the **SZ_INPUT_CAT** parameter. Only generates thermal SZ effect.
- **SZ:dmb**: It is the Dellabruille, Melin, Bartlet [[1]] method to compute the SZ component of the CMB sky. This is the one to be modified in this project (see Figure 2.2). It generates first a catalogue of galaxy clusters according to the mass function specified by the **MASS_FUNCTION** parameter. For each cluster, the expected SZ signal is computed on the basis of a physical model linking mass and redshift to electron density and temperature, on the basis of the spherically symmetric profile specified with the **CLUSTER_PROFILE** parameter. Cluster are distributed at random over the 4π sr of the sky, with a uniform probability. This model accepts two additional parameters: **SZ_CONSTRAINED** (whether the catalogue contains real observed clusters) and **SZ_INCLUDE_POLARISED** (whether to include polarised SZ effect).

- **SZ:hydro+dmb:** merges at low redshift ($z < 0.25$) full hydrodynamic simulation, containing the constrained local SZ map, with a high-redshift model based on cluster number counts following the method implemented in the dmb model. The catalogue only contains high redshift clusters and filaments.
- **SZ:nbody+hydro:** uses a combination of hydrodynamic N-body simulations of the distribution of baryons for redshifts $z < 0.025$ (the local Universe), and of pure N-body simulations of dark matter structures in a Hubble volume.

It is important to note that SZ relativistic effects are not taking into account in this thesis. The thermal SZ effect is the scattering of electrons that are in potential wells with a certain velocity. If the electrons are accelerated by jets coming from AGN's or black holes or if they are influenced by a distribution of non-thermal electrons, they become relativistic. Nonetheless, these effects are negligible at a cosmological scale.

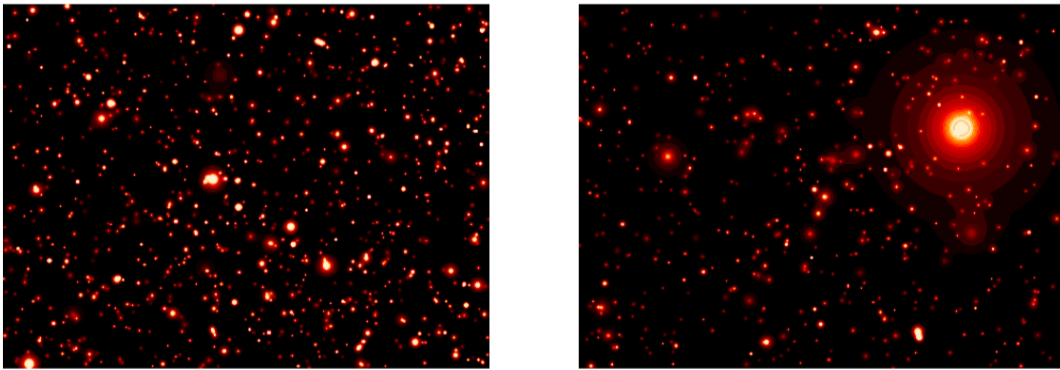


Figure 2.2: *Thermal SZ map of 3 by 4 square degrees. Left Panel: $\Omega_m = 0.3$, $\Lambda = 0.7$, $h = 0.65$, $\Omega_b = 0.05$. Right Panel: $\Omega_m = 1$, $\Lambda = 0$, $h = 0.5$, $\Omega_b = 0.07$, from [1].*

2.4 HEALPix

The analysis of functions on domains with spherical topology occupies a critical place in physics and engineering. HEALPix is a genuinely curvilinear partition of the sphere into exactly equal area quadrilaterals of varying shape [2]. Given that the original pixels in the maps do not have a square shape, it is not viable to fill a sphere with them because they will not adjust each other. One of the ways to overcome this is to perform a method

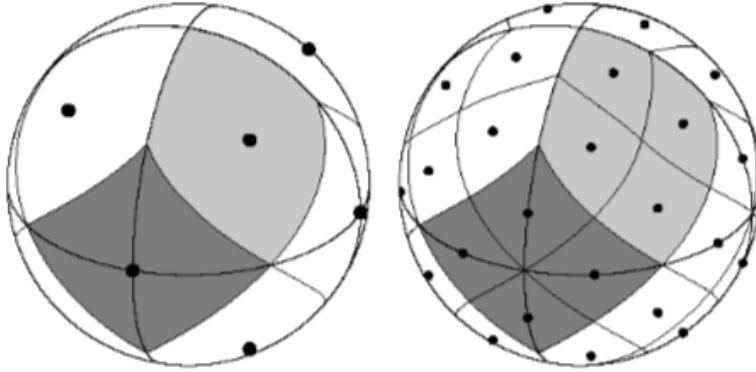


Figure 2.3: Orthographic view of HEALPix partition of the sphere. Light-gray shading shows one of the eight (four north, and four south) identical polar base-resolution pixels. Dark-gray shading shows one of the four identical equatorial base-resolution pixels. The grid is hierarchically subdivided with the grid resolution parameter equal to (left, right): $N_{side} = 1, 2$ and the total number of pixels equal to $N = 12 \times N_{side}^2 = 12, 48$. From [2]

of tessellation of the sky, performed by HEALPix. A tessellation is a method to split a domain, e.g. a surface, such that its area is totally divided in continuous portions, covering the entire surface. This method is not about the pixels' shapes but with their area size. Tessellation on a flat surface is comparatively simple to perform, however in a sphere, due to its curvature, the process becomes more challenging.

All pixels have the same area size since they reach our terrestrial detectors with equal areas. The base-resolution comprises 12 pixels in 3 rings around the poles and equator. The resolution of the grid is expressed by the parameter N_{side} which defines the number of divisions along the side of a base-resolution pixel that is needed to reach a desired high-resolution partition. In other words, it controls the number of pixels in a map and in turn, the way that the tessellation is performed in the sphere, since the number of pixels increases with the increase of N_{side} . In turn, what sets the resolution of the observation is the width of the Gaussian beam, specified by the parameter $sky_{resolution}$. All pixel centers are placed on $4 \times N_{side} - 1$ rings of constant latitude, and are equidistant in azimuth (on each ring).

The two main HEALPix's facilities for this thesis are `anafast` and `synfast` [44]. `anafast` performs harmonic analysis up to a specified maximum spherical harmonic order ℓ_{max} , reading one or two binary FITS files containing a HEALPix temperature or both temperature and polarisation (Q,U) maps and makes an output file containing the angular temperature fluctuation or cross power spectra. Concerning the Stoke's

parameters, four power spectra are needed to characterize fluctuations in a gaussian theory. These are the autocorrelation of T, E and B polarization modes and the cross correlations of E polarization and T temperature. The Stokes parameters are expanded in spin-weighted harmonics $\pm 2Y_l^m$ where the $\pm 2a_{lm}$ coefficients are observable on the sky and their power spectra can be computed for different cosmological models [44]. **anafast** is optimized to calculate the power spectrum of all Stokes' parameters. **synfast** can read the power spectra from a file, e.g. generated by **anafast** function, and then generates Q and U maps, temperature maps and its derivatives. The code can also be applied to generate a set of a_{lm} matching the input power spectra, beam size and pixel size. Those a_{lm} can be used as an input to another **synfast** run. **synfast** needs a random seed which creates a sequence of random numbers that are used in the generation of the random realization of the primary CMB signal.

2.5 CAMB

CAMB is a Boltzman code for calculating CMB, angular power spectrum, matter power spectrum and transfer functions. The PSM code needs the matter power spectra at decoupling, 380 000 years after the big bang. To compute the CMB it is crucial to calculate the linear perturbation component because it is emitted in an epoch where the perturbations are very small and it depends on the integrals of the power spectrum, calculated by a Boltzman code. In this thesis, CAMB is implemented mainly to generate the transfer function and initial matter power spectra necessary to compute the input spectrum of the primary CMB fluctuations (Temperature-Temperature, Temperature-Polarization and Polarization-Polarization modes, respectively, TT, TP and PP modes). This is then used by the **synfast** function of **Healpix** to generate maps for the primordial CMB component of the PSM code. The PSM code uses the fortran part of CAMB and giving arguments to **synfast**, it generates a file where it puts the sky map data with regard to the set of cosmological parameters used. The transfer function is necessary to calculate the CMB maps, and it is then that **synfast** calls CAMB. The SZ component does not need **synfast**. Instead, it makes use of **anafast** to calculate Cl's of the SZ maps.

Using the CAMB and **synfast**, the PSM code generates a map of temperature fluctuations and map of galaxy clusters for that specific set of cosmological parameters.

Chapter 3

Methodology

3.1 Overview

The starting point of this work is the installation of the PSM code and of the features required, understanding how they operate and running them to get familiar with their functioning. Besides, studying the applications of the SZ effect and exploring the machinery of the LTB models is also indispensable. The main work is identifying the functions of the PSM code to be modified and changing them according to a LTB framework. In a first stage, we identified what we named the zero order functions, that is, the ones related to the background properties of the Universe. These include the angular diameter distance, the Hubble rate, the volume element and others. The second stage is then modifying the mass function which is then related with the perturbations. Finally, we compare the obtained results with a standard FLRW framework. As described previously, our LTB Universe is sliced in shells of 100 Mpc. In each shell a Poisson deviate is performed with mean value equal to the mass function. The angular coordinates are distributed evenly along the shell. This is performed to obtain an uniform distribution over the shell, as the angular coordinates of the clusters are evenly distributed. There is also a radial distribution of clusters with redshift. The PSM code attributes the same redshift to clusters belonging to the same shell. Having the maps, we are able to perform a fast statistical analysis, specially with all-sky flat maps, obtaining the histogram of the distribution of pixels and its key moments, one of them being the mean SZ signal $\overline{y_{SZ}}$ (Eq. [2.45]). The PSM generates clusters of galaxies all over the sky, and for small angular areas (for instance, a $10^\circ \times 10^\circ$ patch) where there is a great deal of matter, the sky is still large enough to be flat. Having an all-sky map,

calculating the power spectra is a straightforward procedure employing a HealPix’s package described in Section 2.3. Finally, as this code also generates catalogues of galaxy clusters, we present histograms of the abundance of objects $N(z)$ through a redshift span for the fiducial CGBH model and some variations of the parameters. The abundance of objects $N(z)$ is a crucial quantity to make constraints with galaxy clusters in LTB and to compute the covariance function.

3.2 DMB method

Regarding the generation of maps and catalogues, our focus is on the DMB method [1] (Section 2.3.3), implemented by the PSM, which has been altered to a LTB framework. It generates dark matter halos maps and implements a NFW profile, (2.59), and has the advantage of allowing to perform many map realizations for any set of cosmological parameters. However, this method does not take into account cosmological correlations between clusters (e.g. filaments, as it lacks the modeling of cluster correlations). In other words, it is not sensitive to the clustering component of the power spectra (2.51).

3.3 Model Parameters

As mentioned previously, Garcia-Bellido and Haugbølle proposed a model with six parameters which is totally described by $\Omega_M(r)$ and $H_0(r)$ [12]. They also established a more constrained model that imposes a simultaneous Big Bang time, the constrained GBH model (CGBH) [12]. We decided to set the CGBH model as our reference model but the implementation performed in this thesis is unique as all the non-FLRW information enters the code through tables. Therefore, this modified DMB model can be directly applied to other models like the ALTB model. This CGBH model is characterized by a local void size of a few Gpc and asymptotically Einstein-de Sitter, Ω_{out} is fixed to $\Omega_{out}=1$ and H_{in} and H_{out} are replaced by H_0 of (2.23) which is related to H_T as (2.18) shows. Therefore, only four parameters remain: r_0 , Δr , Ω_{in} and h . A fiducial CGBH model was chosen around which the parameters vary. In this work this model is set to have $r_0=1.5$ Gpc, $\Delta r=0.5$ Gpc, $\Omega_{in}=0.3$ and $h = 0.7 \text{ } 100 \text{ km s}^{-1} \text{ Mpc}^{-1}$. Here, maps are computed only up to $r_0=2.5$ Gpc as the number of galaxy clusters with masses larger than $10^{14} M_\odot$ decays promptly from that scale since there are few clusters above this redshift. The range of values for these four parameters is presented in Table 3.1. To study the evolution

of the power spectra and thermal SZ maps as the parameters vary, three parameters are fixed to their fiducial values while the remaining one varies according to the values in Table 3.1. For instance, when varying the Δr parameter through its different values, the remaining parameters are fixed to $\Omega_M(r)=0.3$, $h=0.7$ and $r_0=1.5$ (their fiducial values).

	Model Parameters				
Δr (Gpc)		0.250	0.5	0.750	
Ω_{in}	0.1	0.2	0.3	0.4	0.5
r_0 (Gpc)	0.750	1	1.5	2	2.5
h (100kms ⁻¹ Mpc ⁻¹)	0.625	0.65	0.675	0.7	0.75

Table 3.1: Range of values for the several parameters. The parameters regarding the fiducial model are in bold.

3.4 The code

As mentioned before, the first stage of the project concerns the modification of the average properties through the void’s profile. For each shell it is assumed that everything behaves as if the Universe was described by a FLRW metric but with the Ω_M parameter varying as in LTB framework. The second stage then relates to the evolution of the perturbations and here the modifications concern the mass function, the linear growth factor and the variance of the fluctuations. Several numerical tools are needed to perform the desired outputs: The Bubble code, the PSM code, CAMB and HEALPix. These are described in the next subsections.

3.4.1 Bubble code

The Bubble code is a publicly available software developed by Philip Bull (Queen Mary, London) which outputs the relativistic exact solutions in LTB framework ¹. It contains a set of functions that, given a baseline model, compute key quantities such as the Hubble rates, the angular diameter distance and the redshift and they are computed along the

¹<https://gitlab.com/cosmobubble/bubble>

geodesic. It makes use of the `gsl` library and it allows for both LCDM and LTB models to be computed. Concerning the LTB framework, this code is prepared to work with the CGBH model from [45] which is indeed the model studied in this work. In the `main.cpp` Bubble file the user can specify which kind of model they wish to work with alongside with its model parameter values. Besides, the quantities that the user wishes to output are also chosen there. Then, the output is generated and files with tables of the different quantities are produced and called in a structure of parameters named `define_cosmo.pro`. From now on, we will name this structure "cosmo" structure. Having these key quantities in the cosmo structure it is then straightforward to create functions and procedures that make use of these quantities. When building and modifying the LTB functions, the tables are imported by calling the cosmo structure and linear interpolating to a redshift array specified by the user by employing the `interp()` IDL function.

3.4.2 Zero order modifications

The first modified file was the configuration file named `config.psm` where it is specified the control parameters of the PSM run and where it is chosen what type of model and components the user wishes to employ. We turned off the code components regarding the CMB primary signal and all the CMB foreground components except the SZ effect. It is here that is also specified the pixelisation parameters for the sky model concerning HEALPix's routines.

The first modified function is the `define_cosmo.pro`. This function creates a structure, usually called `cosmo`, containing the cosmological parameters and arrays of values (tables) coming from the Bubble code from its different outputs. The Ω_{out} parameter is specified here as $\Omega_{out}=1$ as the simulated Universe is here assumed to be asymptotically a critical FLRW Universe outside the void. Other important parameters are specified in this file, for instance the amplitude of density fluctuations $\sigma_8(0)$, the scalar spectral index n_s , the reionisation optical depth τ , the helium fraction and others. Consequently, the tags of the new LTB parameters and array of values were added to the `read_sky_param.pro` function. In the majority of the modified functions described below a linear interpolation had to be employed on the LTB tables generated by Bubble as the redshift array from the "cosmo" structure is fixed and the user may wish to employ a specific redshift array when working with the several quantities (since they are redshift-dependent). Then, the

function that calculates the angular diameter distance, named `ang_dist.pro`, was modified. It computes the angular distance of a source in Mpc by receiving a redshift array and the "cosmo" structure containing the cosmological parameters in memory. This procedure is straightforward since the Bubble code already outputs the d_L quantity and the angular diameter distance is then calculated using the luminosity-distance relationship (Eq. (2.56)).

We also changed the Hubble function by creating a new one named `hubble_at_z_ltb.pro` which receives the same inputs as the angular diameter one. Here, the Hubble transverse rate H_T quantity is used to represent the Hubble rate as it is the one used to define the density parameters as presented in Eqs. (2.9) and (2.10). Then, the function `com_dist.pro` which computes the comoving distance of a source in Mpc was modified to be calculated as in Eq. (2.57). We then created a function named `omega_m_z_ltb.pro` that computes the time-dependent $\Omega_M(r(z))$ density profile in a LTB framework. This function receives the Ω_M array calculated by Bubble and interpolates it with respect to a user-specified redshift array. The function that computes the volume element, `covolume.pro` was modified to be calculated as (2.60). Here, we employ `ang_dist.pro` and the radial transverse Hubble rate H_R .

Some procedures and functions suffered indirect modifications. For example, the function `cluster_model.pro` employed the previous FLRW `hubble_at_z.pro` function and therefore it was replaced by the new LTB one. This `cluster_model.pro` function computes the temperatures, the central densities, the core radii, the scale radii, the central optical depth or the central Compton parameter from redshift and mass arrays. The function `fast_int_y.pro` was changed the same way and it computes the integrated Y parameter of the clusters of masses M and redshift z. The same method was applied to `convert_mass_radius.pro`, `fof2delta.pro` and `fast_convert_mass_radius.pro` functions. The first converts masses and radii from an overdensity to another given a NFW profile, the second converts the Friend-Of-Friend parameter b into an overdensity given a NFW profile and the third is a fast version of the first one. Regarding the `cluster_catalog.pro` function, other changes were applied. The `covolume` function was replaced for the LTB one and the computation of the present density ρ_0 was modified replacing the FLRW Ω_M parameter for the distance-dependent `omega_m_z_ltb.pro` LTB function providing $\Omega_M(r(z))$. In the second stage of modifications regarding the calculation of the mass function, in `cluster_catalog.pro` the factor (2.61) was included

in order to modify the computation of $\sigma(M, z)$ as described in Section 2.2.5. `cluster_catalog.pro` creates a catalog of clusters using a mass function by placing clusters with a certain mass range at each redshift bin. The `mf_density.pro` function was modified the same way as the `cluster_catalog.pro`. This `mf_density.pro` function computes the cluster density given by a mass function for 1 deg^2 .

Clusters of galaxies not only contain dark but also baryonic matter and they can be considered to be large enough to reflect the background cosmological baryon fraction. The baryon fraction in clusters is then expected to be given by the ratio between the baryonic and total matter density parameters, $f_b = \Omega_b/\Omega_m$. Observations support this idea, but it is usually difficult to measure f_b out to sufficiently large radii in clusters. Recent studies, see e.g. [46, 47], providing observed baryon fractions up to the R_{500} overdensity radius in clusters, show that $f_b(R_{500})$ is consistent with the cosmological ratio Ω_b/Ω_m provided by Planck observations. Detailed observations of the Coma cluster, out to the virial radius, also reached the same conclusion, i.e. $f_b = \Omega_b/\Omega_m = 0.158$, [48]. In the PSM code, the baryon fraction is an input parameter that is held fixed for all clusters. In our LTB version of the code, we also make this assumption, i.e. all clusters have the same f_b , regardless of their distance to the LTB void center. We therefore set $f_b = 0.158$ in the `define_cluster.pro` function, as obtained from observations in [48, 46]. By default, the PSM code assumes that the cluster gas mass that originates SZ signal is $M_{gas} = 0.9 f_b M$, where M is the total cluster mass. We kept this setting.

3.4.3 First order modifications

The first order modifications span the changes regarding the computation of the mass function which is then related to the σ_8 parameter and to the linear growth factor. There is only one additional function that was modified when comparing to the first order modifications which is the `cluster_catalog.pro`. As mentioned in Section 2.2.5 and Eq. (2.61), the factor $f_{ltb}=f(t,r)$ was included in the calculation of $\sigma(M, z)$. This procedure calls the function `tinker.pro` which is the multiplicity function $f(\sigma)$ of the mass function as presented in (2.26). To include this f_{ltb} factor several functions were created. First, it is necessary to compute the hypergeometric function ${}_2F_1(a, b; c; z)$ described in equation 2.66. For this, a python code was used and the outputed values were saved in a text file with two columns, one with values ranging from -1 to 1 and the other with the outputed values from the hypergeometric function itself. Then, a function

named `geometrica.pro` was created. This function reads the same file containing the two columns and interpolates the values of a_1 and z coming from Bubble with respect to the user-specified redshift array to output $2F_1(a, b; c; z)$ from (2.66) with the correct values. Then, to compute f_{ltb} two different functions were created, one for the numerator and other for the denominator. These two functions are the linear growth factor in equation (2.65). The only difference between them is the computation of the value of a which differ according to the baseline model. For the FLRW baseline, it is simply given by $a = \frac{1}{1+z}$ while for LTB models it is the a_1 quantity in (2.1). These functions are named `growth_factor_ltb.pro` and `growth_factor_lcdm.pro` respectively. These functions call `geometrica.pro` to compute the $2F_1$ function for the LTB and LCDM case, respectively. To compute `growth_factor_ltb.pro`, or, in other words, the numerator of (2.61), a `shear.pro` function was created to compute (2.63) and α is assumed to have the constant value of $\alpha=2$, [49]. The f_{ltb} factor (2.61) is then computed in the `f_ltb.pro` function by simply calculating the ratio of the two functions described above.

3.4.4 Anafast

As mentioned in the previous chapter, `anafast` is a HEALPix routine that performs harmonic analysis to a specified maximum spherical harmonic order ℓ_{max} , reading binary FITS files containing a HEALPix temperature or both temperature and polarisation (Q,U) maps and outputs a file containing the angular power spectrum, C_l^{TT} , or cross and polarisation power spectra [2]. After running the Bubble and PSM code several files are stored. The one that is used by `anafast` is named `thermalsz_map.fits` which is a temperature only map generated by the PSM with $N_{side}=256$. The output is a thermal SZ power spectrum file named `cl_out.fits`.

3.5 Statistics

After getting the thermal SZ maps and running `anafast` to get the angular power spectra, the IDL function `plthist()` is employed to create histograms of the distribution of pixels in the maps generated for this thesis. To estimate the bandwidth h of the bins of the

histograms we employed the Silverman’s rule of thumb:

$$h = \left(\frac{4\hat{\sigma}^5}{3n} \right)^{\frac{1}{5}} \quad (3.1)$$

This is the bandwidth that minimises the mean integrated squared error [50]. Then, the IDL function `moment()` calculates the moments of a vector. These include the mean:

$$\bar{x} = \frac{1}{N} \sum_{j=0}^{N-1} x_j, \quad (3.2)$$

the variance:

$$\sigma^2 = \frac{1}{N-1} \sum_{j=0}^{N-1} (x_j - \bar{x})^2, \quad (3.3)$$

and also the skewness:

$$\text{skewness} = \frac{1}{N} \sum_{j=0}^{N-1} \left(\frac{x_j - \bar{x}}{\sqrt{\sigma^2}} \right)^3, \quad (3.4)$$

and finally the kurtosis:

$$\text{kurtosis} = \frac{1}{N} \sum_{j=0}^{N-1} \left(\frac{x_j - \bar{x}}{\sqrt{\sigma^2}} \right)^4 - 3. \quad (3.5)$$

For this project only the mean value and the variance. These mean value is translated as the mean SZ signal $\overline{y_{SZ}}$ or the mean Compton parameter value.

3.6 Testing LTB results

All functions that we have modified and described above were tested individually and compared against known literature papers ([12] and [13]). More precisely, we compared the plots concerning the dependence of the matter density profile, the angular diameter distance, the Hubble rates and the volume element with several parameters (Section 4.1). In the mass function modification, we also tested the hypergeometric function by comparing the output function with python and *Wolfram Mathematica* results.

First, we implemented the function outside the PSM code and compared them with published results. Then, we implemented these functions in the PSM itself and we checked

if the output of the functions were the same as when the functions were outside the code. Finally, while running the FLRW version of the PSM code, we compared the results with the FLRW results from the non-modified version of the code to check if the results corresponded.

To test the liability of the Bubble code when integrated in the PSM code, we compared the obtained results with the FLRW results coming from the PSM code without the Bubble implementation.

Finally, we compared the results with the standard FLRW framework. For this, two runs of the PSM code were assembled by setting $\Omega_M = 0.3$ and $\Omega_M = 1$. In both runs the Hubble parameter was set to $h = 0.67 \text{ 100kms}^{-1}\text{Mpc}^{-1}$ and the remaining parameters match the ones in the LTB framework stated in the `define_cosmo.pro` function

Chapter 4

Results

The main goal of this project is to study the dependence of the power spectrum and of the y_{SZ} signal as the model parameters vary. This section presents some of the results regarding the zero and first order modifications as well as the comparison between LTB and FLRW results. Primarily, we present the evolution of key quantities such as the angular diameter distance and the volume element. The angular diameter distance, Eq. (2.15), is related to the SZ signal as is shown in Eq. (2.46), whereas the angular power spectra C_l is proportional to the volume element, Eq. (2.60), and the mass function, Eq. (2.26), as Eq. (2.50) shows. Then, we present the evolution of the density function profile Ω_M in LTB framework when varying the parameters as stated in Table 3.1. Then, we split the results in two stages: zero order modifications and first order modifications, as explained in Chapter 3. In each stage, an all-sky thermal SZ maps as well as a plot of the respective power spectra are shown. Since the generated maps are represented by a vector of pixels and each pixel has a SZ thermal distortion y_{SZ} , a histogram of the distribution of pixels and its respective key statistics, for instance the mean value of y_{SZ} and the variance σ^2 are also displayed. Finally, histograms of the abundance of objects per redshift concerning the generated catalogues are presented in the last section. In the main text it is only presented some of the results and the remaining can be consulted in the appendices at the end of the work.

4.1 Dependence of the LTB density profile on the CGBH parameters

We start by looking at the dependence of the density profile $\Omega_M(r)$, given by Eq. 2.20, for the adopted model as the several parameters vary. When plotting Ω_M with respect to a certain parameter, the remaining ones are set to their fiducial value (see Table 4.1).

For instance, in Figure 4.1 is shown a plot of the evolution shape of Ω_M as the r_0 parameter varies:

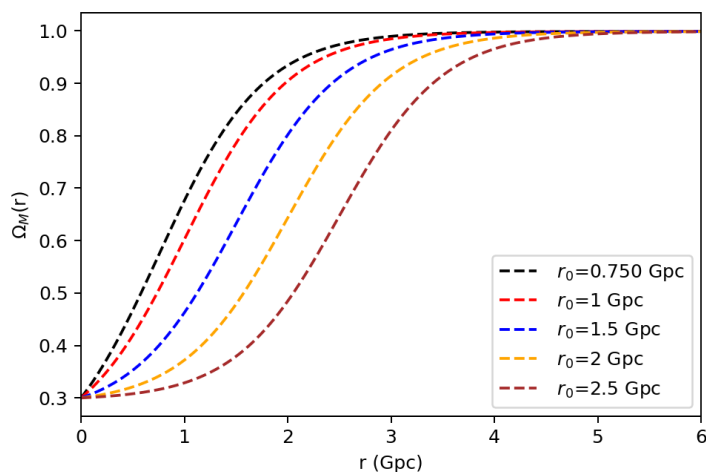


Figure 4.1: Change in the density function profile $\Omega_M(r)$ when varying the CGBH model parameter r_0 . The fiducial model is represented by the blue line ($r_0=1.5$ Gpc).

Naturally, all plots start at $\Omega_{in}=0.3$ at $r=0$ since it is the fiducial value for that parameter.

In Figure 4.2 it is shown the change of $\Omega_M(r)$ when varying the Δr parameter:

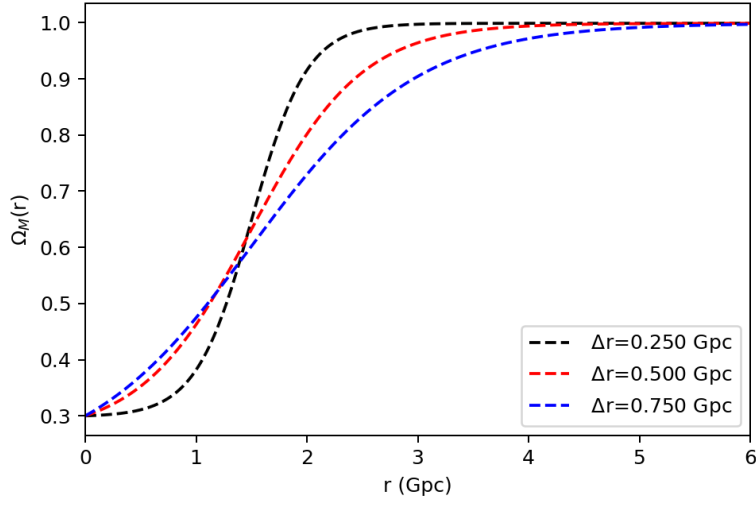


Figure 4.2: Change in the density function profile $\Omega_M(r)$ when varying Δr . The fiducial model is represented by the red line ($\Delta r=0.5$ Gpc).

It can be observed that the density function profile Ω_M varies more smoothly for higher values of Δr , as this parameter represents the transition to uniformity. In Figure 4.3 the variation of $\Omega_M(r)$ is represented for several values of Ω_{in} :

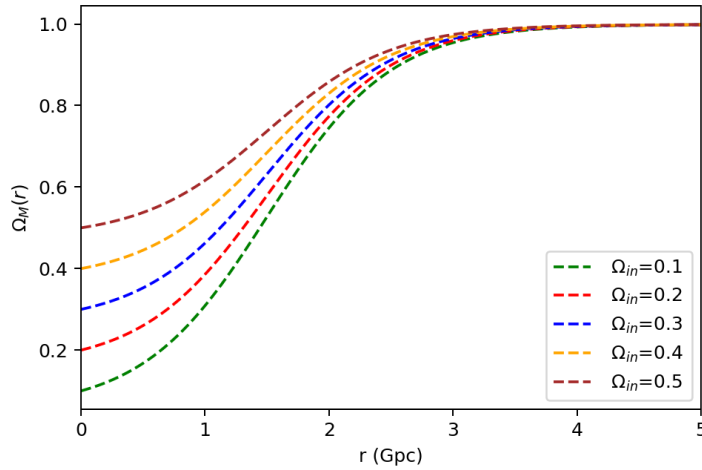


Figure 4.3: Change in the density function profile $\Omega_M(r)$ when varying Ω_{in} . The fiducial model is represented by the blue line ($\Omega_{in}=0.3$ Gpc).

Naturally, the variation of Ω_M is represented for several values of Ω_{in} . For instance, a model in which $\Omega_{in}=0.3$ will have $\Omega_M=0.3$ at $r = 0$. This is understandable since Ω_{in} quantifies the density function inside the void.

In Figure 4.4 the change of $\Omega_M(r)$ is plotted for different values of h :

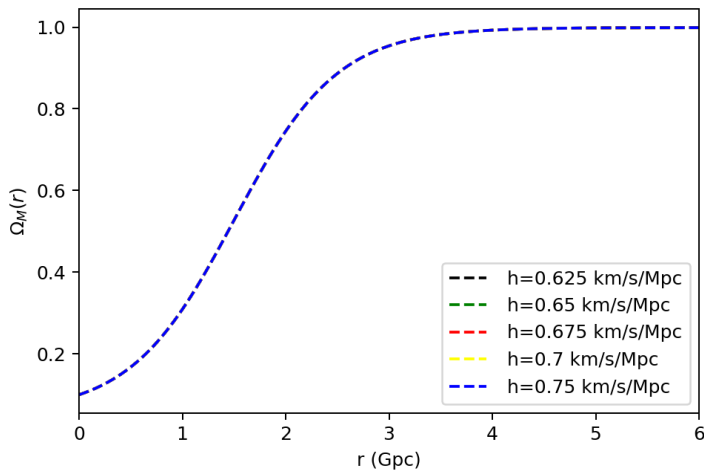


Figure 4.4: Change in the density function profile $\Omega_M(r, t_0)$ when varying h .

As expected from Eq. (2.20), the density function does not depend on h .

4.2 Dependence of r , d_A , dV/dz , H_T and H_R on the CGBH parameters

Here we study how quantities such as d_A , dV/dz , H_T and H_R depend on the CGBH parameters. This will help us to understand the dependence of the thermal SZ signal and power spectrum as a function of the CGBH parameters that will be discussed in Section 5. Some plots represent the dependence for the current age of the universe $t = t_0$ whereas others display key quantities with z , i.e., along the light-cone (geodesic). As the thermal SZ signal depends on the angular diameter distance, see Eqs. (2.45) and (2.46), and the volume element is a key quantity when computing the Poisson term of the angular power spectra, Eq. (2.50), it is important to show the evolution of these quantities with the model parameters. Figure 4.5 represents the evolution of the scale r with redshift:

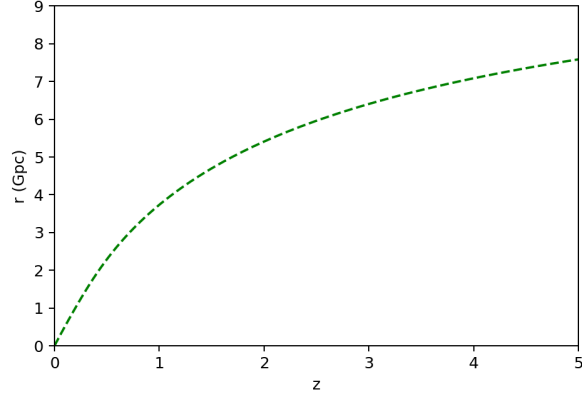


Figure 4.5: Evolution of the scale r with the redshift regarding the fiducial CGBH model.

This plot is useful when we wish to translate scale r into redshift.

Figure 4.6 shows the evolution of the H_T and H_R hubble rates with the scale r at the current time (left panel) and with redshift (right panel). Both plots assume the CGBH fiducial model whose parameter values are listed in Table 3.1.

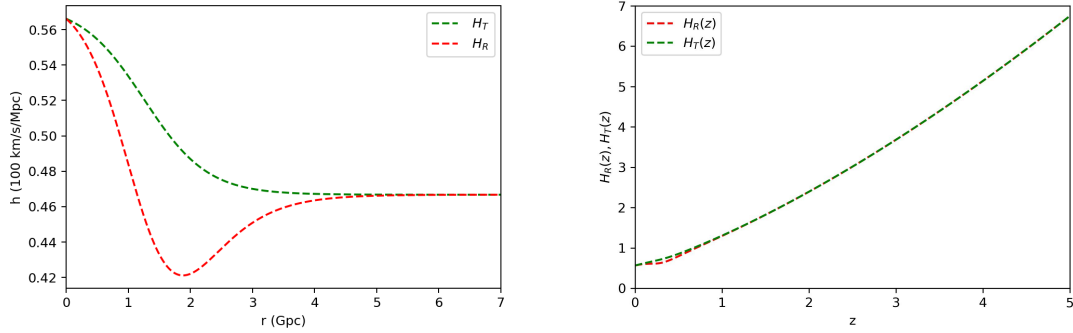


Figure 4.6: Left panel: Evolution of H_T and H_R with the scale r taken at the current time for the central observer assuming a fiducial CGBH model. Right panel: Evolution of H_T and H_R with redshift assuming the fiducial CGBH model.

Angular diameter distance

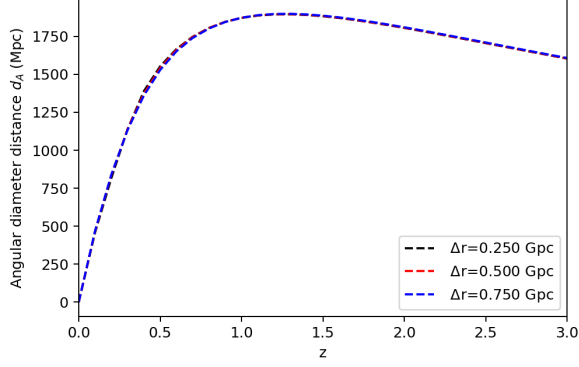


Figure 4.7: Angular diameter distance for different values of Δr . The fiducial model is the red line ($\Delta r = 0.5$ Gpc).

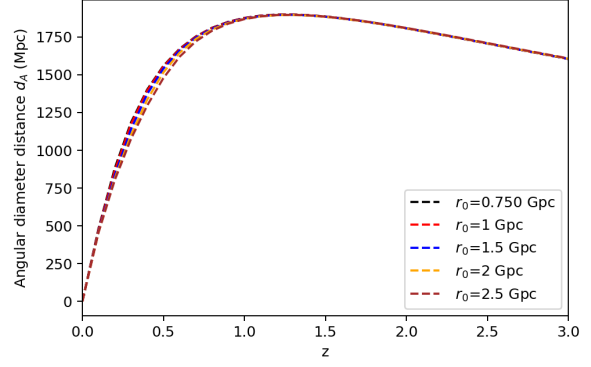


Figure 4.8: Angular diameter distance for different values of r_0 . The fiducial model is the blue line ($r_0 = 1.5$ Gpc).

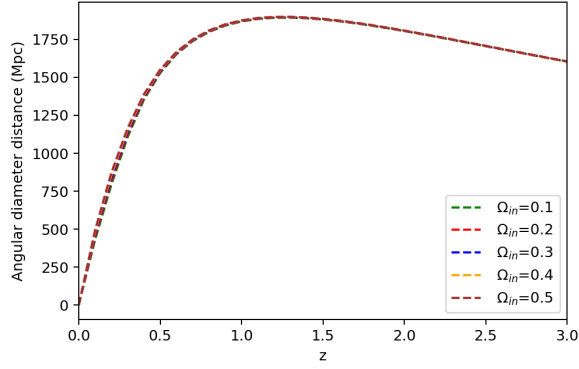


Figure 4.9: Angular diameter distance for different values of Ω_{in} . The fiducial model is the blue line ($\Omega_{in} = 0.3$).

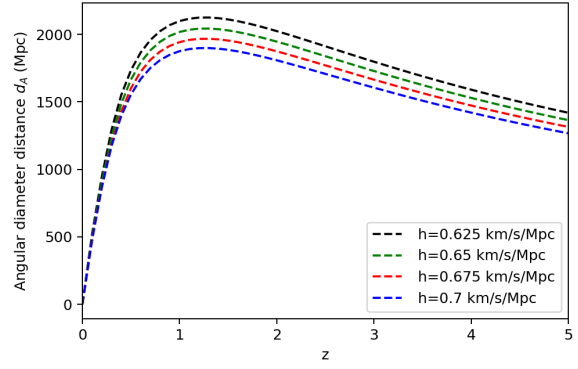


Figure 4.10: Angular diameter distance for different values of h . The fiducial model is the red line ($h = 0.675$ km/s/Mpc).

From the plots it is clear that the angular diameter distance is scarcely sensitive to Δr and Ω_{in} as Figs. 4.7 and 4.9 show. A small variation of this quantity can be noticed when varying r_0 (Fig 4.8) although it presents a significant dependence on h as Fig. 4.10 displays.

Volume element

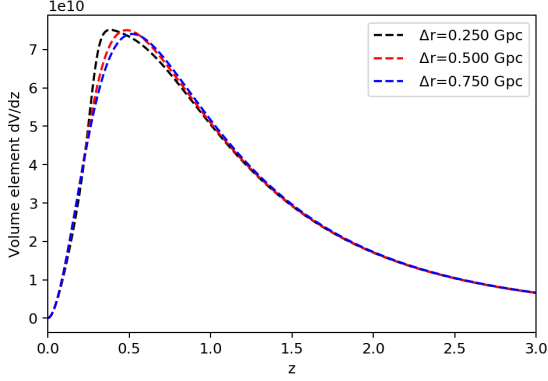


Figure 4.11: Volume element for different values of Δr . The fiducial model is the red line ($\Delta r = 0.5$ Gpc).

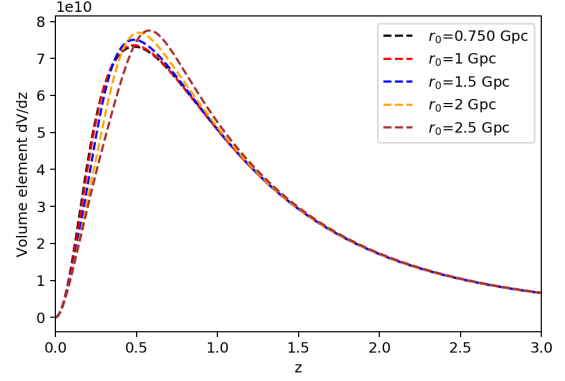


Figure 4.12: Volume element for different values of r_0 . The fiducial model is the blue line ($r_0 = 1.5$ Gpc).

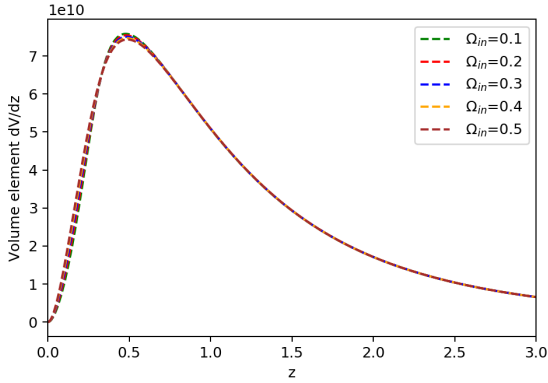


Figure 4.13: Volume element for different values of Ω_{in} . The fiducial model is the blue line ($\Omega_{in} = 0.3$).

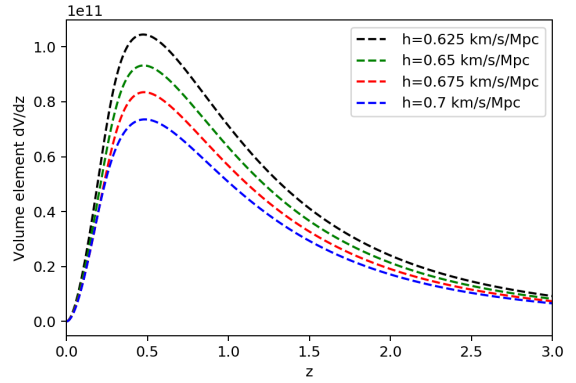


Figure 4.14: Volume element for different values of h . The fiducial model is the red line ($h = 0.675$ km/s/Mpc).

From the obtained plots it is clear that the volume element is barely sensitive to Ω_{in} (Fig 4.13) and it varies the most with h . All curves in all of the plots are identical below $z \approx 0.25$.

4.3 Zero Order Modifications

4.3.1 Thermal SZ maps

First, the thermal SZ map for the fiducial CGBH model and a five degree patch is displayed in Figure 4.15. Then, thermal SZ maps for two different values of Ω_{in} are displayed for comparison in figures 4.16 and 4.17.

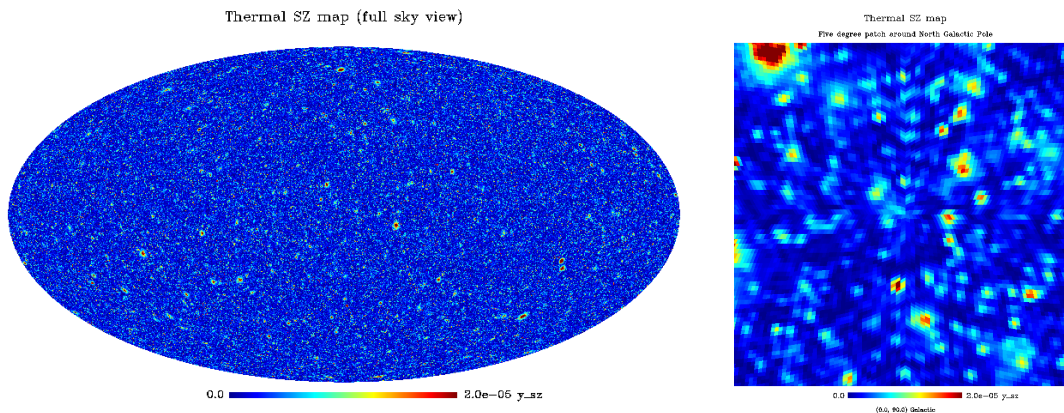


Figure 4.15: Mollview projection of the thermal SZ map regarding the fiducial CGBH model.

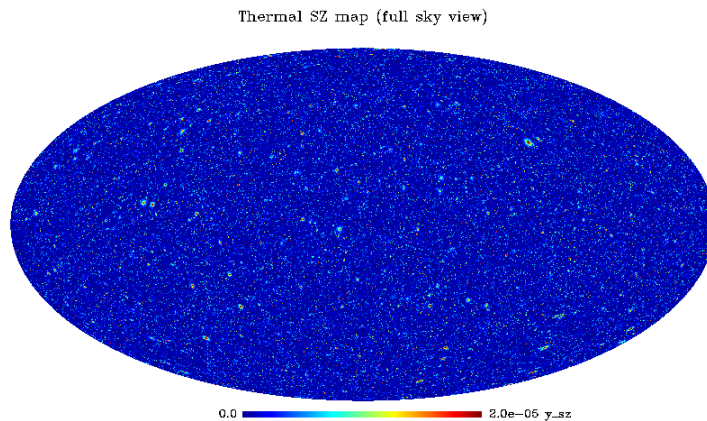


Figure 4.16: Mollview projection for a CGBH model with $\Omega_{in} = 0.1$ (the remaining parameters are set to their fiducial value).

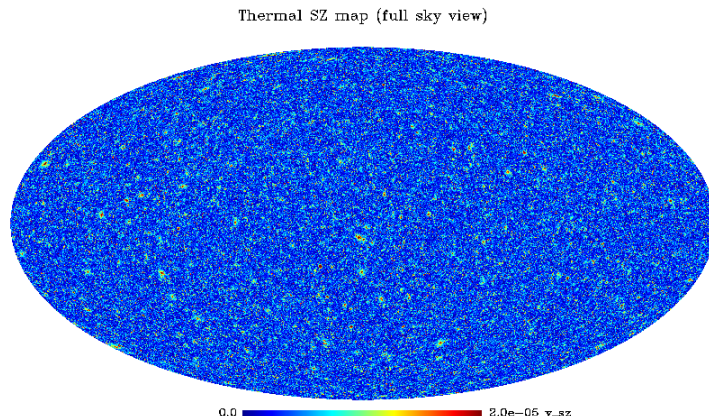


Figure 4.17: Mollview projection for a CGBH model with $\Omega_{in} = 0.5$ (the remaining parameters are set to their fiducial value).

4.3.2 Map statistics

The following step is computing the respective mean value of the SZ signal $\overline{y_{SZ}}$ and its variance in the maps. These are presented in Table 4.1. We note that our maps do not contain the SZ signal contribution from gas in filaments and in low density regions (gas outside clusters), see [16], for a discussion on how the thermal SZ effect originates from different temperature and density regions (the phase space) in hydrodynamic N-body simulations in FLRW models. As a consequence we expect that our $\overline{y_{SZ}}$ signal will be smaller than that could be obtained from hydrodynamic N-body simulations in LTB.

Fiducial CGBH model	
	$\Omega_{in} = 0.3, r_0 = 1.5, \Delta r = 0.5, h = 0.7$
$\overline{y_{SZ}}$	2.876E-06
σ^2	1.006E-11

Table 4.1: Mean y -distortion and variance of the thermal SZ signal in maps obtained using the zero-order modification for the fiducial CGBH model.

Dependence with Δr (Gpc)		
	0.250	0.750
$\overline{y_{SZ}}$	2.544E-06	2.951E-06
σ^2	8.882E-12	1.023E-11

Table 4.2: *SZ mean y -distortion and variance in maps obtained using the zero-order modification when varying Δr .*

Dependence with h				
	0.625	0.65	0.675	0.75
$\overline{y_{SZ}}$	3.107E-06	2.988E-06	2.927E-06	2.724E-06
σ^2	8.698E-12	8.809E-12	9.333E-12	1.063E-11

Table 4.3: *SZ mean y -distortion and variance in maps obtained using the zero-order modification when varying h .*

Dependence with Ω_{in}				
	0.1	0.2	0.4	0.5
$\overline{y_{SZ}}$	1.397E-06	2.155E-06	3.548E-06	4.215E-06
σ^2	6.461E-12	8.440E-12	1.100E-11	1.218E-11

Table 4.4: *SZ mean y -distortion and variance in maps obtained using the zero-order modification when varying Ω_{in} .*

Dependence with r_0 (Gpc)				
	0.750	1	2	2.5
$\overline{y_{SZ}}$	3.827E-06	2.837E-06	2.543E-06	2.361E-06
σ^2	1.365E-11	9.636E-12	8.840E-12	7.420E-12

Table 4.5: *SZ mean y -distortion and variance in maps obtained using the zero-order modification when varying, r_0 .*

4.3.3 Power Spectrum

Figure 4.18 shows the thermal SZ angular power spectra in maps obtained with the zero-order modification method, as a function of the CGBH Ω_{in} parameter. The variation of the SZ angular power spectrum with the other CGBH model parameters can be found in the Appendix "Zero order modification" (Figs. .13, .14 and .15) along with a corresponding set of all-sky map realizations (Figs .1-.11).

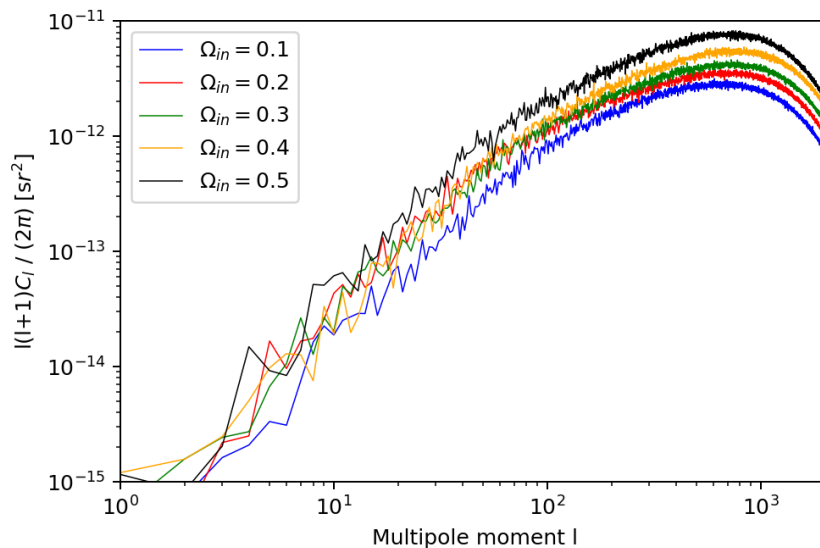


Figure 4.18: Angular power spectrum of the CGBH model obtained using the zero order modification method, for the different values of Ω_{in} . The fiducial model is represented by the green line.

Our findings under the zero order modification method will be used to interpret the results of your final stage of modifications that we will present next. In Section 5 we will present the discussion of our main results.

4.4 First Order Modifications

The first order modification method, that includes all zero order modifications plus modifications of the mass function, linear growth factor and variance of density fluctuations in a CGBH framework, are our best predictions for the thermal SZ effect arising from the galaxy cluster population generated by our approach. In the coming

sections we will present results that will be discussed in detail in Section 5.

4.4.1 Thermal SZ maps

First, the thermal SZ map for the fiducial CGBH model (obtained with the first order modification method) is displayed in Figure 4.19. A five degree patch is shown in Figure 4.20. Then, in Figures 4.21 and 4.22 the thermal SZ maps for $r_0=0.750$ Gpc and $r_0 = 2.5$ Gpc as well as the thermal SZ maps for $\Delta r = 0.250$ Gpc and $\Delta r=0.750$ Gpc in Figures 4.23 and 4.24.

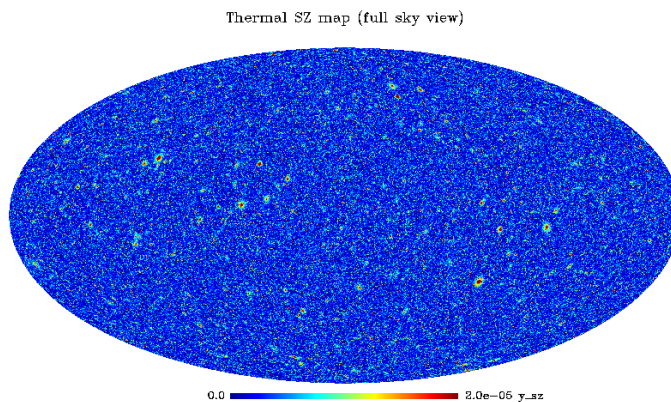


Figure 4.19: Mollview projection of the thermal SZ map regarding the fiducial CGBH model.

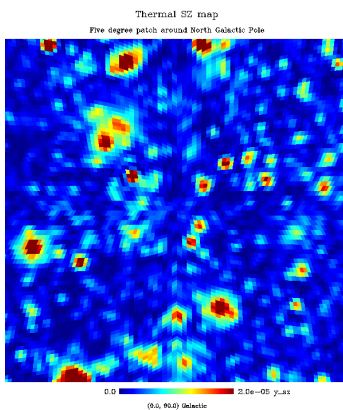


Figure 4.20: Gnomview thermal SZ patch regarding the fiducial CGBH model.

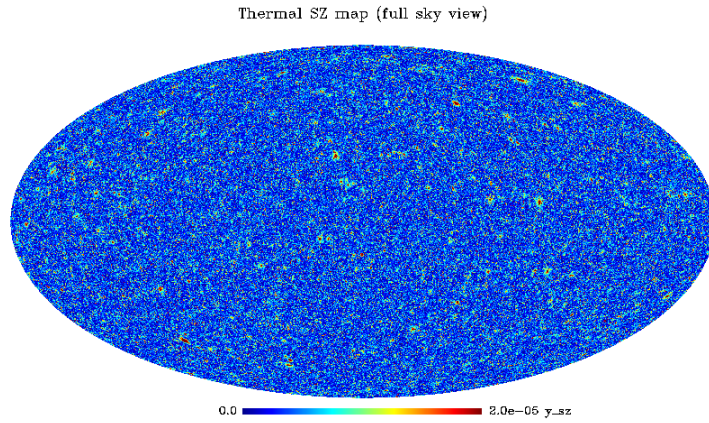


Figure 4.21: Thermal SZ map of a CGBH model with $r_0=0.750$ Gpc (the remaining parameters are set to their fiducial value).

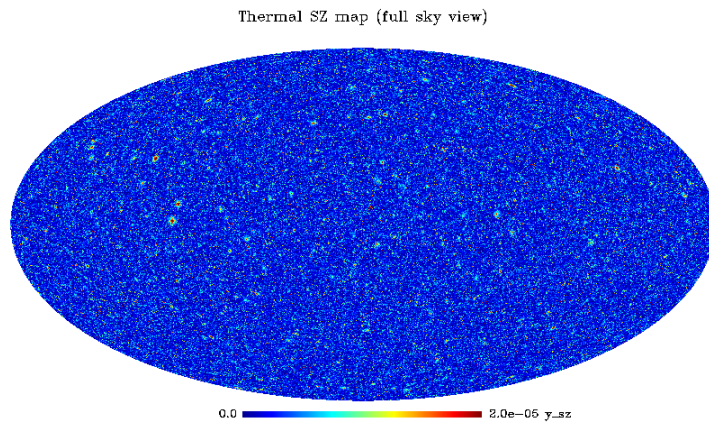


Figure 4.22: Thermal SZ map of a CGBH model with $r_0=2.5$ Gpc (the remaining parameters are set to their fiducial value).

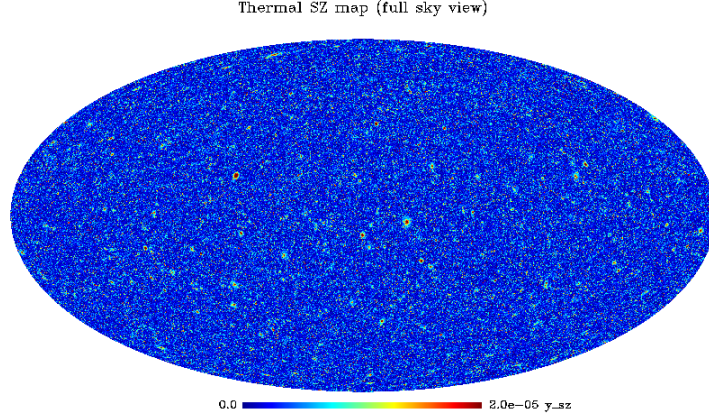


Figure 4.23: Thermal SZ map of a CGBH model with $\Delta r=0.250$ Gpc (the remaining parameters are set to their fiducial value).

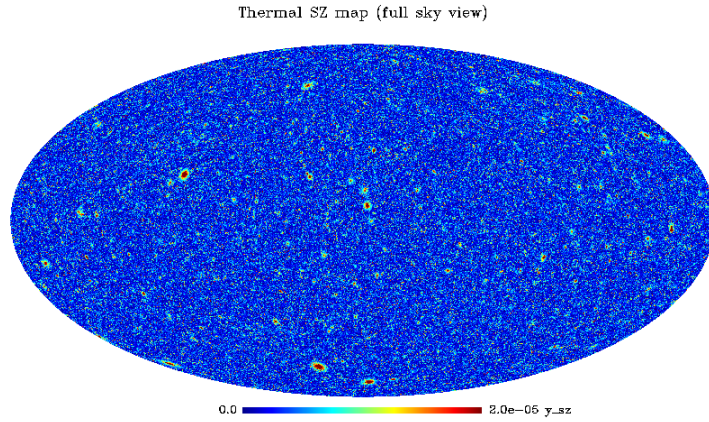


Figure 4.24: Thermal SZ map of a CGBH model with $\Delta r=0.750$ Gpc. (the remaining parameters are set to their fiducial value).

4.4.2 Map statistics

As before, the next step is computing the mean value of the SZ signal, $\overline{y_{SZ}}$, and the variance.

Fiducial CGBH model	
	$\Omega_{in}=0.3, r_0 = 1.5, \Delta r=0.5, h = 0.7$
$\overline{y_{SZ}}$	3.565E-06
σ^2	1.373E-11

Table 4.6: *SZ mean y -distortion and variance in maps obtained with the first order modification methods for the fiducial CGBH model.*

Dependence with Δr (Gpc)		
	0.250	0.750
$\overline{y_{SZ}}$	3.285E-06	3.622E-06
σ^2	1.335E-11	1.359E-11

Table 4.7: *SZ mean y -distortion and variance in maps obtained with the first order modification method when varying Δr .*

Dependence with h			
	0.65	0.675	0.75
$\overline{Y_{sz}}$	3.755E-06	3.659E-06	3.411E-06
σ^2	1.287E-11	1.319E-11	1.525E-11

Table 4.8: *SZ mean y -distortion and variance in maps obtained with the first order modification method when varying h .*

Dependence with Ω_{in}			
	0.1	0.2	0.4
$\overline{y_{SZ}}$	2.046E-06	2.809E-06	4.266E-06
σ^2	1.185E-11	1.229E-11	1.466E-11

Table 4.9: *SZ mean y -distortion and variance in maps obtained with the first order modification method when varying Ω_{in} .*

	Dependence with r_0 (Gpc)			
	0.750	1	2	2.5
$\overline{y_{SZ}}$	4.636E-06	4.258E-06	3.153E-06	2.908E-06
σ^2	1.822E-11	1.705E-11	1.110E-11	1.272E-12

Table 4.10: *SZ mean y -distortion and variance in maps obtained with the first order modification method when varying r_0 .*

4.4.3 Power Spectrum

Figure 4.25 shows the angular SZ power spectra obtained in our maps for the different values of r_0 . The power spectra for the different values of Δr , h , and Ω_{in} are depicted in Figures 4.26, 4.27 and 4.28, respectively. These results will be discussed in Section 5.

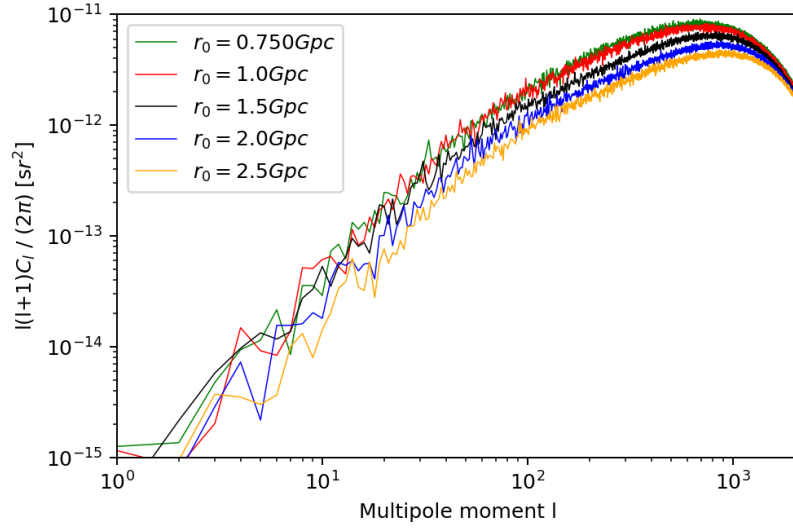


Figure 4.25: *Thermal SZ angular power spectrum of the CGBH model for the different values of r_0 .*

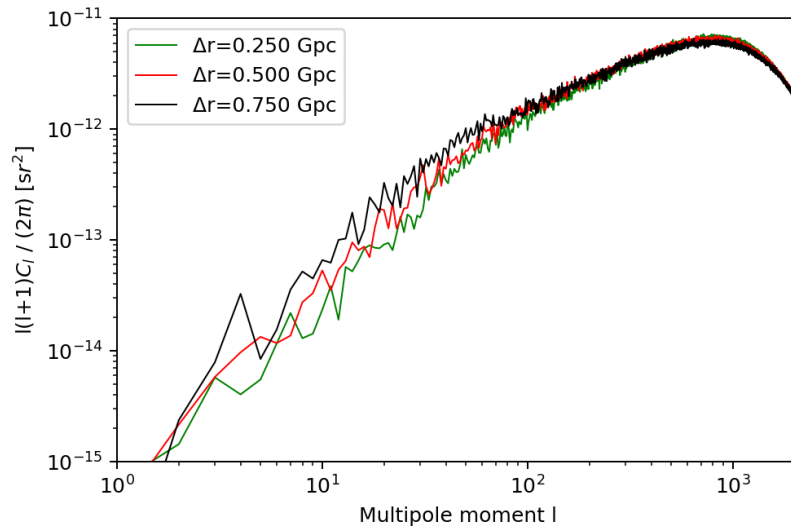


Figure 4.26: Thermal SZ angular power spectrum of the CGBH model for the different values of Δr .

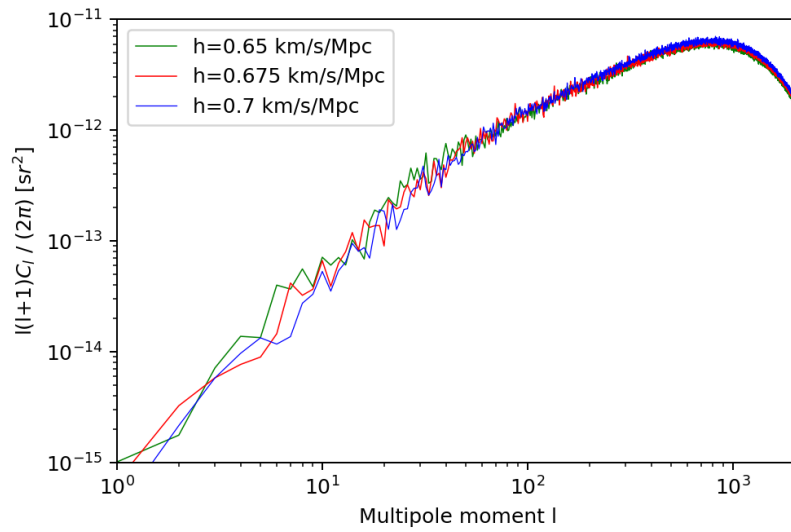


Figure 4.27: Thermal SZ angular power spectrum of the CGBH model for the different values of h .

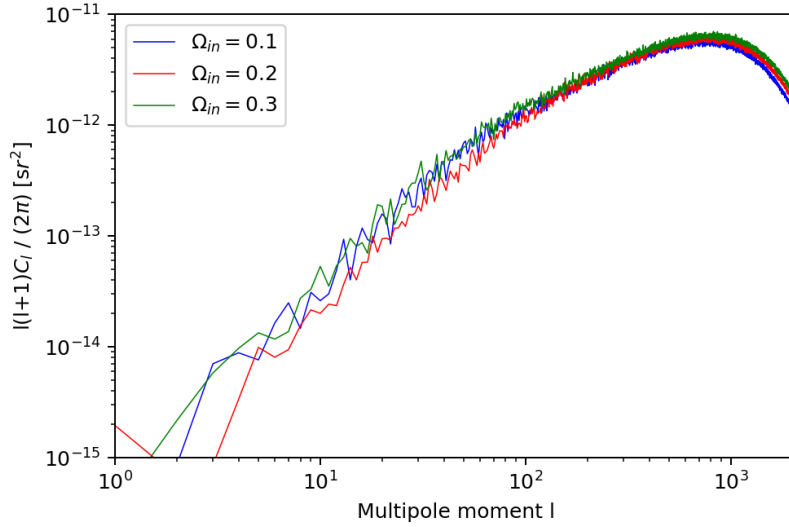


Figure 4.28: *Thermal SZ angular power spectrum of the CGBH model for the different values of Ω_{in} .*

4.4.4 Redshift dependence of the $f(t(z), r(z))$ function

A key quantity modelled in our (first order modification) method is the mass function. This was modified according to the method described in Section 2.2.5, that requires the computation of the $f(t(z), r(z))$ function for the incoming light-rays from clusters. In this section we study the impact of the different CGBH model parameters on f , which encapsulates the deviation of the standard Tinker mass function to the mass function in a LTB framework (that was not changed in our zero order modification method).

The evolution of $f(t(z), r(z))$, see Eq. (2.61), with regard to the different parameters is depicted in Figures 4.29, 4.30, 4.31 and 4.32. The discussion of these plots will be done in Section 5.

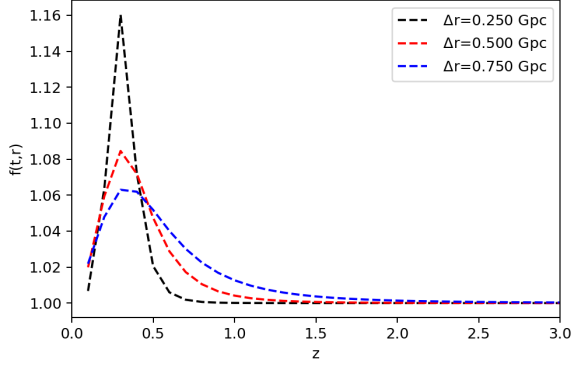


Figure 4.29: $f(t, r)$ for different values of Δr .

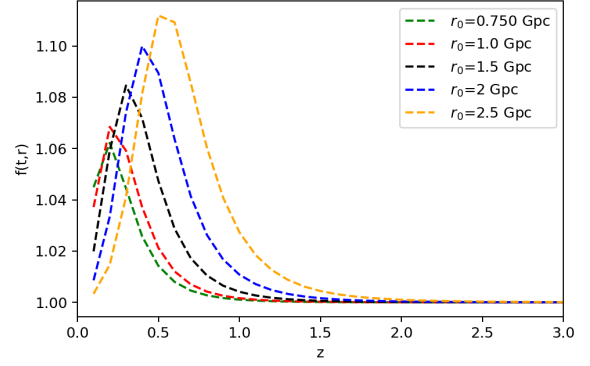


Figure 4.30: $f(t, r)$ for different values of r_0 .

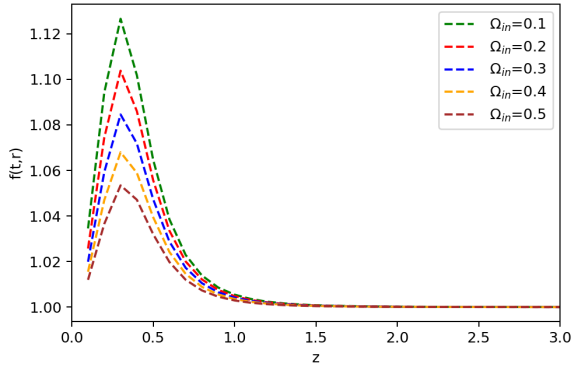


Figure 4.31: $f(t, r)$ for different values of Ω_{in} .

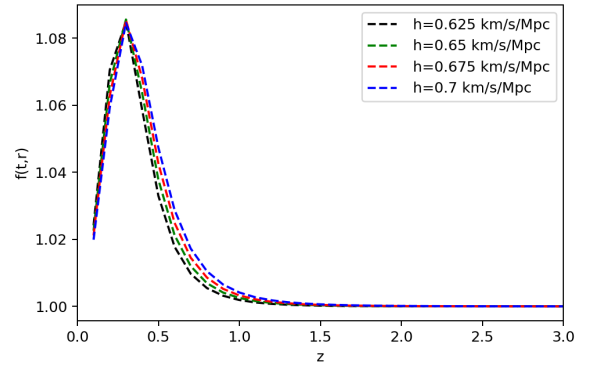


Figure 4.32: $f(t, r)$ for different values of h .

4.5 Comparison Between Zero and First Order Modifications

Below it is represented the comparison between the thermal SZ maps and the power spectra for the fiducial CGBH model for both zero and first order modifications for map realizations with the same random number generator's seed. The maps are a reprint of Figures 4.15 and 4.19 and are placed here to facilitate comparison. One important consequence of changing the mass function to the LTB framework (first order modification method) is that the number of clusters derived from the poison deviates of the mass function in each shell will

be different in the zero and first order modification methods. This is why we do not see clusters in the same locations in the maps of Fig. 4.33, even if we use the same random seed, because the number of cluster drawn in each shell are different in each method. Figure 4.34 shows thermal SZ power spectra of the fiducial CGBH model obtained from the maps in Fig. 4.33. We will discuss this results in Section 5.

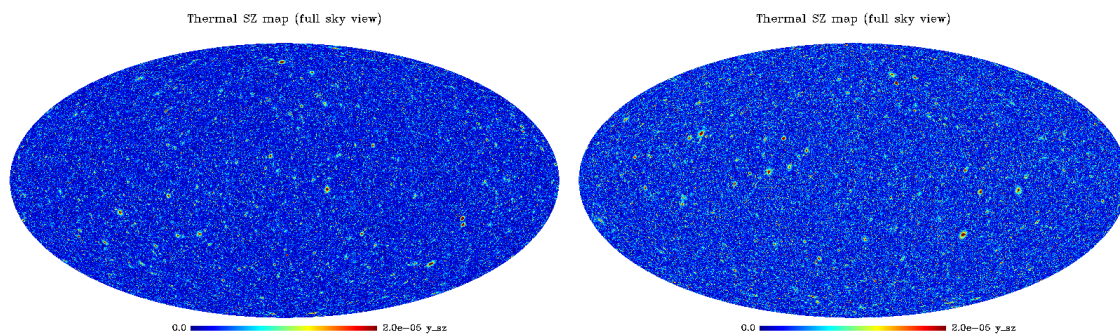


Figure 4.33: Thermal SZ maps of the fiducial CGBH model obtained with the zero order (left) and first order (right) modification methods.

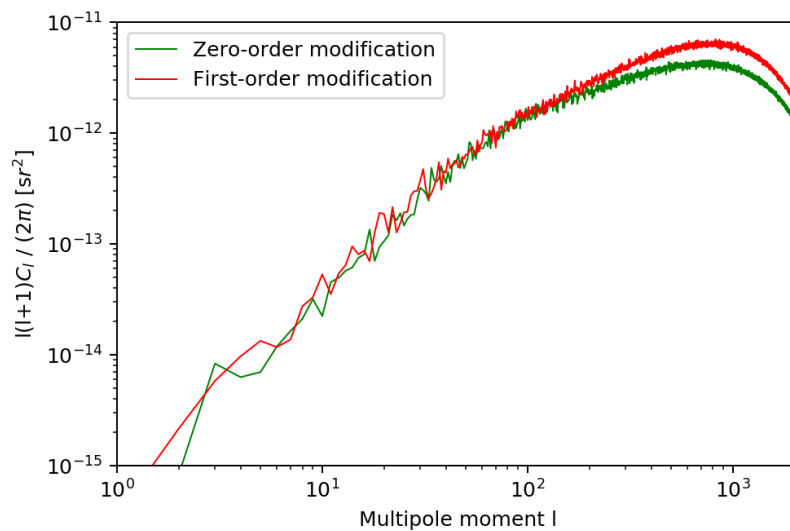


Figure 4.34: Power spectra of the fiducial CGBH model: Zero order modification (green line) and first order modification (red line).

4.6 Comparison between CGBH and FLRW

Finally, we wish to compare the results with the standard FLRW model. For this, we compare the results from the CGBH model with the standard FLRW model setting $\Omega_M = 0.3$ and $\Omega_M = 1$ as described in Section 3. In both runs the Hubble parameter was set to $h = 0.67$ and the remaining parameters match the ones in the CGBH framework. In particular all models (CGBH and FLRW) were run with the same $\sigma_8(z = 0) = 0.8$ normalization.

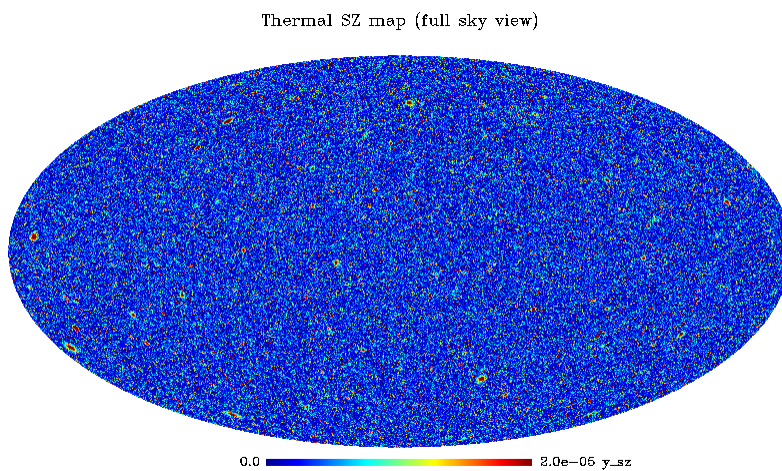


Figure 4.35: *Thermal SZ map for the standard FLRW model with $\Omega_M = 1$.*

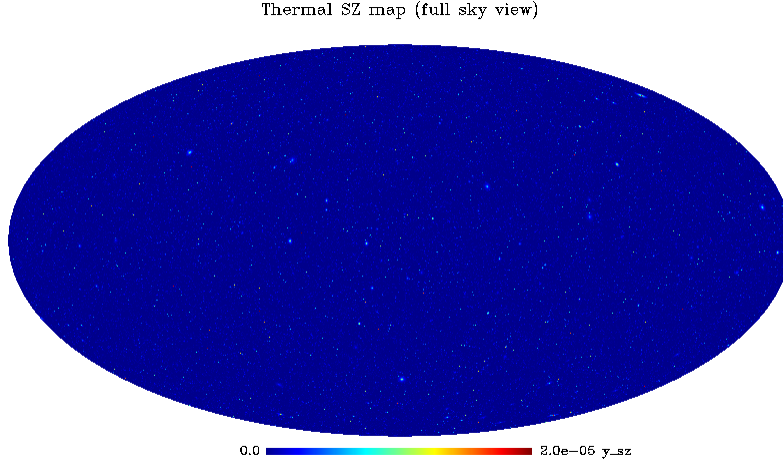


Figure 4.36: Thermal SZ map for the standard FLRW model with $\Omega_M = 0.3$.

Table 4.11 shows the mean and variance of the thermal SZ signal for the FLRW map realizations of Figures 4.35 and 4.36.

	FLRW model	
	$\Omega_M = 0.3$	$\Omega_M = 1$
$\overline{y_{sz}}$	1.661E-07	3.965E-06
σ^2	2.997E-13	3.012E-11

Table 4.11: SZ mean y -distortion and variance in maps regarding the FLRW model with $\Omega_M = 0.3$ and $\Omega_M = 0.1$.

4.6.1 Map histogram comparison

Next, we present pixel histograms, Fig 4.37, for the for the zero order and first order CGBH map realizations and for the critical density, $\Omega_M = 1$, FLRW model. These results will also be discussed in Section 5.

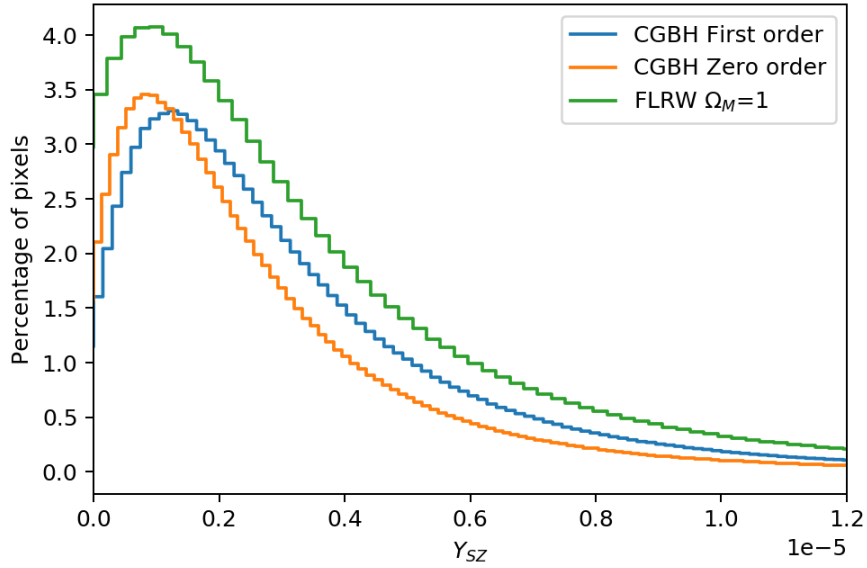


Figure 4.37: Comparison between the histograms of the distribution of pixels of the fiducial CGBH model with FLRW with $\Omega_M = 1$

4.6.2 Power Spectrum

Figure 4.38 shows a comparison of the thermal SZ power spectra for the FLRW and CGBH models. We note that all models assume the same h and $\sigma_8(z = 0)$ normalization and therefore the angular SZ power spectra obtained for the FLRW do not necessarily match results where these models are considered with different $\sigma_8(z = 0)$ normalizations (that try to reproduce the local abundance of galaxy clusters, see e.g. the results from numerical simulations in [51, 30]).

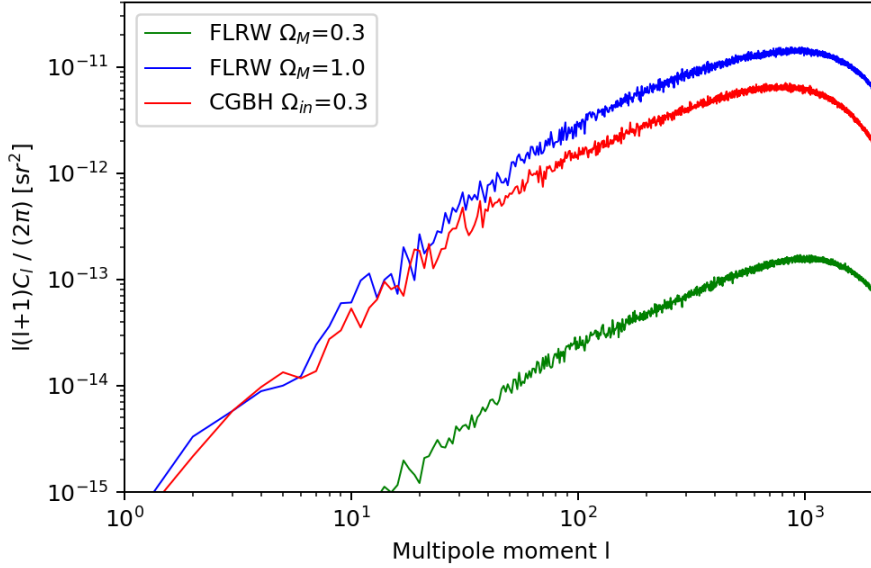


Figure 4.38: Comparison between the power spectra of the fiducial CGBH model with $\Omega_{in} = 0.3$ (red line) and the standard FLRW model with curvature with $\Omega_M = 1$ (blue line) and with $\Omega_M = 0.3$ (green line)

4.7 Catalogues of Galaxy Clusters

The catalogues of galaxy clusters generated by the PSM code contain the following properties: galactic longitude and latitude, redshift, cluster virial mass, radial and transverse cluster velocity, angle of transverse velocity, core and virial radius and integrated Y_{SZ} signal (often called “SZ luminosity”) of clusters. Figure 4.39 shows the Y_{SZ} cluster luminosity distributions for the CGBH zero and first order modification and $\Omega_M = 1$ FLRW catalogues. In Figure 4.40 we see cluster number counts, $N(z)$, as function of redshift for the same set of catalogues. The code generates these catalogues assuming a minimum mass of $M_{min} = 10^{14}M_{\odot}$. Other catalogue quantities, such as cluster velocities and the kinetic SZ effect were not modified by this work, so they will not be addressed here.

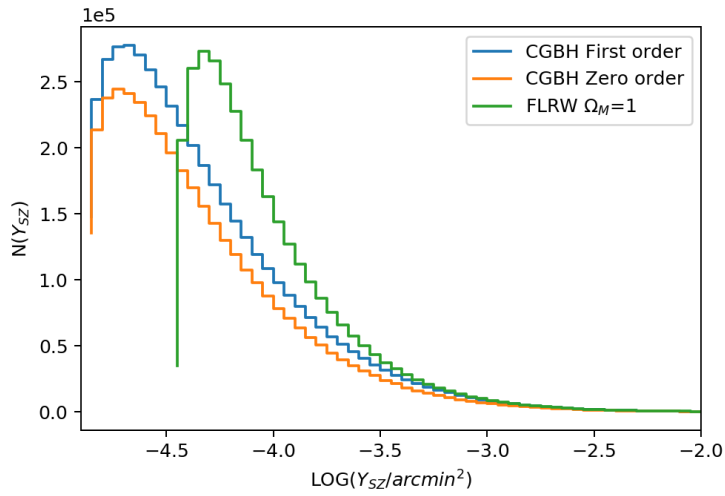


Figure 4.39: Distribution of cluster integrated Y_{SZ} luminosities for the fiducial CGBH (zero and first order modification) model and FLRW model with $\Omega_M = 1$. These catalogues assume a minimum mass of $M_{min} = 10^{14} M_{\odot}$.

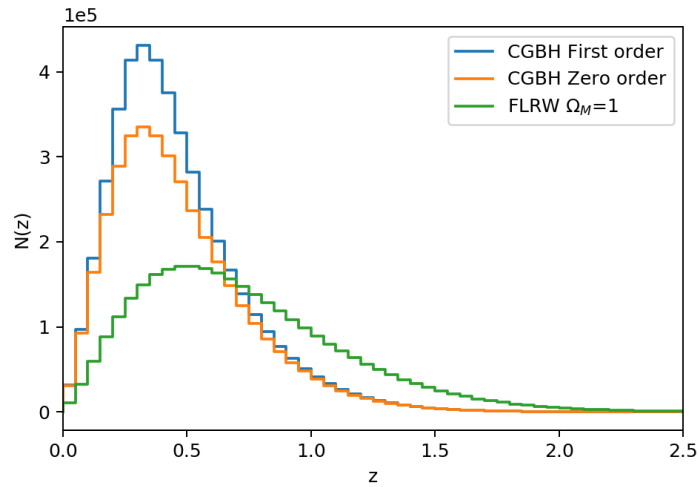


Figure 4.40: Redshift distribution of (all-sky) galaxy cluster number counts, $N(z)$, for the fiducial CGBH model and FLRW model with $\Omega_M = 1$. These catalogues assume a minimum mass of $M_{min} = 10^{14} M_{\odot}$.

Chapter 5

Discussion

5.1 LTB Density profile

We start by analysing the dependence of the CGBH density profile, Ω_M , on the model parameters that we vary in this thesis. This is presented in the figures of Section 4.1. When plotting Ω_M with respect to a certain parameter, the remaining ones are set to their fiducial value (see Table 4.1). Figure 4.1 shows the dependence of $\Omega_M(r)$ on the r_0 parameter. As the value of r_0 increases the lines undergo a translation to the right. For instance, the leftmost line represents $r_0 = 0.750$ Gpc and the rightmost line represents $r_0 = 2.5$ Gpc. This means that the density function profile $\Omega_M(r)$ will reach its asymptotical value of 1 much faster in models where r_0 is smaller. For example, a model with $r_0 = 0.750$ Gpc reaches $\Omega_M = 1$ at $r \approx 3$ Gpc whereas a model with $r_0 = 2.5$ Gpc hits the same value only at $r \approx 5$ Gpc. This makes sense because the larger the r_0 , the biggest is the void and the Universe becomes asymptotically Einstein-de-Sitter at larger scales. In Figure 4.2 it is observed the change of $\Omega_M(r)$ when varying the Δr parameter. The red line represents the fiducial model with $\Delta r = 0.5$ Gpc, the leftmost line represents $\Delta r = 0.250$ Gpc and the rightmost line represents $\Delta r = 0.750$ Gpc. It can be observed that the density function profile Ω_M will reach its asymptotical value of 1 at smaller distances when Δr is smaller. Indeed, a model with $\Delta r = 0.250$ Gpc reaches $\Omega_M = 1$ at $r \approx 3$ Gpc while a model with $\Delta r = 0.750$ Gpc hits the same value only $r \approx 5$ Gpc. Therefore, one can conclude that the smaller the value of Δr , the smaller the scale at which $\Omega_M = 1$. For larger values of Δr , the biggest is the distance at which an asymptotically FLRW arises. This makes sense since Δr characterises the transition to uniformity. Larger values of Δr reflect a smoother transition

from inside to outside the void, which in turn means a smoother variation of Ω_M until its asymptotical value. In Figure 4.3 the variation of $\Omega_M(r)$ is represented for several values of Ω_{in} . It can be observed that independently of the value of Ω_{in} , the density profiles reach the asymptotical value of 1 at the same scale. This is natural since this parameter only translates the matter density inside the void and the other parameters are fixed to their fiducial value. Outside of it, when $r \gg r_0$ and the Universe becomes a FLRW Universe with density Ω_{out} . Finally, in Figure 4.4 the change of $\Omega_M(r)$ is plotted for different values of h . We can conclude that Ω_M is not h -dependent, as it presents the very same evolution for the different values of this parameter. This is natural since the expression of $\Omega_M(r)$ in Eq. (2.20) is independent of h .

5.2 Redshift dependence of r , d_A , dV/dz , H_T and H_R

The plots concerning the redshift evolution of the angular diameter distance, Hubble rates and volume element as the CGBH parameters vary are shown in Section 4.2. Our results demonstrate that the angular diameter distance is scarcely sensitive to Δr and Ω_{in} as Figs. 4.7 and 4.9 show. A small variation of this quantity can be noticed when varying r_0 , Fig. 4.8, although it presents a significant dependence on h as Fig. 4.10 displays. The curves are identical below $z \approx 0.5$ but from that redshift, the higher is this parameter, the lower is the angular diameter distance.

From the results, it is clear that the volume element is not sensitive to Ω_{in} , see Fig. 4.13. The volume element presents a small dependence on Δr (Fig. 4.11) and on r_0 (Fig. 4.12) but is highly sensitive to h , see Fig. 4.14. Figure 4.6 shows the evolution of the transverse Hubble rate H_T and the radial Hubble rate H_R with the scale r taken at the current time for the central observer (left panel) and with redshift (right panel). As such, from the plot we conclude that these two rates are indistinguishable from $r \approx 4$ Gpc, ($z > 1$), since the Universe is asymptotically FLRW outside the void and the two rates become the same.

5.3 Zero Order Modification

Figure 4.15 shows a thermal SZ map regarding the fiducial CGBH model. The redder the spots, the stronger is the y_{SZ} signal. Clusters on these maps have a very small angular size because it is an all-sky projection where the sky has a total of about 54 thousand degrees. In figures 4.16 and 4.17 the same maps are shown for $\Omega_{in} = 0.1$ and $\Omega_{in} = 0.5$. There is a clear

difference between the images as the map of $\Omega_{in} = 0.5$ features more spots and as it shows in general a brighter, greenish colour. This is logical since this parameter controls the matter quantity inside the void. A higher value of Ω_{in} implies a higher number of galaxy clusters since the density ρ_m was altered to a LTB framework where now is distance-dependent. This in turn will make the mean SZ signal, $\overline{y_{SZ}}$, to increase as it is proportional to the electron number density, see Eq. (2.45). Then, the statistics for the different values of Δr are displayed in Table 4.2. The highest value of $\overline{y_{SZ}}$ when varying Δr is at $\Delta r = 0.750$ Gpc while the lowest is at $\Delta r = 0.250$ Gpc. Since the angular diameter distance is not dependent on this parameter, Fig. (4.7), this can be explained by noting that until $z \approx 0.5$ the matter density function $\Omega_M(r)$ is higher for higher values of this parameter, Fig. (4.2).

Regarding the h parameter, as Table 4.3 shows, the highest the value of h , the lowest is $\overline{y_{SZ}}$. The angular diameter distance is highly sensitive to this parameter (Fig. 4.10) and for higher values of h , the value of this quantity is overall lower. This effect alone would imply an increase in the mean $\overline{y_{SZ}}$ signal in the maps, but the opposite is observed. This may be explained by the fact that h also enters in the calculation of the electron number density and the temperature-mass relation evolution along the line-of-sight integration, leading to the observed behaviour of the $\overline{y_{SZ}}$ signal. Regarding the variation of Ω_{in} , through Table 4.4 it is clear that a higher value of Ω_{in} translates into a higher value of $\overline{y_{SZ}}$. Again, as the angular diameter distance does not evolve significantly when this parameter varies, Fig. (4.9), the reason for this is the same given above when comparing the SZ thermal maps: a higher value of Ω_{in} means a higher matter content inside the void which translates into a higher number of galaxy clusters which in turn makes the SZ signal to rise. Finally, the last Table 4.5 concerns the variation with the r_0 parameter. It is explicit that the highest is r_0 , the lowest is $\overline{y_{SZ}}$. The variation of the angular diameter distance with this parameter, Fig. (4.8), is not enough to explain these differences. As mentioned, r_0 is the typical size of the void. This means that a CGBH model with larger voids have a tendency to be linked to lower values of $\overline{y_{SZ}}$. The largest is the void, the highest is the transition redshift from which the Universe becomes described by an asymptotically, cluster-richer FLRW metric and the less galaxy clusters this Universe owns. Contrariwise, the smaller is the void, the smaller is the redshift transition and the more clusters lie in the sky, increasing the overall value of $\overline{y_{SZ}}$.

The power spectrum when Ω_{in} varies is plotted in Fig. 4.18. The change in the volume element regarding the variation of this parameter, Fig. 4.13, is not significant to explain these variations. As seen before when analyzing the SZ signal, as Ω_{in} increases there is

a higher abundance of objects since the mass function also increases as the density ρ_m was modified to vary from shell to shell. Ω_{in} is the lowest value of the density function profile Ω_M , therefore if we start the modelation with a higher value, more objects will be generated independently of the value of the volume element. The power spectra have a peak for $l \approx 1000$ and then decreases. A common feature to all power spectra is a decaiment for larger multipoles l . As the angular power spectra is highly sensitive to the volume element and the mass function, Eq. (2.50), for larger multipoles l the number of small angular sized objects decay and the power starts to diminish.

5.4 First Order Modification

The results regarding the first order modifications can be found in Section 4.4. Figures 4.21 and 4.22 show thermal SZ maps for $r_0=0.750$ and $r_0=2.5$ Gpc respectively. Figure 4.19 is the same map for the fiducial model ($r_0=1.5$ Gpc). There is a remarkable difference between these maps as the one with smaller value of r_0 presents a more lighter, greenish colour and more bigger spots representing galaxy clusters. On the contrary, the map with $r_0=2.5$ Gpc is bluer and has less spots. This feature translates into higher values of $\overline{y_{SZ}}$ as this parameter decreases (Table 4.10). The explanation for this is the same given above regarding the zero order modifications. Figures 4.23 and 4.24 show the same type of maps when varying Δr . A higher value of this parameter reflects a lighter, greenish map with more galaxy clusters. The same conclusion can be drawn by observing Table 4.7 where $\overline{y_{SZ}}$ increases as the parameter increases. The cause for this is identical to the one described in the previous section. The $\overline{y_{SZ}}$ for different values of h can be found in Table 4.8. Once again, as this parameter increases its values $\overline{y_{SZ}}$ also grows. The same analysis but with respect to the Ω_{in} is represented in Table 4.9. As Ω_{in} rises the same happens to $\overline{y_{SZ}}$. The explanation for both parameters h and Ω_{in} is the very same as for the zero order modifications.

The power spectra regarding the CGBH model for the different values of r_0 are displayed in Figure 4.25. The black line corresponds to $r_0=1.5$ Gpc. As it can be observed, the higher the value of this parameter, the overall power is lower. The same behaviour is seen regarding the mean SZ signal $\overline{y_{SZ}}$. From a certain multipole, all lines seem to converge. This makes sense since from a certain stage, the volume element and $f(t, r)$ are the same regardless of the value of this parameter (Figs. 4.12 and 4.30). As mentioned before, a lower r_0 translates into a smaller void and so the Universe becomes FLRW earlier, at lower redshifts. If it is

FLRW sooner, there will be more galaxy clusters and the mass function yields higher values. Observing Fig 4.30, for lower r_0 , at lower redshifts $f(t,r)$ is higher. So, the function $f(t,r)$ increases the mass function at lower redshifts for lower r_0 but for higher redshift the opposite happens. Besides, $f(t,r)$ makes the peak of the different curves of Fig. 4.25 to undergo a small translation contrary to what happened when varying Ω_{in} as the peaks are at the same multipole l . The same power spectra are displayed for the different values of Δr in Fig. 4.26. These plots differ for small values of l but then they are very similar for $l > 100$. The volume element has a slight dependence on this parameter (Fig. 4.11) as in the range of $z = [0.25, 0.5]$ the curve corresponding to $\Delta r = 0.250$ Gpc dominates. Besides, the $f(t,r)$ function evolves significantly when this parameter varies, see Fig. 4.29. From that figure, it is clear that the curve corresponding to the same value of Δr dominates in the same redshift range. This makes the power spectra for this value to dominate for low l . As seen before, higher values of Δr translate into stronger SZ signals. In fact, the highest value of Δr dominates until a certain phase but then the $f(t,r)$ function comes into play as it makes the mass function of lower values of Δr to yield higher values and to increase the overall power. In that range of redshift, the volume element also favours lower values of Δr .

The power spectra when varying Ω_{in} are displayed in Fig. 4.28. The reason for its behaviour is similar as the one given in the zero order modifications. However, now the $f(t,r)$ function comes into play in the mass function. Inspecting Fig. 4.31 we observe that lower values of Ω_{in} have a higher $f(t,r)$ function. That is why the power spectra curves from the zero order to the first order modification rise and get closer to each other as the lower values of Ω_{in} undergo a bigger rise. The power spectra when varying h is depicted in Fig. 4.27. The volume element is favouring lower values of h (Fig. 4.14) which translates into higher power for these multipoles. Then, from a certain redshift, $f(t,r)$ starts favouring higher values of h . These two effects make the power spectrum to be almost identical for the different values of h from $l \approx 90$ onward.

Finally, the plots for the evolution of $f(t,r)$ are depicted in Section 4.4.4 and in figures 4.29, 4.30, 4.31 and 4.32. The first obvious feature of these plots is $f(t,r)$ going asymptotically to 1. This is in accordance with Eq. (2.61) and with Eq. (2.62). For large redshifts the shear ϵ vanishes as the Hubble rates are indistinguishable, see Eq. (2.63) and Figure 4.6. When there is no shear, the numerator and denominator of Eq. (2.61) are asymptotically the same, which reflect the fact that these LTB models are asymptotically Einstein-de-Sitter described by a FLRW metric. Then, it is clear that $f(t,r)$ is sensitive

to every parameter although it does not evolve much when h varies. Figure 4.29 shows the variation of $f(t, r)$ with Δr . The lower the value of this parameter, the higher $f(t, r)$ reaches and the more narrow is the plot and the faster it reaches $f(t, r) = 1$. When r_0 increases (Fig. 4.30), $f(t, r)$ reaches a higher value and the plot is wider and reaches $f(t, r) = 1$ at later stages. However, when Ω_{in} varies (Fig. 4.31), the plots make it to $f(t, r) = 1$ at the same redshift but for higher values of this parameter the maximum value of $f(t, r)$ is lower and the plot is slightly more narrow. As mentioned, almost no change is observed when h is varied (Fig. 4.32) besides a small increment on the plot's width as this parameter increases.

5.5 Comparison between Zero and First Order Modification

The results regarding the comparison between zero and first order modification can be found in Section 4.5. First, a thermal SZ map regarding zero and first order modifications for the fiducial CGBH model are displayed in the left and right panels of Figure 4.33, respectively. The first order modification map exhibits more red and green spots than the zero modification one and it is in general lighter, anticipating a higher $\overline{y_{SZ}}$. Indeed, comparing tables 4.1 and 4.6, the zero order modification yields $\overline{y_{SZ}} = 2.876 \times 10^{-6}$ while the other one yields $\overline{y_{SZ}} = 3.565 \times 10^{-6}$. The same conclusion can be drawn by inspecting their power spectra in Figure 4.34. The two plots are very similar until $l \approx 100$. From there, the first order modification power is slightly higher than the other one. The difference between these two concern the modification of the mass function. That being said, we can conclude that by modifying the mass function to a LTB framework it increases, in general, the number of galaxy clusters in the sky and consequently the mean SZ signal $\overline{y_{SZ}}$ and the thermal SZ power spectrum.

5.6 FLRW Framework and Comparison With CGBH Model

In Section 4.6 the results comparing the fiducial CGBH model (first order modification) and FLRW model are shown. Figure 4.38 shows the power spectra of the FLRW model with $\Omega_M = 1$, $\Omega_M = 0.3$ and of the fiducial CGBH model with $\Omega_{in} = 0.3$ and $\Omega_{out} = 1$. It is clear that the critical density, $\Omega_M=1$, FLRW model has a larger overall power. This can be explained by noting that all models have the same $\sigma_8(z = 0)$ normalization, and that in the LTB framework inside the void the matter density is only $\Omega_{in}=0.3$, reaching its

asymptotical value of 1 when $r \gg r_0$. In contrast, the FLRW model assumes a constant matter density of $\Omega_M = 1$ throughout the whole Universe. Comparing to the standard $\Omega_M = 0.3$ model, in the LTB Universe there is an under density provided that it is a void model where the number of clusters is less than the former model. In short, the overall LTB power is smaller because the density below the transition redshift is lower than in the FLRW model, as there are less massive clusters in the sky. The two power spectra have different forms essentially because the density matter function, the volume element and the Hubble rate are calculated in different ways. The mean y_{sz} value is much higher when $\Omega_M = 1$ ($\overline{y_{sz}} = 3.965 \times 10^{-6}$) than when $\Omega_M=0.3$ ($\overline{y_{sz}} = 1.661 \times 10^{-7}$) by a factor of ≈ 10 . The $\overline{y_{sz}}$ value for the CGBH fiducial model is $\overline{y_{sz}} = 2.87610^{-6}$) (Table 4.1). Likewise, the number of galaxy clusters when $\Omega_M = 1$ is much higher than when $\Omega_M = 0.3$ because the σ_8 parameter is fixed for both cases. That is why the green power spectra curve corresponding to $\Omega_M = 1$ is lower than the blue curve corresponding to $\Omega_M = 0.3$. In Figure 4.37, a histogram for the fiducial CGBH and FLRW model can be observed. The histograms of the distribution of pixels are not Gaussian, rather, it contain a long tail for higher y_{SZ} values. When perturbations grow linearly, the fluctuations in the sky are described by a Gaussian distribution. When the distribution is not Gaussian, as is the case, there are deviations due to non-linear growth of structures. These non-linear-evolving structures, as is the case of clusters of galaxies, are responsible for this deviation from a Gaussian distribution.

5.7 Catalogues of Galaxy Clusters

The results regarding the catalogues of galaxy clusters are displayed in figures 4.39 and 4.40. The integral of the curves yields the total number of objects in the catalog. There is a clear enhancement from the zero to the first order modification as the mass function is being altered. We conclude that these number counts are sensitive to the underlying cosmology as the shape of the curves change according to the model employed.

5.8 Future Steps

5.8.1 Cluster mocks, kinetic SZ and emulators for parameter inference

A future step would be to extend this method to ALTB models. This code is flexible as it is prepared to work with the main LTB quantities and generate catalogues regardless of the type of the model we are employing, as long as the quantities are calculated in the procedure. Extending this software to predict catalogues with optical cluster observables, such as cluster richness, and integrated mass maps they may be used to study model signatures and galaxy surveys - CMB/SZ (eg Euclid - Planck) correlations. Having the catalogues and maps, we would then confront theoretical predictions against SZ (Planck) observations and optical catalogues from existing galaxy surveys (eg SDSS/MAXBSG). From there it is possible to create mock simulations of galaxy clusters that Euclid will observe by employing other observables, such as cluster number counts and scaling laws. These mock simulations are needed to compute covariance functions for cosmological parameter inference with galaxy clusters identified in galaxy surveys. As this work is focused on the thermal SZ effect concerning the DMB method, the kinetic effect has not yet been modified to a LTB framework. The kinetic effect is an important observable to constrain LTB models. We plan to modified that component of the DMB/PSM method in the near future, by implementing a correct modelation of the cluster velocities computed in LTB theory. This implementation is also crucial to obtain the correct (longitudinal and transverse) velocity information that is being output to the cluster catalogues, by our modified version of the PSM code. This is quite relevant as galaxy surveys are sensitive to dipole terms and for that a correct modelation of the velocities in LTB is needed.

Another future step would include speed up parameter inference codes by building emulators of observed quantities. The main objective would be to calculate the power spectra C_l and other observables, such as cluster number counts, in a faster way. This is important because the computation of these quantities is time consuming for LTB models and Bayesian inference codes require fast computation of theoretical predictions of observable quantities over a wide range of model parameters in a multi-dimensional space. We would like to approach this problem in the future, by constructing emulators of cluster observables by using supervised machine learning (ML) methods. The emulator would use the our existing tools to compute theoretical predictions for cluster observables, such as the angular power spectrum, and cluster number counts to build a regression ML model

as a function of the LTB model parameters. For the CGBH we would use the 4 parameters considered in this thesis, and then would combine these emulators with Bayesian Monte-Carlo-Markov Chain (MCMC) codes to fast estimate model predictions for the MCMC random walks and to compute the posterior distribution of the parameters given the observed data. This emulator is built by training an algorithm from the data points of the PSM runs. For instance, we could train a neural network (NN) and optimize its parameters to better adjust the parameters with the observables. The test set would verify the results and this NN would be ready to receive parameters and to predict observables like C_l , number counts and scaling relations.

5.8.2 Lensing and Scaling relations

This methodology can be extended to weak lensing studies by generating weak lensing convergence maps. To test our LTB results with EUCLID surveys we would apply a $Y_{SZ} - M$ scaling relation for the clusters. An important Euclid cluster observable is the cluster richness. Euclid will provide catalogues containing several thousands of observed cluster richness and mass. Therefore, we would need to employ a mass-richness relation (see equation 2.44) to compute cluster richness from mass in our modified version of the PSM code. This would allow us to generate theoretical LTB cluster richness catalogues and to use these with supervised emulators in parameter inference codes (see previous section). The PSM code implements already the first three scaling relations (eqs. 2.40 to 2.42) to predict integrated SZ signal for the simulated clusters in the catalogues. We would add eq. (2.44) to the PSM model so that it can also predict cluster richness in the simulated catalogues. The cluster richness is the number of member galaxies, visible in the optical or infra-red galaxy surveys. In the microwave the observable is the Y_{SZ} , the SZ luminosity. In the optical we see galaxies and we count how many of them lay in a cluster and then compute the relation between number of galaxies and mass. These scalings are sensitive to the formation history of clusters and to the underlying cosmology. Our implementation for the LTB version of the PSM code would have an impact in the $E(z)$ function. Before integrating the richness mass scaling in the PSM model we will fit eq. (2.44) and eq. (2.43) with cluster observations of Y and N and masses estimates from lensing observations. This would be a first test of LTB models using these scaling relations.

Chapter 6

Summary

One of the assumptions of the cosmological principle is the statement that the Universe is homogeneous at "sufficiently large-scales". It is not well established how large these scale should be and if this assumption is the best to describe current observations. The upcoming ESA/Euclid satellite mission will test this paradigm over a wide range of scales allowing us to assess whether the non-homogeneous Lemaitre-Tolman-Bondi (LTB) models should be considered to accurately describe observations locally and at intermediate cosmological scales. This thesis focused on addressing the problem of modeling the galaxy cluster population in the context of LTB models, and the development of new numerical tools that may be used to provide ways of confronting model predictions with CMB (e.g. Planck) and galaxy survey (e.g. Euclid) observations of galaxy clusters. We modified the thermal SZ component of the DMB method in the PSM code according to a LTB framework, by employing the CGBH model. Our modifications were implemented using pre-computed tables of the essential quantities of the theoretical model (e.g. angular diameter distances, volume element, mass function). We used the code Bubble to create these tables for the CGBH model, but our implementation can be directly applied for other LTB models if the correct tables are provided to the code. We divided our work in two stages, the first relating to the background properties of the Universe and the second to the mass function and perturbations. We then performed statistical analysis to obtain the power spectra, the SZ signal and also catalogues of galaxy clusters. These catalogues allow us to compute, for the first time, mock simulations of clusters in LTB framework crucial for further parameter inference using, for example, galaxy cluster number counts. Our results show a clear difference between the

first and second stage of modifications regarding the CGBH model, as the power spectra and SZ signal yield an overall higher power for the latter model. Besides, the results also indicate a cosmology-dependence of the distribution of cluster abundances and Y_{sz} signal with redshift, which is an indication of the importance of using these observables to constrain LTB model parameters. Having the catalogues and maps, the future steps would be to confront theoretical predictions against SZ (Planck) observations and optical catalogues from existing galaxy surveys (eg SDSS/MAXBSG). The study in this project is timely and innovative. The work performed is crucial to generate thermal SZ maps and catalogues to create mock simulations to further prepare galaxy surveys and to do cross-correlations of the CMB with galaxy surveys concerning the forthcoming ESA/Euclid mission.

References

- [1] J. Delabrouille, J. B. Melin, and J. G. Bartlett. Simulations of Sunyaev-Zel'dovich Maps and Their Applications. In Lin-Wen Chen, Chung-Pei Ma, Kin-Wang Ng, and Ue-Li Pen, editors, *AMiBA 2001: High-Z Clusters, Missing Baryons, and CMB Polarization*, volume 257 of *Astronomical Society of the Pacific Conference Series*, page 81, January 2002.
- [2] K. M. Górski, E. Hivon, A. J. Banday, B. D. Wandelt, F. K. Hansen, M. Reinecke, and M. Bartelmann. HEALPix: A Framework for High-Resolution Discretization and Fast Analysis of Data Distributed on the Sphere. *Astrophysical Journal*, 622(2):759–771, April 2005.
- [3] Philip Bull, Yashar Akrami, Julian Adamek, Tessa Baker, Emilio Bellini, Jose Beltrán Jiménez, Eloisa Bentivegna, Stefano Camera, Sébastien Clesse, Jonathan H. Davis, Enea Di Dio, Jonas Enander, Alan Heavens, Lavinia Heisenberg, Bin Hu, Claudio Llinares, Roy Maartens, Edvard Mörtsell, Seshadri Nadathur, Johannes Noller, Roman Pasechnik, Marcel S. Pawłowski, Thiago S. Pereira, Miguel Quartín, Angelo Ricciardone, Signe Riemer-Sørensen, Massimiliano Rinaldi, Jeremy Sakstein, Ippocratis D. Saltas, Vincenzo Salzano, Ignacy Sawicki, Adam R. Solomon, Douglas Spolyar, Glenn D. Starkman, Danièle Steer, Ismael Tereno, Licia Verde, Francisco Villaescusa-Navarro, Mikael von Strauss, and Hans A. Winther. Beyond Λ CDM: Problems, solutions, and the road ahead. *Physics of the Dark Universe*, 12:56–99, June 2016.
- [4] Shahab Joudaki, Chris Blake, Catherine Heymans, Ami Choi, Joachim Harnois-Deraps, Hendrik Hildebrandt, Benjamin Joachimi, Andrew Johnson, Alexander Mead, David Parkinson, Massimo Viola, and Ludovic van Waerbeke. CFHTLenS revisited:

assessing concordance with Planck including astrophysical systematics. *Monthly Notices of the Royal Astronomical Society*, 465(2):2033–2052, February 2017.

- [5] S. Joudaki, H. Hildebrandt, D. Traykova, N. E. Chisari, C. Heymans, A. Kannawadi, K. Kuijken, A. H. Wright, M. Asgari, T. Erben, H. Hoekstra, B. Joachimi, L. Miller, T. Tröster, and J. L. van den Busch. KiDS+VIKING-450 and DES-Y1 combined: Cosmology with cosmic shear. *Astronomy & Astrophysics*, 638:L1, June 2020.
- [6] R. Laureijs, J. Amiaux, S. Arduini, J. L. Auguères, J. Brinchmann, R. Cole, M. Cropper, C. Dabin, L. Duvet, A. Ealet, B. Garilli, P. Gondoin, L. Guzzo, J. Hoar, H. Hoekstra, R. Holmes, T. Kitching, T. Maciaszek, Y. Mellier, F. Pasian, W. Percival, J. Rhodes, G. Saavedra Criado, M. Sauvage, R. Scaramella, L. Valenziano, S. Warren, R. Bender, F. Castander, A. Cimatti, O. Le Fèvre, H. Kurki-Suonio, M. Levi, P. Lilje, G. Meylan, R. Nichol, K. Pedersen, V. Popa, R. Rebolo Lopez, H. W. Rix, H. Rottgering, W. Zeilinger, F. Grupp, P. Hudelot, R. Massey, M. Meneghetti, L. Miller, S. Paltani, S. Paulin-Henriksson, S. Pires, C. Saxton, T. Schrabback, G. Seidel, J. Walsh, N. Aghanim, L. Amendola, J. Bartlett, C. Baccigalupi, J. P. Beaulieu, K. Benabed, J. G. Cuby, D. Elbaz, P. Fosalba, G. Gavazzi, A. Helmi, I. Hook, M. Irwin, J. P. Kneib, M. Kunz, F. Mannucci, L. Moscardini, C. Tao, R. Teyssier, J. Weller, G. Zamorani, M. R. Zapatero Osorio, O. Boulade, J. J. Foumond, A. Di Giorgio, P. Guttridge, A. James, M. Kemp, J. Martignac, A. Spencer, D. Walton, T. Blümchen, C. Bonoli, F. Bortoletto, C. Cerna, L. Corcione, C. Fabron, K. Jahnke, S. Ligori, F. Madrid, L. Martin, G. Morgante, T. Pamplona, E. Prieto, M. Riva, R. Toledo, M. Trifoglio, F. Zerbi, F. Abdalla, M. Douspis, C. Grenet, S. Borgani, R. Bouwens, F. Courbin, J. M. Delouis, P. Dubath, A. Fontana, M. Frailis, A. Grazian, J. Koppenhöfer, O. Mansutti, M. Melchior, M. Mignoli, J. Mohr, C. Neissner, K. Noddle, M. Poncet, M. Scodeggio, S. Serrano, N. Shane, J. L. Starck, C. Surace, A. Taylor, G. Verdoes-Kleijn, C. Vuerli, O. R. Williams, A. Zacchei, B. Altieri, I. Escudero Sanz, R. Kohley, T. Oosterbroek, P. Astier, D. Bacon, S. Bardelli, C. Baugh, F. Bellagamba, C. Benoist, D. Bianchi, A. Biviano, E. Branchini, C. Carbone, V. Cardone, D. Clements, S. Colombi, C. Conselice, G. Cresci, N. Deacon, J. Dunlop, C. Fedeli, F. Fontanot, P. Franzetti, C. Giocoli, J. Garcia-Bellido, J. Gow, A. Heavens, P. Hewett, C. Heymans, A. Holland, Z. Huang, O. Ilbert, B. Joachimi, E. Jennins, E. Kerins, A. Kiessling, D. Kirk, R. Kotak, O. Krause, O. Lahav, F. van Leeuwen, J. Lesgourgues, M. Lombardi, M. Magliocchetti,

K. Maguire, E. Majerotto, R. Maoli, F. Marulli, S. Maurogordato, H. McCracken, R. McLure, A. Melchiorri, A. Merson, M. Moresco, M. Nonino, P. Norberg, J. Peacock, R. Pello, M. Penny, V. Pettorino, C. Di Porto, L. Pozzetti, C. Quercellini, M. Radovich, A. Rassat, N. Roche, S. Ronayette, E. Rossetti, B. Sartoris, P. Schneider, E. Semboloni, S. Serjeant, F. Simpson, C. Skordis, G. Smadja, S. Smartt, P. Spano, S. Spiro, M. Sullivan, A. Tilquin, R. Trotta, L. Verde, Y. Wang, G. Williger, G. Zhao, J. Zoubian, and E. Zucca. Euclid Definition Study Report. *arXiv e-prints*, page arXiv:1110.3193, October 2011.

- [7] M. Tegmark. Doppler Peaks on all that: CMB Anisotropies and What They Can Tell Us. In S. Bonometto, J. R. Primack, and A. Provenzale, editors, *Dark Matter in the Universe*, page 379, January 1996.
- [8] Planck Collaboration, N. Aghanim, Y. Akrami, M. Ashdown, J. Aumont, C. Baccigalupi, M. Ballardini, A. J. Banday, R. B. Barreiro, N. Bartolo, S. Basak, R. Battye, K. Benabed, J. P. Bernard, M. Bersanelli, P. Bielewicz, J. J. Bock, J. R. Bond, J. Borrill, F. R. Bouchet, F. Boulanger, M. Bucher, C. Burigana, R. C. Butler, E. Calabrese, J. F. Cardoso, J. Carron, A. Challinor, H. C. Chiang, J. Chluba, L. P. L. Colombo, C. Combet, D. Contreras, B. P. Crill, F. Cuttaia, P. de Bernardis, G. de Zotti, J. Delabrouille, J. M. Delouis, E. Di Valentino, J. M. Diego, O. Doré, M. Douspis, A. Ducout, X. Dupac, S. Dusini, G. Efstathiou, F. Elsner, T. A. Enßlin, H. K. Eriksen, Y. Fantaye, M. Farhang, J. Fergusson, R. Fernandez-Cobos, F. Finelli, F. Forastieri, M. Frailis, A. A. Fraisse, E. Franceschi, A. Frolov, S. Galeotta, S. Galli, K. Ganga, R. T. Génova-Santos, M. Gerbino, T. Ghosh, J. González-Nuevo, K. M. Górski, S. Gratton, A. Gruppuso, J. E. Gudmundsson, J. Hamann, W. Handley, F. K. Hansen, D. Herranz, S. R. Hildebrandt, E. Hivon, Z. Huang, A. H. Jaffe, W. C. Jones, A. Karakci, E. Keihänen, R. Keskitalo, K. Kiiveri, J. Kim, T. S. Kisner, L. Knox, N. Krachmalnicoff, M. Kunz, H. Kurki-Suonio, G. Lagache, J. M. Lamarre, A. Lasenby, M. Lattanzi, C. R. Lawrence, M. Le Jeune, P. Lemos, J. Lesgourgues, F. Levrier, A. Lewis, M. Liguori, P. B. Lilje, M. Lilley, V. Lindholm, M. López-Cañiego, P. M. Lubin, Y. Z. Ma, J. F. Macías-Pérez, G. Maggio, D. Maino, N. Mandolesi, A. Mangilli, A. Marcos-Caballero, M. Maris, P. G. Martin, M. Martinelli, E. Martínez-González, S. Matarrese, N. Mauri, J. D. McEwen, P. R. Meinhold, A. Melchiorri, A. Mennella, M. Migliaccio, M. Millea, S. Mitra, M. A. Miville-Deschênes, D. Molinari, L. Montier, G. Morgante, A. Moss, P. Natoli, H. U. Nørgaard-Nielsen, L. Pagano, D. Paoletti,

- B. Partridge, G. Patanchon, H. V. Peiris, F. Perrotta, V. Pettorino, F. Piacentini, L. Polastri, G. Polenta, J. L. Puget, J. P. Rachen, M. Reinecke, M. Remazeilles, A. Renzi, G. Rocha, C. Rosset, G. Roudier, J. A. Rubiño-Martín, B. Ruiz-Granados, L. Salvati, M. Sandri, M. Savelainen, D. Scott, E. P. S. Shellard, C. Sirignano, G. Sirri, L. D. Spencer, R. Sunyaev, A. S. Suur-Uski, J. A. Tauber, D. Tavagnacco, M. Tenti, L. Toffolatti, M. Tomasi, T. Trombetti, L. Valenziano, J. Valiviita, B. Van Tent, L. Vibert, P. Vielva, F. Villa, N. Vittorio, B. D. Wandelt, I. K. Wehus, M. White, S. D. M. White, A. Zacchei, and A. Zonca. Planck 2018 results. VI. Cosmological parameters. *Astronomy & Astrophysics*, 641:A6, September 2020.
- [9] George Abbé Lemaître and M. A. H. MacCallum. The Expanding Universe. *General Relativity and Gravitation*, 29(5):641–680, May 1997.
- [10] H. Bondi. Spherically Symmetrical Models in General Relativity. *General Relativity and Gravitation*, 31:1783, November 1999.
- [11] Richard C. Tolman. Effect of Inhomogeneity on Cosmological Models. *General Relativity and Gravitation*, 29(7):935–943, June 1997.
- [12] Juan Garcia-Bellido and Troels Haugbølle. Confronting Lemaitre Tolman Bondi models with observational cosmology. *Journal of Cosmology and Astroparticle Physics*, 2008(4):003, April 2008.
- [13] C. Z. Vargas, F. T. Falciano, and R. R. R. Reis. Discrepancy in parameter constraints for LTB models using BAO and SNIa. *Classical and Quantum Gravity*, 34(2):025002, January 2017.
- [14] Andrey V. Kravtsov and Stefano Borgani. Formation of Galaxy Clusters. *Annual Review of Astronomy and Astrophysics*, 50:353–409, September 2012.
- [15] Steven W. Allen, August E. Evrard, and Adam B. Mantz. Cosmological Parameters from Observations of Galaxy Clusters. *Annual Review of Astronomy and Astrophysics*, 49(1):409–470, September 2011.
- [16] Antonio C. da Silva, Scott T. Kay, Andrew R. Liddle, Peter A. Thomas, Frazer R. Pearce, and Domingos Barbosa. The Impact of Cooling and Preheating on the Sunyaev-Zeldovich Effect. *Astrophysical Journal Letters*, 561(1):L15–L18, November 2001.

- [17] Pedro Avelino, Tiago Barreiro, C. Sofia Carvalho, Antonio da Silva, Francisco S. N. Lobo, Prado Martin-Moruno, Jose Pedro Mimoso, Nelson J. Nunes, Diego Rubiera-Garcia, Diego Saez-Gomez, Lara Sousa, Ismael Tereno, and Arlindo Trindade. Unveiling the Dynamics of the Universe. *arXiv e-prints*, page arXiv:1607.02979, July 2016.
- [18] António J.C. da Silva. Elements of Cosmology and Structure Formation. 622(2):7–19, April 2013.
- [19] T. Padmanabhan. *Structure Formation in the Universe*. Cambridge, UK: Cambridge University Press, ISBN-10: 0521424860, 1993.
- [20] A. Jenkins, C. S. Frenk, S. D. M. White, J. M. Colberg, S. Cole, A. E. Evrard, H. M. P. Couchman, and N. Yoshida. The mass function of dark matter haloes. *Monthly Notices of the Royal Astronomical Society*, 321(2):372–384, February 2001.
- [21] Ravi K. Sheth and Giuseppe Tormen. Large-scale bias and the peak background split. *Monthly Notices of the Royal Astronomical Society*, 308(1):119–126, September 1999.
- [22] A. E. Evrard, T. J. MacFarland, H. M. P. Couchman, J. M. Colberg, N. Yoshida, S. D. M. White, A. Jenkins, C. S. Frenk, F. R. Pearce, J. A. Peacock, and P. A. Thomas. Galaxy Clusters in Hubble Volume Simulations: Cosmological Constraints from Sky Survey Populations. *Astrophysical Journal*, 573(1):7–36, July 2002.
- [23] Jeremy Tinker, Andrey V. Kravtsov, Anatoly Klypin, Kevork Abazajian, Michael Warren, Gustavo Yepes, Stefan Gottlöber, and Daniel E. Holz. Toward a Halo Mass Function for Precision Cosmology: The Limits of Universality. *Astrophysical Journal*, 688(2):709–728, December 2008.
- [24] Pedro T. P. Viana and Andrew R. Liddle. The cluster abundance in flat and open cosmologies. *Monthly Notices of the Royal Astronomical Society*, 281:323, July 1996.
- [25] N. J. Nunes, A. C. da Silva, and N. Aghanim. Number counts in homogeneous and inhomogeneous dark energy models. *Astronomy & Astrophysics*, 450(3):899–907, May 2006.
- [26] Naoshi Sugiyama. Cosmic Background Anisotropies in Cold Dark Matter Cosmology. *Astrophysical Journal Supplement*, 100:281, October 1995.

- [27] Sean M. Carroll, William H. Press, and Edwin L. Turner. The cosmological constant. *Annual Review of Astronomy and Astrophysics*, 30:499–542, January 1992.
- [28] N. Aghanim, A. C. da Silva, and N. J. Nunes. Cluster scaling relations from cosmological hydrodynamic simulations in a dark-energy dominated universe. *Astronomy & Astrophysics*, 496(3):637–644, March 2009.
- [29] John E. Carlstrom, Gilbert P. Holder, and Erik D. Reese. Cosmology with the Sunyaev-Zel’dovich Effect. *Annual Review of Astronomy and Astrophysics*, 40:643–680, January 2002.
- [30] Antonio C. da Silva, Domingos Barbosa, Andrew R. Liddle, and Peter A. Thomas. Hydrodynamical simulations of the Sunyaev-Zel’dovich effect: the kinetic effect. *Monthly Notices of the Royal Astronomical Society*, 326(1):155–163, September 2001.
- [31] M. Birkinshaw. The Sunyaev-Zel’dovich effect. *Physics Reports*, 310(2-3):97–195, March 1999.
- [32] J. Delabrouille, M. Betoule, J. B. Melin, M. A. Miville-Deschênes, J. Gonzalez-Nuevo, M. Le Jeune, G. Castex, G. de Zotti, S. Basak, M. Ashdown, J. Aumont, C. Baccigalupi, A. J. Banday, J. P. Bernard, F. R. Bouchet, D. L. Clements, A. da Silva, C. Dickinson, F. Dodu, K. Dolag, F. Elsner, L. Fauvet, G. Faÿ, G. Giardino, S. Leach, J. Lesgourgues, M. Liguori, J. F. Macías-Pérez, M. Massardi, S. Matarrese, P. Mazzotta, L. Montier, S. Mottet, R. Paladini, B. Partridge, R. Piffaretti, G. Prezeau, S. Prunet, S. Ricciardi, M. Roman, B. Schaefer, and L. Toffolatti. The pre-launch Planck Sky Model: a model of sky emission at submillimetre to centimetre wavelengths. *Astronomy & Astrophysics*, 553:A96, May 2013.
- [33] B. Ryden. Introduction to Cosmology. *Cambridge University Press*, 2017.
- [34] Nabila Aghanim, Subhabrata Majumdar, and Joseph Silk. Secondary anisotropies of the CMB. *Reports on Progress in Physics*, 71(6):066902, June 2008.
- [35] Planck Collaboration, P. A. R. Ade, N. Aghanim, C. Armitage-Caplan, M. Arnaud, M. Ashdown, F. Atrio-Barandela, J. Aumont, C. Baccigalupi, A. J. Banday, R. B. Barreiro, J. G. Bartlett, E. Battaner, K. Benabed, A. Benoît, A. Benoit-Lévy, J. P. Bernard, M. Bersanelli, P. Bielewicz, J. Bobin, J. J. Bock, A. Bonaldi, J. R. Bond, J. Borrill, F. R. Bouchet, M. Bridges, M. Bucher, C. Burigana, R. C. Butler, J. F.

Cardoso, P. Carvalho, A. Catalano, A. Challinor, A. Chamballu, H. C. Chiang, L. Y. Chiang, P. R. Christensen, S. Church, D. L. Clements, S. Colombi, L. P. L. Colombo, B. Comis, F. Couchot, A. Coulais, B. P. Crill, A. Curto, F. Cuttaia, A. Da Silva, L. Danese, R. D. Davies, R. J. Davis, P. de Bernardis, A. de Rosa, G. de Zotti, J. Delabrouille, J. M. Delouis, F. X. Désert, C. Dickinson, J. M. Diego, K. Dolag, H. Dole, S. Donzelli, O. Doré, M. Douspis, X. Dupac, G. Efstathiou, T. A. Enßlin, H. K. Eriksen, F. Finelli, I. Flores-Cacho, O. Forni, M. Frailis, E. Franceschi, S. Galeotta, K. Ganga, R. T. Génova-Santos, M. Giard, G. Giardino, Y. Giraud-Héraud, J. González-Nuevo, K. M. Górski, S. Gratton, A. Gregorio, A. Gruppuso, F. K. Hansen, D. Hanson, D. Harrison, S. Henrot-Versillé, C. Hernández-Monteagudo, D. Herranz, S. R. Hildebrandt, E. Hivon, M. Hobson, W. A. Holmes, A. Hornstrup, W. Hovest, K. M. Huffenberger, G. Hurier, A. H. Jaffe, T. R. Jaffe, W. C. Jones, M. Juvela, E. Keihänen, R. Keskitalo, T. S. Kisner, R. Kneissl, J. Knoche, L. Knox, M. Kunz, H. Kurki-Suonio, F. Lacasa, G. Lagache, A. Lähteenmäki, J. M. Lamarre, A. Lasenby, R. J. Laureijs, C. R. Lawrence, J. P. Leahy, R. Leonardi, J. León-Tavares, J. Lesgourgues, M. Liguori, P. B. Lilje, M. Linden-Vørnle, M. López-Caniego, P. M. Lubin, J. F. Macías-Pérez, B. Maffei, D. Maino, N. Mandolesi, A. Marcos-Caballero, M. Maris, D. J. Marshall, P. G. Martin, E. Martínez-González, S. Masi, M. Massardi, S. Matarrese, F. Matthai, P. Mazzotta, A. Melchiorri, J. B. Melin, L. Mendes, A. Mennella, M. Migliaccio, S. Mitra, M. A. Miville-Deschênes, A. Moneti, L. Montier, G. Morgante, D. Mortlock, A. Moss, D. Munshi, P. Naselsky, F. Nati, P. Natoli, C. B. Netterfield, H. U. Nørgaard-Nielsen, F. Noviello, D. Novikov, I. Novikov, S. Osborne, C. A. Oxborrow, F. Paci, L. Pagano, F. Pajot, D. Paoletti, B. Partridge, F. Pasian, G. Patanchon, O. Perdereau, L. Perotto, F. Perrotta, F. Piacentini, M. Piat, E. Pierpaoli, D. Pietrobon, S. Plaszczynski, E. Pointecouteau, G. Polenta, N. Ponthieu, L. Popa, T. Poutanen, G. W. Pratt, G. Prézeau, S. Prunet, J. L. Puget, J. P. Rachen, R. Rebolo, M. Reinecke, M. Remazeilles, C. Renault, S. Ricciardi, T. Riller, I. Ristorcelli, G. Rocha, C. Rosset, M. Rossetti, G. Roudier, J. A. Rubiño-Martín, B. Rusholme, M. Sandri, D. Santos, G. Savini, D. Scott, M. D. Seiffert, E. P. S. Shellard, L. D. Spencer, J. L. Starck, V. Stolyarov, R. Stompor, R. Sudiwala, R. Sunyaev, F. Sureau, D. Sutton, A. S. Suur-Uski, J. F. Sygnet, J. A. Tauber, D. Tavagnacco, L. Terenzi, L. Toffolatti, M. Tomasi, M. Tristram, M. Tucci, J. Tuovinen, G. Umama, L. Valenziano, J. Valiviita, B. Van Tent, J. Varis, P. Vielva, F. Villa, N. Vittorio, L. A. Wade, B. D. Wandelt, S. D. M. White, D. Yvon, A. Zacchei,

- and A. Zonca. Planck 2013 results. XXI. Power spectrum and high-order statistics of the Planck all-sky Compton parameter map. *Astronomy & Astrophysics*, 571:A21, November 2014.
- [36] Jacques Delabrouille and the PSM development team. Planck Sky Model: User Manual version 1.7.8. http://www.apc.univ-paris7.fr/~delabrou/PSM/Public/PSM_user_manual_v1_7_8.pdf, 2013.
- [37] M. Arnaud, G. W. Pratt, R. Piffaretti, H. Böhringer, J. H. Croston, and E. Pointecouteau. The universal galaxy cluster pressure profile from a representative sample of nearby systems (REXCESS) and the $Y_{SZ} - M_{500}$ relation. *Astronomy & Astrophysics*, 517:A92, July 2010.
- [38] Daisuke Nagai, Andrey V. Kravtsov, and Alexey Vikhlinin. Effects of Galaxy Formation on Thermodynamics of the Intracluster Medium. *Astrophysical Journal*, 668(1):1–14, October 2007.
- [39] Chris Clarkson. Establishing homogeneity of the universe in the shadow of dark energy. *Comptes Rendus Physique*, 13(6-7):682–718, July 2012.
- [40] David Alonso, Juan García-Bellido, Troels Haugbølle, and Alexander Knebe. Halo abundances and shear in void models. *Physics of the Dark Universe*, 1(1-2):24–31, November 2012.
- [41] C.E. Pearson. *Handbook of applied mathematics*. Van Nostrand Reinhold Co, Reinhold Company, New York, ISBN-13:978-0442264932, 1974.
- [42] J. Delabrouille, M. Betoule, J. B. Melin, M. A. Miville-Deschênes, J. Gonzalez-Nuevo, M. Le Jeune, G. Castex, G. de Zotti, S. Basak, M. Ashdown, J. Aumont, C. Baccigalupi, A. J. Banday, J. P. Bernard, F. R. Bouchet, D. L. Clements, A. da Silva, C. Dickinson, F. Dodu, K. Dolag, F. Elsner, L. Fauvet, G. Faÿ, G. Giardino, S. Leach, J. Lesgourgues, M. Liguori, J. F. Macías-Pérez, M. Massardi, S. Matarrese, P. Mazzotta, L. Montier, S. Mottet, R. Paladini, B. Partridge, R. Piffaretti, G. Prezeau, S. Prunet, S. Ricciardi, M. Roman, B. Schaefer, and L. Toffolatti. The pre-launch Planck Sky Model: a model of sky emission at submillimetre to centimetre wavelengths. *Astronomy & Astrophysics*, 553:A96, May 2013.

- [43] Elena Pierpaoli, Stefano Borgani, Douglas Scott, and Martin White. On determining the cluster abundance normalization. *Monthly Notices of the Royal Astronomical Society*, 342(1):163–175, June 2003.
- [44] Eric Hivon, Frode K. Hansen, Benjamin D. Wandelt, Krzysztof M. Górski, Anthony J. Banday, and Martin Reinecke. HEALPix Fortran Facility User Guidelines. <https://healpix.jpl.nasa.gov/pdf/facilities.pdf>, 2010.
- [45] Juan García-Bellido and Troels Haugbølle. Looking the void in the eyes—the kinematic Sunyaev Zeldovich effect in Lemaître Tolman Bondi models. *Journal of Cosmology and Astroparticle Physics*, 2008(9):016, September 2008.
- [46] I. Chiu, J. J. Mohr, M. McDonald, S. Bocquet, S. Desai, M. Klein, H. Israel, M. L. N. Ashby, A. Stanford, B. A. Benson, M. Brodwin, T. M. C. Abbott, F. B. Abdalla, S. Allam, J. Annis, M. Bayliss, A. Benoit-Lévy, E. Bertin, L. Bleem, D. Brooks, E. Buckley-Geer, E. Bulbul, R. Capasso, J. E. Carlstrom, A. Carnero Rosell, J. Carretero, F. J. Castander, C. E. Cunha, C. B. D’Andrea, L. N. da Costa, C. Davis, H. T. Diehl, J. P. Dietrich, P. Doel, A. Drlica-Wagner, T. F. Eifler, A. E. Evrard, B. Flaugher, J. García-Bellido, G. Garmire, E. Gaztanaga, D. W. Gerdes, A. Gonzalez, D. Gruen, R. A. Gruendl, J. Gschwend, N. Gupta, G. Gutierrez, J. Hlavacek-L, K. Honscheid, D. J. James, T. Jeltema, R. Kraft, E. Krause, K. Kuehn, S. Kuhlmann, N. Kuropatkin, O. Lahav, M. Lima, M. A. G. Maia, J. L. Marshall, P. Melchior, F. Menanteau, R. Miquel, S. Murray, B. Nord, R. L. C. Ogando, A. A. Plazas, D. Rapetti, C. L. Reichardt, A. K. Romer, A. Roodman, E. Sanchez, A. Saro, V. Scarpine, R. Schindler, M. Schubnell, K. Sharon, R. C. Smith, M. Smith, M. Soares-Santos, F. Sobreira, B. Stalder, C. Stern, V. Strazzullo, E. Suchyta, M. E. C. Swanson, G. Tarle, V. Vikram, A. R. Walker, J. Weller, and Y. Zhang. Baryon content in a sample of 91 galaxy clusters selected by the South Pole Telescope at $0.2 < z < 1.25$. *Monthly Notices of the Royal Astronomical Society*, 478(3):3072–3099, August 2018.
- [47] Anthony H. Gonzalez, Suresh Sivanandam, Ann I. Zabludoff, and Dennis Zaritsky. Galaxy Cluster Baryon Fractions Revisited. *Astrophysical Journal*, 778(1):14, November 2013.
- [48] M. S. Mirakhor and S. A. Walker. A complete view of the outskirts of the Coma cluster. *Monthly Notices of the Royal Astronomical Society*, 497(3):3204–3220, September 2020.

- [49] Philip Bull, Timothy Clifton, and Pedro G. Ferreira. Kinematic Sunyaev-Zel'dovich effect as a test of general radial inhomogeneity in Lemaitre-Tolman-Bondi cosmology. *Physical Review D*, 85(2):024002, January 2012.
- [50] B.W. Silverman. Density Estimation for Statistics and Data Analysis. *Monographs on Statistics and Applied Probability*, Chapman and Hall, 1986.
- [51] Antonio C. da Silva, Domingos Barbosa, Andrew R. Liddle, and Peter A. Thomas. Hydrodynamical simulations of the Sunyaev-Zel'dovich effect. *Monthly Notices of the Royal Astronomical Society*, 317(1):37–44, September 2000.

Appendices

Zero Order Modification

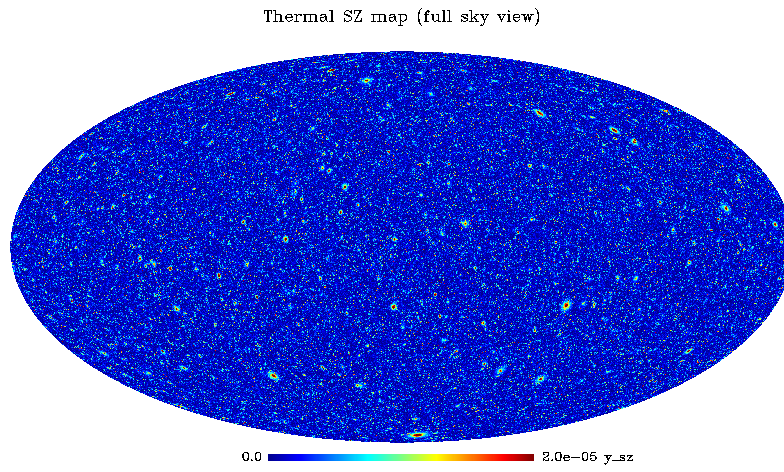


Figure .1: Mollview projection of the thermal SZ map for a CGBH model with $\Omega_{in}=0.2$.

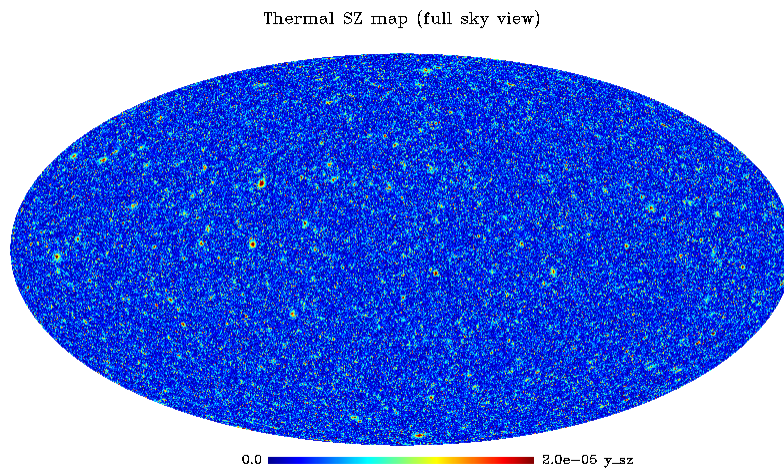


Figure .2: Mollview projection of the thermal SZ map for a CGBH model with $\Omega_{in}=0.4$

Thermal SZ map (full sky view)

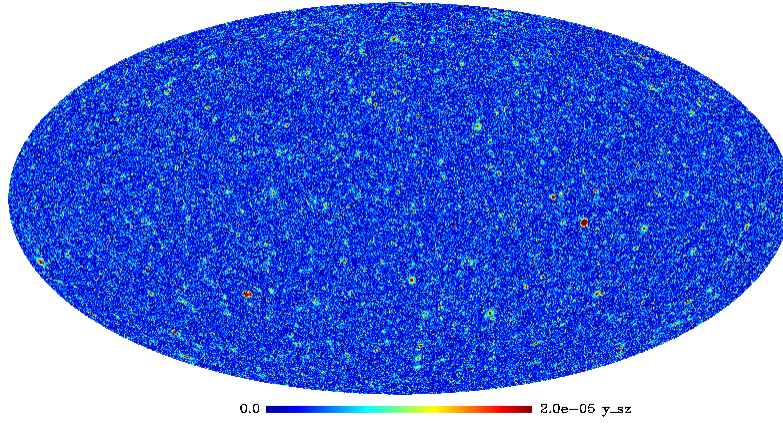


Figure .3: Mollview projection of the thermal SZ map for a CGBH model with $r_0=0.750$ Gpc.

Thermal SZ map (full sky view)

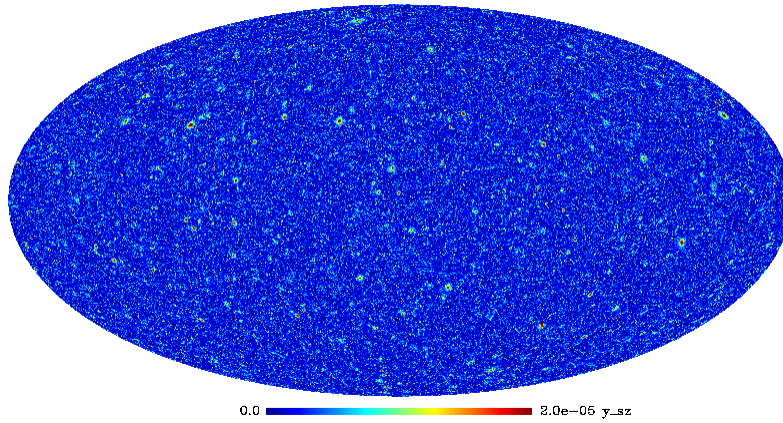


Figure .4: Mollview projection of the thermal SZ map for a CGBH model with $r_0=1.0$ Gpc.

Thermal SZ map (full sky view)

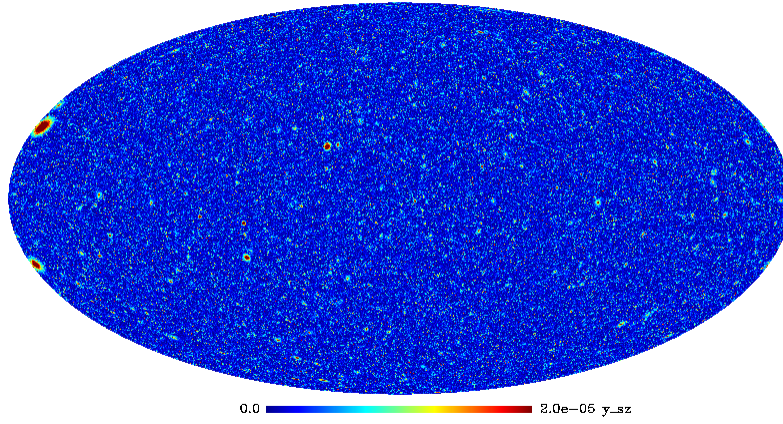


Figure .5: Mollview projection of the thermal SZ map for a CGBH model with $r_0=2.0$ Gpc.

Thermal SZ map (full sky view)

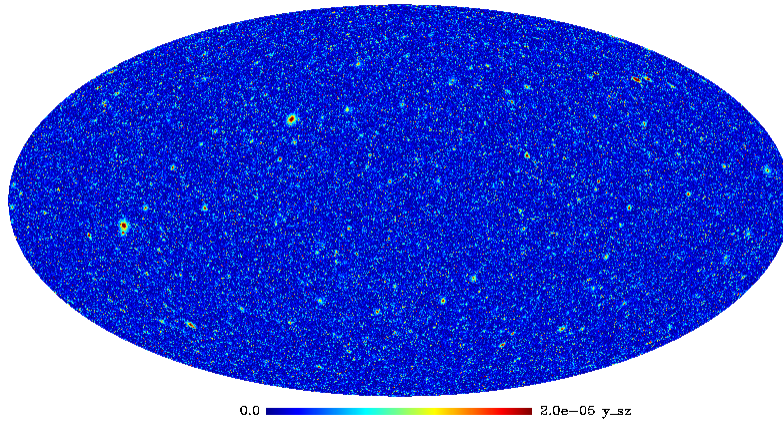


Figure .6: Mollview projection of the thermal SZ map for a CGBH model with $r_0=2.5$ Gpc.

Thermal SZ map (full sky view)

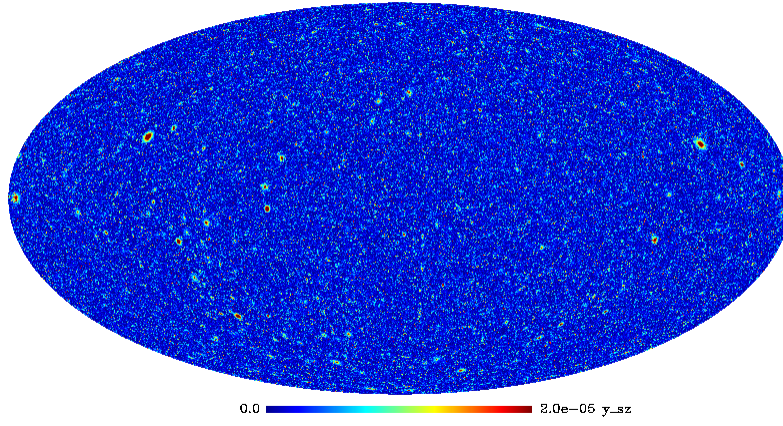


Figure .7: Mollview projection of the thermal SZ map for a CGBH model with $\Delta r = 0.250$ Gpc.

Thermal SZ map (full sky view)

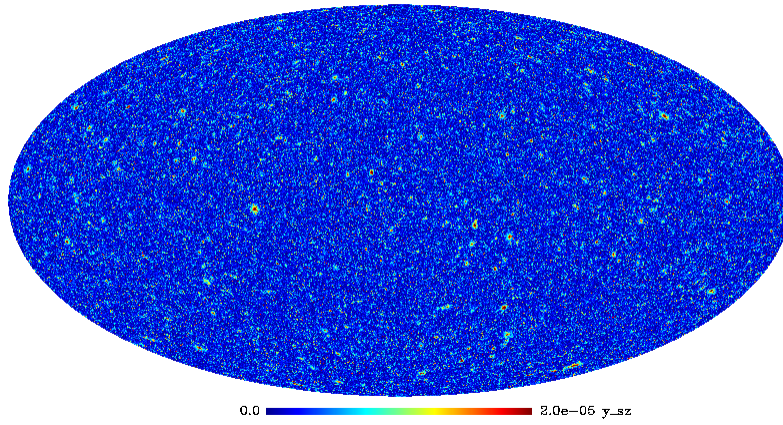


Figure .8: Mollview projection of the thermal SZ map for a CGBH model with $\Delta r = 0.750$ Gpc.

Thermal SZ map (full sky view)

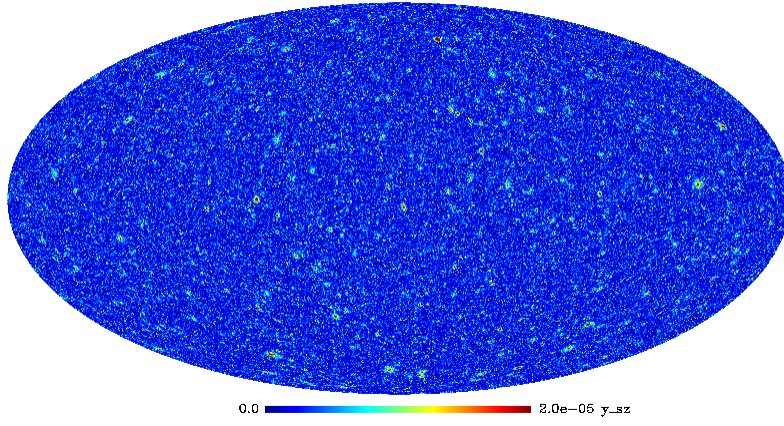


Figure .9: Mollview projection of the thermal SZ map for a CGBH model with $h=0.625$ km/s/Mpc.

Thermal SZ map (full sky view)

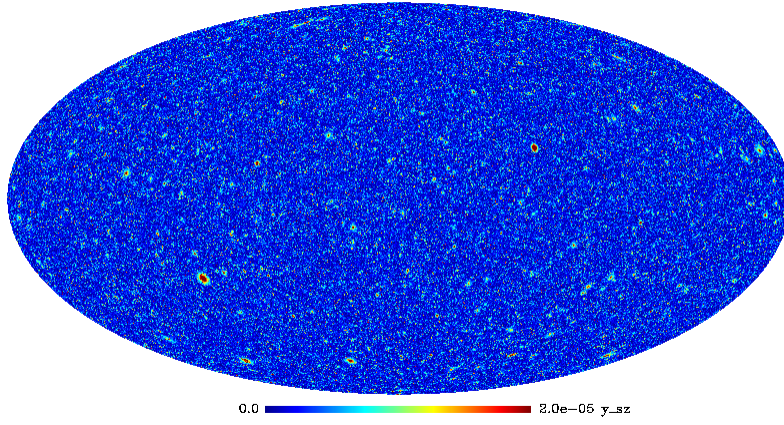


Figure .10: Mollview projection of the thermal SZ map for a CGBH model with $h=0.65$ km/s/Mpc.

Thermal SZ map (full sky view)

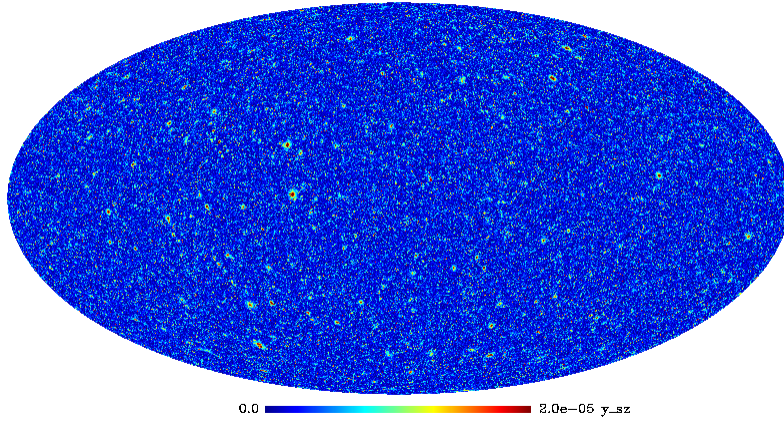


Figure .11: Mollview projection of the thermal SZ map for a CGBH model with $h=0.675$ km/s/Mpc.

Thermal SZ map (full sky view)

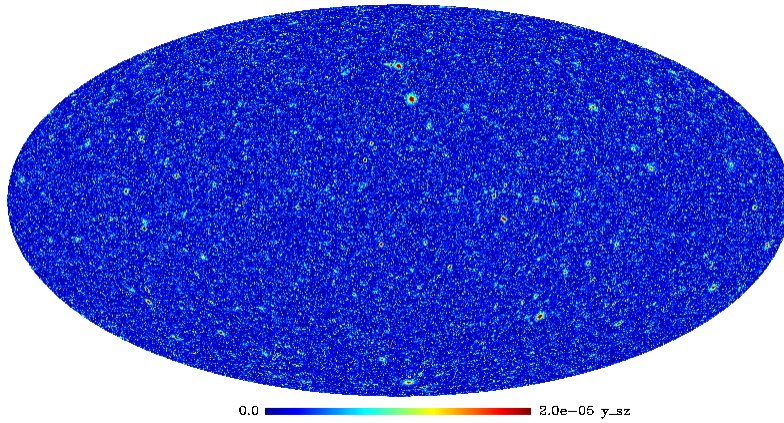


Figure .12: Mollview projection of the thermal SZ map for a CGBH model with $h=0.75$ km/s/Mpc.

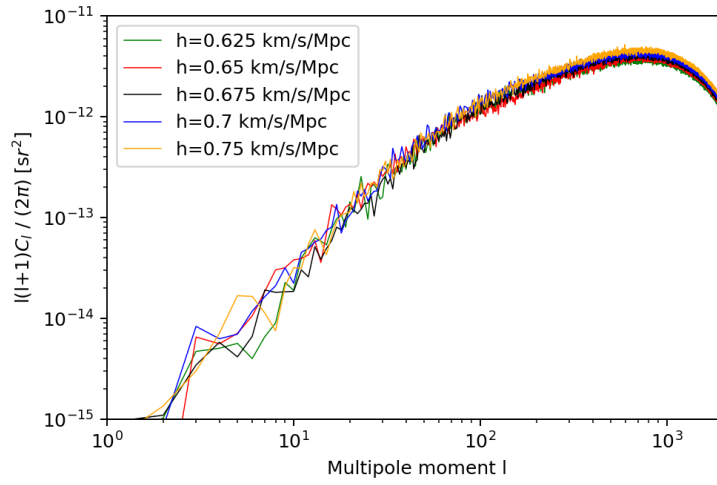


Figure .13: Power Spectra of the CGBH model when varying h .

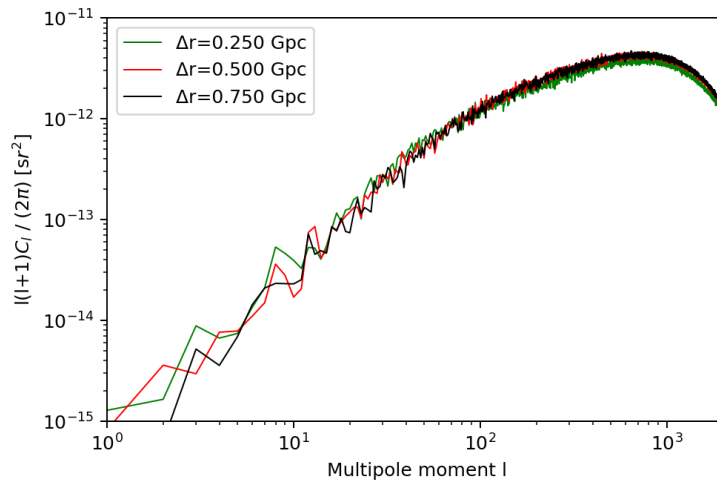


Figure .14: Power Spectra of the CGBH model when varying Δr .

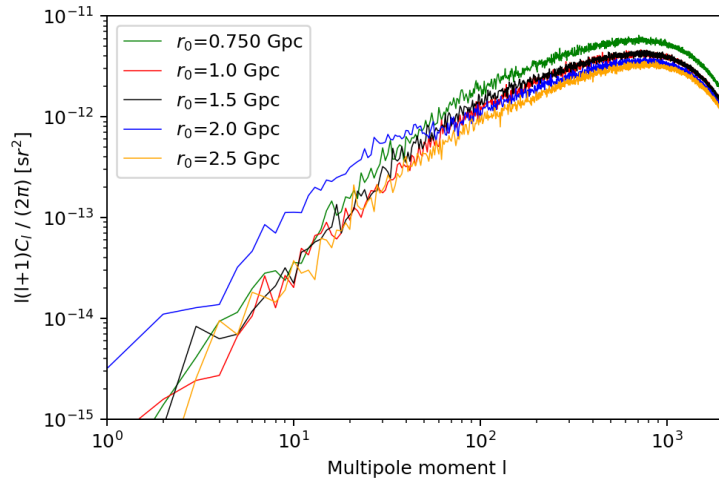


Figure .15: *Power Spectra of the CGBH model when varying r_0 .*

First Order Modification

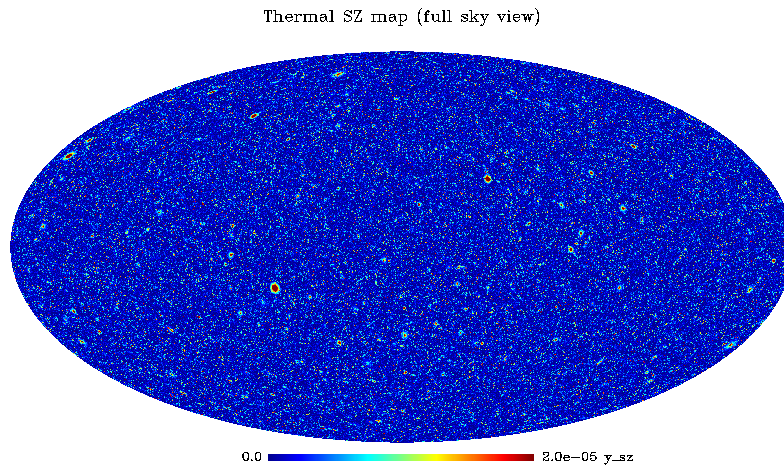


Figure .16: Mollview projection of the thermal SZ map for a CGBH model with $\Omega_{in}=0.1$

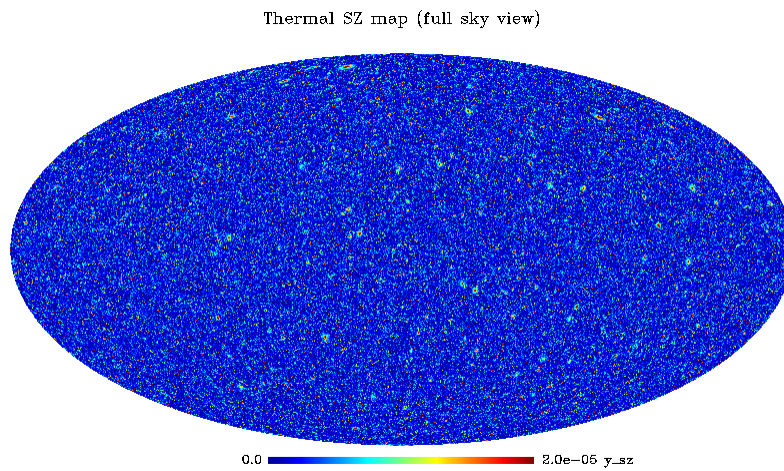


Figure .17: Mollview projection of the thermal SZ map for a CGBH model with $\Omega_{in}=0.2$

Thermal SZ map (full sky view)

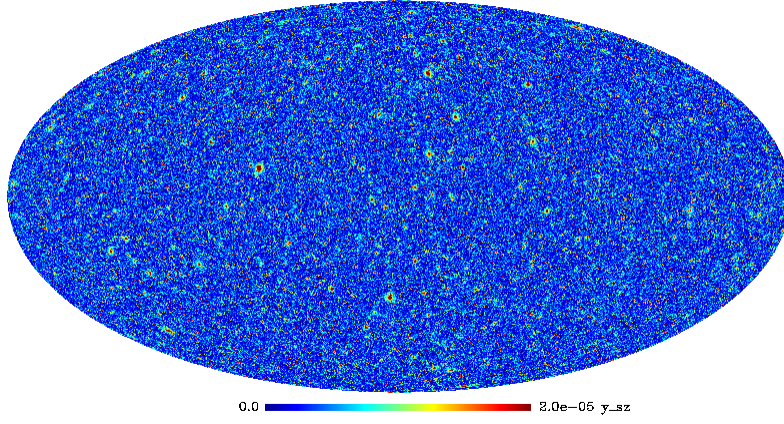


Figure .18: *Mollview projection of the thermal SZ map for a CGBH model with $r_0=1.0$ Gpc.*

Thermal SZ map (full sky view)

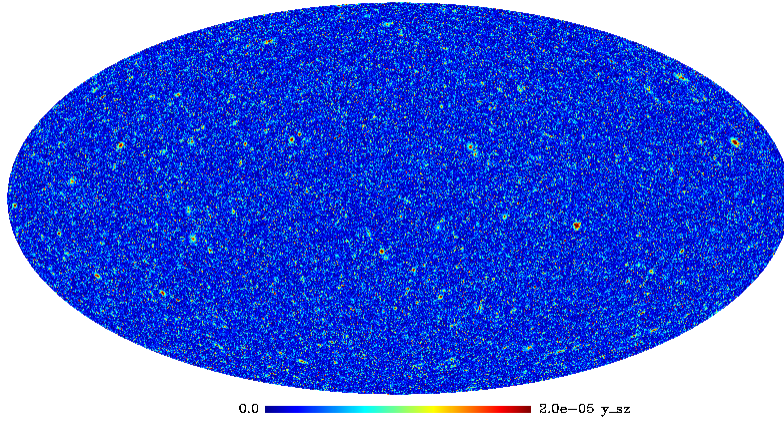


Figure .19: *Mollview projection of the thermal SZ map for a CGBH model with $r_0=2.0$ Gpc.*

on line processing :

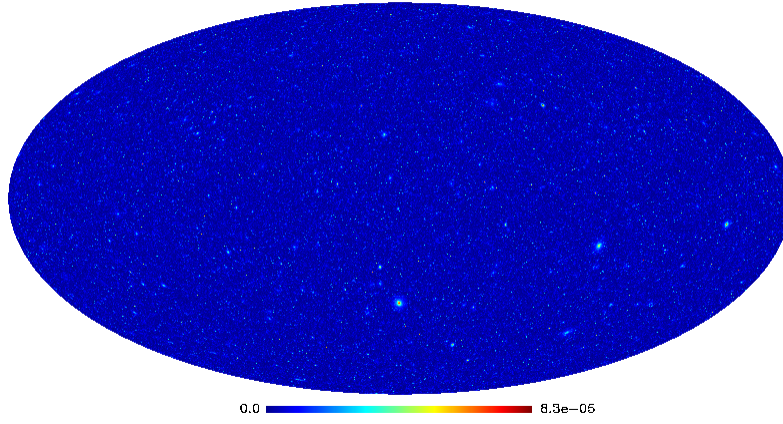


Figure .20: Mollview projection of the thermal SZ map for a CGBH model with $h=0.65$ km/s/Mpc.

Thermal SZ map (full sky view)

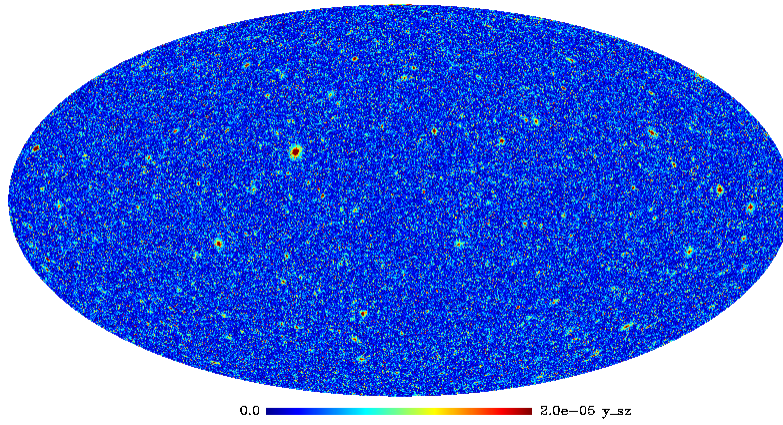


Figure .21: Mollview projection of the thermal SZ map for a CGBH model with $h=0.675$ km/s/Mpc.